

SIDE-IMPLANTED PIEZORESISTIVE SHEAR STRESS SENSOR FOR TURBULENT
BOUNDARY LAYER MEASUREMENT

By

YAWEI LI

A DISSERTATION PRESENTED TO THE GRADUATE SCHOOL
OF THE UNIVERSITY OF FLORIDA IN PARTIAL FULFILLMENT
OF THE REQUIREMENTS FOR THE DEGREE OF
DOCTOR OF PHILOSOPHY

UNIVERSITY OF FLORIDA

2008

© 2008 Yawei Li

To my husband Zhongmin and my parents

ACKNOWLEDGMENTS

Financial support for the research project is provided by National Science Foundation (CTS-04352835 and CMS-0428593) and AFOSR grant (F49620-03-C-0114). A doctoral dissertation is never the work of an individual, but instead a miracle that encompasses the efforts of many people. I would like to recognize a number of people who have helped me in various ways during my time in University of Florida.

First and foremost, I extend my sincerest gratitude to my advisor, Dr. Mark Sheplak, who gave me the opportunity to work in MEMS research field. I sincerely appreciate his guidance, continuous encouragement and support in my research, tirelessly sharing with me his expertise and wisdom. His profound knowledge in MEMS, fluids, acoustics and so on is the invaluable source I always rely on.

I also wish to extend gracious thanks to my committee members, Drs. Toshikazu Nishida, Louis N. Cattafesta, Bhavani V. Sankar and David Arnold for their instruction and assistance on this interdisciplinary project. They are always generous on their time and expertise, and I am grateful for their efforts.

I would give special thanks to professors in Department of Electrical and Computer Engineering, Material Science Engineering and Mechanical and Aerospace Engineering at University of Florida, especially Dr. Mark Law and his student Ljubo Radic, Dr. Kevin Jones and Dr. Raphael Haftka for their invaluable suggestions on my device fabrication, process simulation and design optimization. I would especially like to thank Dr. Melih Pepila at Sabanchi University (Turkey) and Dr. Jaco F. Schutte for their suggestions in optimization design.

My thanks go to Dr. Venketaraman Chandrasekaran at Sensata Technologies, Sean Knight in University of South Florida, Alvin A Barlian in Stanford University and Core Systems

Company for their help in device fabrications, and Keck Pathammavong at Engent for his help in device packaging. I would also express my thanks to Al Ogden, Dr. Ivan Kravchenko and Bill Lewis at UFNF for the facility maintenance and help on the fabrication.

I was fortunate enough to have great colleagues throughout my graduate school experience. My thanks go to IMG members, especially Hongwei Qu for his suggestions and discussions in device fabrication; Brandon Bertolucci, Alex Phipps, David Martin for their kind help and assistance in device package design, Vijay Chandrasekharan, Qi Song, Benjamin Griffin and John Griffin for their kind help in device characterization, Matt Williams, Benjamin Griffin, Brandon Bertolucci and Brian Homeijier for their great editing and suggestions in my dissertation writing. It has been a pleasure to have work with them, and I will carry these invaluable memories on rest of life.

Finally, I reserve the special thanks to my families for their support and encouragement. I am always grateful to my husband, Zhongmin Liu for his endless love and support in my life. My parents always encouraged me to be the best and do my best on what I want to do. I would like to thank them for believing me every time I said I would graduate “next year”. Without their love and support this dissertation would not be possible.

TABLE OF CONTENTS

	<u>page</u>
ACKNOWLEDGMENTS	4
LIST OF TABLES	9
LIST OF FIGURES	10
ABSTRACT	14
CHAPTER	
1 INTRODUCTION	16
Motivation for Wall Shear Stress Measurement.....	16
Wall Shear Stress.....	17
Turbulent Boundary Layer	19
Research Objectives.....	22
Dissertation Overview	24
2 BACKGROUND	29
Techniques for Shear Stress Measurement.....	29
Conventional Techniques	30
MEMS-Based Techniques.....	31
Floating Element Sensors	32
Sensor Modeling and Scaling.....	32
Error Analysis and Challenges	34
Effect of misalignment	34
Effect of pressure gradient	35
Effect of cross-axis vibration and pressure fluctuations	36
Previous MEMS Floating Element Shear Stress Sensors.....	38
Capacitive Shear Stress Sensors.....	38
Optical Shear Stress Sensors	40
Piezoresistive Shear Stress Sensors.....	42
A Fully-Bridge Side-Implanted Piezoresistive Shear Stress Sensor	43
3 SHEAR STRESS SENSOR MODELING	53
Quasi-Static Modeling.....	54
Structural Modeling.....	54
Small Deflection Theory	55
Large Deflection Theory	56
Energy method	57
Exact analytical model	57
Lumped Element Modeling.....	58

Finite Element Analysis.....	60
Piezoresistive Transduction.....	62
Piezoresistive Coefficients.....	64
Piezoresistive Sensitivity.....	66
Electromechanical Sensitivity.....	68
Noise Model.....	69
Thermal Noise.....	69
$1/f$ Noise.....	70
Device Specific Issues.....	72
Transverse Sensitivity.....	72
Temperature Compensation.....	73
Device Junction Isolation.....	74
Summary.....	78
4 DEVICE OPTIMIZATION.....	91
Problem Formulation.....	91
Design Variables.....	91
Objective Function.....	93
Constraints.....	94
Candidate Flows.....	95
Methodology.....	96
Optimization Results and Discussion.....	97
Sensitivity Analysis.....	98
Summary.....	100
5 FABRICATION AND PACKAGING.....	105
Fabrication Overview and Challenges.....	105
Fabrication Process.....	105
Sensor Packaging for Wind Tunnel Testing.....	110
6 EXPERIMENTAL CHARACTERIZATION.....	118
Experimental Characterization Issues.....	118
Experimental Setup.....	119
Electrical Characterization.....	119
Dynamic Calibration.....	120
Noise Measurement.....	121
Experimental Results.....	122
Electrical Characterization.....	122
Dynamic Calibration Results and Discussion.....	122
Summary.....	126

7	CONCLUSION AND FUTURE WORK	137
	Summary and Conclusions	137
	Future Work.....	138
	Temperature Compensation.....	139
	Static Characterization.....	141
	Noise Measurement	142
	Recommendations for Future Sensor Designs.....	142
 APPENDIX		
A	MECHANICAL ANALYSIS.....	145
	Small Deflection	145
	Large Deflection-Energy Method.....	147
	Large Deflection-Analytical Method.....	149
	Stress Analysis.....	152
	Effective Mechanical Mass and Compliance	153
B	NOISE FLOOR OF THE WHEATSTONE BRIDGE	157
C	PROCESS TRAVELER	160
	Masks.....	160
	Process Steps	160
D	PROCESS SIMULATION	166
E	MICROFABRICATION RECIPE FOR RIE AND DRIE PROCESS.....	169
F	PACKAGING DRAWINGS	170
	LIST OF REFERENCES.....	173
	BIOGRAPHICAL SKETCH	180

LIST OF TABLES

<u>Table</u>	<u>page</u>
1-1	Summary of typical skin friction contributions for various vehicles.....25
1-2	Parameters in the turbulent boundary layer.25
3-1	Material properties and geometry parameters used for model validation.....79
3-2	Resonant frequency and effective mass predicted by LEM and FEA.79
3-3	First 6 modes and effective mass predicted by FEA for the representative structure.....79
3-4	Piezoresistive coefficients for n-type and p-type silicon.79
3-5	Piezoresistive coefficients for n-type and p-type silicon in the <110> direction.80
3-6	Space parameter dimensions for junction isolation.80
4-1	The candidate shear stress sensor specifications.102
4-2	Upper and lower bounds associated with the specifications in Table 4-1.102
4-3	Optimization results for the cases specified in Table 4-1.103
6-1	LabVIEW settings for noise PSD measurement.....128
6-2	The optimal geometry of the shear stress sensor that was characterized.....128
6-3	Sensitivity at different bias voltage for the tested sensor.128
6-4	A comparison of the predicted versus realized performance of the sensor under test for a bias voltage of 1.5V.....129
E-1	Input parameters in the ASE on STS DRIE systems.169
E-2	Anisotropic oxide/nitride etch recipe on the Unaxis ICP Etcher system.....169
E-3	Anisotropic aluminum etch recipe on the Unaxis ICP Etcher system.169

LIST OF FIGURES

<u>Figure</u>	<u>page</u>
1-1 Schematic of wall shear stress in a laminar boundary layer on an airfoil section.	26
1-2 Schematic representation of the boundary layer transition process for a flat-plate flow at a ZPG	26
1-3. Schematic of typical velocity profile for low-speed laminar and turbulent boundary layers [9].	27
1-4 The structure of a typical turbulent boundary layer.....	27
1-5 Estimates of Kolmogorov microscales of length and time as a function of Reynolds number based on a $1/7^{\text{th}}$ power-law profile.	28
2-1 Schematic cross-sectional view of the floating element based sensor.....	46
2-2 Schematic plan view and cross-section of a typical floating element sensor	46
2-3 Integrated shear force variation as a function of sensor resolution for different element areas.....	47
2-4 Schematic illustrating pressure gradient effects on the force balance of a floating element.....	47
2-5 Schematic cross-sectional view of the capacitive floating element sensor	48
2-6 Plan-view of a horizontal-electrode capacitive floating element sensor	48
2-7 Schematic top-view of a differential capacitive shear stress sensor	49
2-8 A schematic cross-sectional view of an optical differential shutter-based floating element shear stress sensor	49
2-9 Schematic top and cross-sectional view of a Febry-Perot shear stress sensor	50
2-10 Top and cross-sectional view of Moiré optical shear stress sensor	50
2-11 A schematic top view of an axial piezoresistive floating element sensor	51
2-12 A schematic top view of a laterally-implanted piezoresistive shear stress sensor	51
2-13 A schematic 3D view of the side-implanted piezoresistive floating element sensor.....	52
3-1 Schematic top view of the structure of a piezoresistive floating element sensor.	81
3-2 The simplified clamped-clamped beam model of the floating element structure.....	81

3-3	Lumped element model of a floating element sensor: (a) spring-mass-dashpot system (mechanical) and (b) equivalent electrical LCR circuit.....	81
3-4	Representative results of displacement of tethers for the representative structure.....	82
3-5	Representative load-deflection characteristics of analytical models and FEA for the representative structure.	82
3-6	Verification of the analytically predicted stress profile with FEA results for the representative structure.	83
3-7	The mode shape for the representative structure.	83
3-8	Geometry used in computation of Euler's angles.	84
3-9	Polar dependence of piezoresistive coefficients for p-type silicon in the (100) plane.	84
3-10	Polar dependence of piezoresistive coefficients for n-type silicon in the (100) plane.	85
3-11	Piezoresistive factor as a function of impurity concentration for p- type silicon at 300K	85
3-12	Schematic illustrating the relevant geometric parameters for piezoresistor sensitivity calculations.	86
3-13	Schematic representative of a deflected side-implanted piezoresistive shear stress sensor and corresponding resistance changes in Wheatstone bridge.....	86
3-14	Wheatstone bridge subjected to cross-axis acceleration (a) and pressure (b).....	87
3-15	Schematic of the double-bridge temperature compensation configuration.	87
3-16	Top view schematic of the side-implanted piezoresistor and p++ interconnect in an n-well (a) and equivalent electric circuit indicating that the sensor and leads are junction isolated (b).	88
3-17	Doping profile of n-well, p++ interconnect, and piezoresistor using FLOOPS simulation.....	88
3-18	Cross view of isolation width between p++ interconnects.	89
3-19	Cross view of isolation width between p++ interconnect and piezoresistor.....	89
3-20	Top view of the isolation widths on a sensor tether.....	90
3-21	Top view schematic of the side-implanted piezoresistor with a metal line contact.....	90
4-1	Flow chart of design optimization of the piezoresistive shear stress sensor.....	104

4-2	Logarithmic derivative of objective function τ_{\min} with respect to parameters.	104
5-1	Process flow of the side-implanted piezoresistive shear stress sensor.	112
5-2	SEM side view of side wall trench after DRIE Si.	113
5-3	SEM side view of the notch at the interface of oxide and Si after DRIE.	113
5-4	SEM top view of the trench after DRIE oxide and Si.....	114
5-5	SEM top views of the trench after DRIE oxide and Si with oxide overetch.	114
5-6	SEM top views of the trench with silicon grass through a micromasking effect due to oxide underetch.	115
5-7	SEM side view of the trench after DRIE oxide and Si.	115
5-8	Photograph of the fabricated device.	116
5-9	A photograph of the device with a close up view of the side-implanted piezoresistor. ...	116
5-10	Photograph of the PCB embedded in Lucite package.	117
5-11	Interface circuit board for offset compensation.	117
6-1	The bridge dc offset voltage as a function of bias voltages for the tested sensor.....	130
6-2	An electrical schematic of the interface circuit for offset compensation.....	130
6-3	A schematic of the experimental setup for the dynamic calibration experiements.	131
6-4	Forward and reverse bias characteristics of the p/n junction.....	131
6-5	Reverse bias breakdown voltage of the P/N junction.	132
6-7	The nonlinearity of the I-V curve in Figure 6-6 at different sweeping voltages.	133
6-8	The output voltage as a function of shear stress magnitude of the sensor at a forcing frequency of 2.088 kHz as a function bias voltage.....	133
6-9	The normalized output voltage as a function of shear stress magnitude of the sensor at a forcing frequency of 2.088 kHz for several bias voltages.....	134
6-10	Gain and phase factors of the frequency response function.	134
6-11	The magnitude and phase angle of the reflection coefficient of the plane wave tube.	135
6-12	Output–referred noise floor of the measurement system at a bias voltage of 1.5V.....	136

7-1	Pressure drops versus length between taps in the flow cell.....	144
7-2	Experimental setup of static calibration.....	144
A-1	The clamped beam and free body diagram. a) Clamped-clamped beam. b) Free body diagram of the beam. c) Free body diagram of part of the beam.....	156
A-2	Clamped-clamped beam in large deflection.	156
A-3	Clamped-clamped beam in small deflection (a) and free body diagram of the clamped beam (b).....	156
B-1	The Wheatstone bridge.	159
B-2	The thermal noise model of the Wheatstone bridge.	159
B-3	The $1/f$ noise model of the Wheatstone bridge.....	159
E-1	The drawing illustrating the Lucite packaging.	170
E-2	The aluminum plate for the plane wave tube interface connection.	171
E-3	Aluminum packaging for pressure sensitivity testing.....	172

Abstract of Dissertation Presented to the Graduate School
of the University of Florida in Partial Fulfillment of the
Requirements for the Degree of Doctor of Philosophy

SIDE-IMPLANTED PIEZORESISTIVE SHEAR STRESS SENSOR FOR TURBULENT
BOUNDARY LAYER MEASUREMENT

By

Yawei Li

August 2008

Chair: Mark Sheplak
Major: Aerospace Engineering

In this dissertation, I discuss the device modeling, design optimization, fabrication, packaging and characterization of a micromachined floating element piezoresistive shear stress sensor for the time-resolved, direct measurement of fluctuating wall shear stress in a turbulent flow. This device impacts a broad range of applications from fundamental scientific research to industrial flow control and biomedical applications.

The sensor structure integrates side-implanted, diffused resistors into the silicon tethers for piezoresistive detection. Temperature compensation is enabled by integrating a fixed, dummy Wheatstone bridge adjacent to the active shear-stress sensor. A theoretical nonlinear mechanical model is combined with a piezoresistive sensing model to determine the electromechanical sensitivity. Lumped element modeling (LEM) is used to estimate the resonant frequency. Finite element modeling is employed to verify the quasi-static and dynamic models. Two dominant electrical noise sources in the piezoresistive shear stress sensor, $1/f$ noise and thermal noise, and amplifier noise were considered to determine the noise floor. These models were then leveraged to obtain optimal sensor designs for several sets of specifications. The cost function, minimum detectable shear stress (MDS) formulated in terms of sensitivity and noise floor, is

minimized subject to nonlinear constraints of geometry, linearity, bandwidth, power, resistance, and manufacturing limitations. The optimization results indicate a predicted optimal device performance with a MDS of $O(0.1 \text{ mPa})$ and a dynamic range greater than 75 dB. A sensitivity analysis indicates that the device performance is most responsive to variations in tether width.

The sensors are fabricated using an 8-mask, bulk micromachining process on a silicon wafer. An n-well layer is formed to control the space-charge layer thickness of reverse-biased p/n junction-isolated piezoresistors. The sensor geometry is realized using reactive ion etch (RIE) and deep reactive ion etch (DRIE). Hydrogen annealing is employed to smooth the sidewall scalloping caused by DRIE. The piezoresistors are achieved by side-wall boron implantation. The structure is finally released from the backside using the combination of DRIE and RIE.

Electrical characterization indicates linear junction-isolated resistors, and a negligible leakage current ($<0.12 \text{ }\mu\text{A}$) for the junction-isolated diffused piezoresistors up to a reverse bias voltage of -10 V. Using a known acoustically-excited wall shear stress for calibration, the sensor exhibited a sensitivity of $4.24 \text{ }\mu\text{V/Pa}$, a noise floor of $11.4 \text{ mPa}/\sqrt{\text{Hz}}$ at 1 kHz, a linear response up to the maximum testing range of 2 Pa, and a flat dynamic response up to the testing limit of 6.7 kHz. These results, coupled with a wind-tunnel suitable package, result in a suitable transducer for turbulence measurements in low-speed flows, a first for piezoresistive MEMS-based direct shear stress sensors.

CHAPTER 1 INTRODUCTION

This chapter provides an introduction to wall shear stress and motivation for its measurement. Then the scaling turbulent boundary layer is reviewed as it applies to dictating the requirements for wall shear stress sensors. The research objectives and contributions are presented. This chapter ends with the dissertation overview.

Motivation for Wall Shear Stress Measurement

The quantification of wall shear stress is important in a variety of engineering applications, specifically in the development of aerospace and naval vehicles. These vehicles span a wide range of Reynolds numbers (Re) from low Re (unmanned air vehicles for homeland security surveillance and detection) to a very high Re (hypersonic vehicles for rapid global and space access). Across the Re range, unsteady, complex flow phenomena associated with transitional, turbulent, and separating boundary layers play an important role in aerodynamics and propulsion efficiency of these vehicles [1, 2]. Furthermore, since shear stress is a vector field, it may provide advantages over pressure sensing in active flow control applications involving separated flows [3].

The accurate measurement of the wall shear stress is of vital importance for understanding the critical vehicle characteristics, such as lift, drag, and propulsion efficiency. Therefore, the ability to obtain quantitative, time-resolved shear stress measurements may elucidate complex physics and ultimately help engineers improve the performance of these vehicles [4]. Viscous drag or skin friction drag is formed due to shear stress in the boundary layer. The viscous loss is highly dependent on the physical aerodynamic/hydrodynamic system; typical viscous losses for different systems are listed in Table 1-1 [5]. For aircraft, reducing skin friction by 20% results in a 10% annual fuel savings, and for underwater vehicles, a reduction of skin friction drag of 20%

would result in a 6.8% increase in speed [5]. Therefore, shear stress measurement attracts attention in sensor-actuator systems for use in active control of the turbulent boundary layer with an aim of minimizing the skin friction [6].

Wall Shear Stress

When a continuum viscous fluid flows over an object, the no slip boundary condition at the surface results in a velocity gradient within a very thin boundary layer [7]; the streamwise velocity increases from zero at the wall to its free-stream value at the edge of the boundary layer. The velocity profile is shown in Figure 1-1. The viscous effects are confined to the boundary layer, while outside of the boundary layer the flow is essentially inviscid [7]. Two classes of surface forces act on the aerodynamic body: the normal force per unit area (pressure) P , and the tangential force per unit area (shear stress) τ_w . For a Newtonian flow, the wall shear stress is proportional to the velocity gradient at the wall.

The boundary layer is classified as laminar or turbulent depending on Reynolds number or flow structure [7]. A laminar boundary layer forms at low Reynolds numbers and is characterized by its smooth and orderly motion, where microscopic mixing of mass, momentum and energy occurs only between adjacent vertical fluid layers. A turbulent boundary layer forms at high Reynolds numbers and is characterized by random and chaotic motion [8]. The macroscopic mixing traverses several regions within the boundary layer. There is a transition range between laminar and turbulent boundary layers, partially laminar and partially turbulent, as shown in Figure 1-2. In the transition range, the flow is very sensitive to small disturbances [8].

Typical velocity profiles for low speed laminar and turbulent boundary layer are shown in Figure 1-3. Due to the intense mixing, the turbulent boundary layer has a fuller velocity profile; thus, the shear stress in the turbulent boundary layer is larger than in a laminar boundary layer.

The boundary layer thickness, $\delta(x)$, is defined as the distance from the wall to the point at which the velocity is 99% of the free-stream velocity [7]. The laminar boundary layer thickness in a zero pressure gradient flat-plate flow is given by Blasius as [7]

$$\frac{\delta}{x} = \frac{5.0}{\sqrt{Re_x}}, \quad (1-1)$$

where Re_x is the free stream Reynolds number and given by $U_\infty x/\nu$, x is the streamwise distance, U_∞ is the free stream velocity, and ν is the kinematic viscosity of the fluid. For turbulent flow, the boundary layer thickness is estimated by the 1/7th power law velocity profile is [7]

$$\frac{\delta}{x} = \frac{0.16}{(Re_x)^{1/7}}. \quad (1-2)$$

The shear stress is related to skin friction by the skin-friction coefficient

$$C_f = \frac{\tau_w}{\frac{1}{2}\rho U_\infty^2}, \quad (1-3)$$

The wall shear stress τ_w for a one dimensional laminar flow is given by Newton's law of viscosity [7],

$$\tau_w = \mu \left. \frac{du}{dy} \right|_{y=0}, \quad (1-4)$$

where μ is the dynamic viscosity of the fluid and u is the local streamwise velocity in the boundary layer. For turbulent flow, the shear stress is decomposed into mean shear stress $\overline{\tau_w}$ and fluctuating shear stress τ_w' in terms of the Reynolds decomposition,

$$\tau_w = \overline{\tau_w} + \tau_w'. \quad (1-5)$$

The mean skin friction for laminar and turbulent flow are given by [7]

$$C_{f,plate} = \frac{2\tau_w}{\rho U_\infty^2} = \frac{0.664}{\sqrt{Re_x}}, \quad (1-6)$$

and

$$C_{f,plate} = \frac{0.027}{(Re_x)^{1/7}}, \quad (1-7)$$

respectively. Equation (1-2) and (1-7) are based on the assumption of the 1/7th power law form of the velocity profile proposed by Prandtl [7],

$$\frac{u}{U_\infty} = \left(\frac{y}{\delta}\right)^{1/7}. \quad (1-8)$$

These formulas are in reasonable agreement with turbulent flat-plate data and are appropriate for a general scaling analysis [7].

Turbulent Boundary Layer

To understand the temporal and spatial resolution requirements for the shear stress sensor, we need to understand the relevant time and length scales associated with a turbulent boundary layer. There are two regions in a turbulent boundary layer: the inner layer and outer layer [9]. The semi-log plot of the structure of a typical turbulent boundary layer is shown in Figure 1-4. The outer layer (wake region), is turbulent (eddy) shear-dominated and the effect of the wall is communicated via shear stress. The inner 20% of the boundary layer is defined as the inner layer, where viscous shear dominates. The overlap layer smoothly connects the inner and outer layer. There are three regions within the inner layer:

$0 < y^+ < 5$	viscous sublayer (or linear) region	$u^+ = y^+$
$5 < y^+ < 45$	buffer region	
$45 < y^+ < 0.2\delta^+$	log region	$u^+ = \frac{1}{k} \ln y^+ + B$

where k is the Karman constant and B is the intercept. They are universal constants with $k = 0.41$ and $B = 5.0$ [7]. . The non-dimensional velocity u^+ is defined as

$$u^+ = \bar{u}/u^* , \quad (1-9)$$

where u^* is given by

$$u^* = \sqrt{\tau_w/\rho} , \quad (1-10)$$

\bar{u} is the mean velocity, and ρ is the density of the fluid. The non-dimensional distance y^+ is defined as

$$y^+ = y/l^* = yu^*/\nu , \quad (1-11)$$

where $l^* = \nu/u^*$ is the characteristic viscous length scale. A turbulent flow possesses different length scales. The largest eddies are on the order of the boundary layer thickness, while the smallest eddies can approach the Kolmogorov length scales [8]. Kolmogorov's universal equilibrium theory states that the small scale motions are statistically independent of the slower large-scale turbulent structures, but depend on the rate at which the energy is supplied by large-scale motions and on the kinematic viscosity [8]. In addition, the rate at which energy is supplied is assumed to be equal to the rate of dissipation. Thus, the small eddies must have a smaller time scale and are assumed to be locally isotropic. Therefore, the dissipation rate and kinetic viscosity are parameters governing small scale motions. The scaling relationships between the small and large scale structures in a boundary layer flow are [4, 8, 10]

$$\frac{\eta}{\delta} \sim \left(\frac{u_e \delta}{\nu} \right)^{-3/4} = (Re_\delta)^{-3/4} \quad (1-12)$$

and

$$\frac{Tu}{\delta} \sim \left(\frac{u_e \delta}{\nu} \right)^{-1/2} = (Re_\delta)^{-1/2} , \quad (1-13)$$

where η and T are the Kolmogorov length and time scales respectively, u_e is the eddy velocity (typically $u_e \sim O(0.01U_\infty)$) [4]. Substitution of Equation (1-2) into Equation (1-12) and Equation (1-13) leads to estimates of the Kolmogorov microscales in terms of Re_x ,

$$\eta \sim 20x(Re_x)^{-1/14} \quad (1-14)$$

and

$$T \sim \frac{400x}{U_\infty}(Re_x)^{-4/7} . \quad (1-15)$$

The relationship between the Kolmogorov microscales and Reynolds number is given in Figure 1-5 for a zero pressure gradient turbulent boundary layer with $U_\infty = 50$ m/s, and at a distance $x = 1$ m downstream of the leading edge assuming a $1/7^{th}$ power-law velocity profile.

In order to detect the wall shear stress generated by the smallest eddies in a turbulent boundary layer, the sensor size must be of the same order of magnitude as the Kolmogorov length scale [10], and have a flat frequency range greater than the reciprocal of the Kolmogorov time scale [4]. These microscales are rough estimates, so some researchers used the viscous length scale l^* and time scale, $t^* = \nu/u^{*2}$, to estimate the required sensor size and bandwidth [11, 12]. For example, Padmanabahn et al. [11] used $4l^*$ in their sensor design, and Alfredsson et al.[12] used $10l^*$, $8l^*$ and $2l^*$ in their experiments. Gad-el-Hak and Bandyopadhyay [13] reported these viscous scales are on the same order of the Kolmogorov scales.

If the sensor size is larger than the Kolmogorov length scale, the fluctuating component will be spatially averaged, which results in spectral attenuation and a corresponding underestimation of the turbulent parameters [14, 15]. It has been reported that the sensor smaller than 20 wall units were free from spatial averaging effects [16], while the sensor larger than 30 wall units suffered shear stress underestimation [17]. Equation (1-12) and (1-13) indicate that as

the Reynolds number increases, the sensor size should decrease and the bandwidth of the sensor should increase. For example, at $Re_x = 10^7$, the Kolmogorov length scale is $65 \mu\text{m}$ and the characteristic frequency is 3.7 kHz . From experiments and numerical simulation results, Löfdahl and Gad-el-Hak stated that a sensor size of 3-5 times of Kolmogorov length is reliable for accurate turbulence measurement [10]. A summary of parameters and their analytical expressions for a zero pressure gradient turbulent boundary layer are listed in Table 1-2 [7, 8].

In addition, roughness is another factor that may disturb the turbulent boundary layer. The roughness height due to the flatness of the device die in the package, misalignment in tunnel installation, and gap size is denoted by k_s , and the characterized roughness is given by

$$k_s^+ = \frac{k_s u^*}{\nu}. \quad (1-16)$$

In turbulent flow if $k_s^+ > 5$ the roughness protrudes above the thin viscous layer, causing wall friction to increase significantly [7]. If $k_s^+ < 4$, the wall surface is deemed hydraulically smooth and the roughness does not significantly disturb the turbulent boundary layer [7].

Research Objectives

The goal of this dissertation is to develop a robust, high resolution, and high bandwidth silicon micromachined piezoresistive floating element shear stress sensor for turbulent boundary layer measurement. The shear stress sensor should possess high spatial and temporal resolution and a low minimum detectable signal (MDS). To date, the quantitative, time-resolved, continuous, direct measurement of fluctuating shear stress has not yet been realized [4]. Further effort is required to developed standard, reliable MEMS shear-stress sensors with quantifiable uncertainties. The detailed description of the choice of the piezoresistive sensing scheme is discussed in Chapter 2.

Depending on the application, there are several challenges in the development of this device. An ideal shear stress sensor should have a large dynamic range ($O(80 \text{ dB})$), large bandwidth ($O(10 \text{ kHz})$), and a spatial resolution of $O(100 \text{ }\mu\text{m})$ to capture the spectra of the fluctuating shear stress without spatial averaging. The resolvable shear stress would be on the order of $O(0.1 \text{ mPa})$, resulting in force resolution of $O(10 \text{ pN})$ for the desired spatial resolution of $O(100 \text{ }\mu\text{m})$. In addition, an ideal sensor should be packaged to allow for flush-mounting on the measurement wall surface to avoid flow disturbances.

Traditional intrusive instruments suffer from insufficient spatial and temporal resolution. Microelectromechanical systems (MEMS) technology offers the potential to meet these requirements by extending silicon-based integrated circuit manufacturing approaches to microfabrication of miniature structures [4]. From the perspective of measurement instrumentation, the small physical size and reduced inertia of microsensors vastly improves both the temporal and spatial measurement resolution relative to conventional macroscale sensors. Thus, MEMS shear stress sensors offer the possibility of satisfying transduction challenges associated with measuring very small forces while maintaining a large dynamic range and high bandwidth.

The previous research in MEMS shear stress sensors [18-25] is discussed in detail in Chapter 2. Three transduction schemes have been developed for direct measurement of shear stress: capacitive [18, 21, 24], optical [20, 22, 23] and piezoresistive [19, 25]. These previously developed sensors possess performance limitations and cannot be used for quantitative shear stress measurements.

This research effort is the combination of multidisciplinary design and optimization, fabrication, packaging and calibration, which results in a truly flush-mounted, MEMS direct wall shear stress sensor. The contributions to the above efforts are:

- Development of electromechanical modeling and nonlinear constrained design optimization to achieve good sensor performance for aerospace applications.
- Development and execution of a novel micro-fabrication process accounting for p/n junction isolation and high-quality electrical and moisture passivation.
- Development of a sensor package that can be flush-mounted on the wall surface.
- Realization and preliminary characterization of a functioning device.

Dissertation Overview

This dissertation is organized into seven chapters and five appendices. Chapter 1 provides the motivation for the topic of this dissertation. Background information regarding previous shear stress measurement technology is discussed in Chapter 2. Sensor modeling is discussed in Chapter 3. This includes the electromechanical modeling, finite element analysis for model verification as well as specific design issues. Chapter 4 discusses device optimization subjected to manufacturing constraints and specifications. Chapter 5 describes the detailed fabrication process and device packaging. Experimental characterization setups and results are presented in Chapter 6. The conclusion and future work are presented in Chapter 7.

Information supporting this dissertation is given in appendices. Appendix A provides detailed derivations of the quasi-static beam models and dynamic models. The detailed modeling of the noise floor of the fully active Wheatstone bridge is discussed in Appendix B. A fabrication process flow is presented in Appendix C. The process simulation using FLOOPS [26] is given in Appendix D. The recipes for plasma etching are given in Appendix E. Finally, packaging details, vendors, and engineering drawings are provided in Appendix F.

Table 1-1. Summary of typical skin friction contributions for various vehicles [5].

Vehicles	Typical viscous loss
Supersonic fighter	25-30 %
Large transport aircraft	40 %
Executive aircraft	50 %
Underwater bodies	70 %
Ships at low/high speed	90-30 %

Table 1-2. Parameters in the turbulent boundary layer.

Parameters	Analytical expression
Free stream velocity U_∞ (m/s)	U_∞
Typical eddy velocity u_e (m/s)	$u_e \sim 0.01U_\infty$
Streamwise distance x (m)	x
Kinematic viscosity	ν
Reynolds number based on streamwise distance	$Re_x = \frac{U_\infty x}{\nu}$
Boundary layer thickness δ (m)	$\delta = 0.16x(Re_x)^{-1/7}$
Momentum thickness θ (m)	$\frac{\theta}{\delta} \approx \frac{7}{72}$
Reynolds number based on momentum thickness Re_θ	$Re_\theta = \frac{U_\infty \theta}{\nu}$
Reynolds number based on boundary layer thickness	$Re_\delta = \frac{u_e \delta}{\nu}$
Skin friction coefficient C_f	$C_f = 0.027(Re_x)^{-1/7}$
Wall shear stress τ_w (Pa)	$\tau_w = C_f \frac{1}{2} \rho U_\infty^2$
Kolmogorov length scale η (m)	$\eta \sim \delta(Re_\delta)^{-3/4}$
Kolmogorov time scale T (s)	$T \sim \frac{\delta(Re_\delta)^{-0.5}}{u_e}$

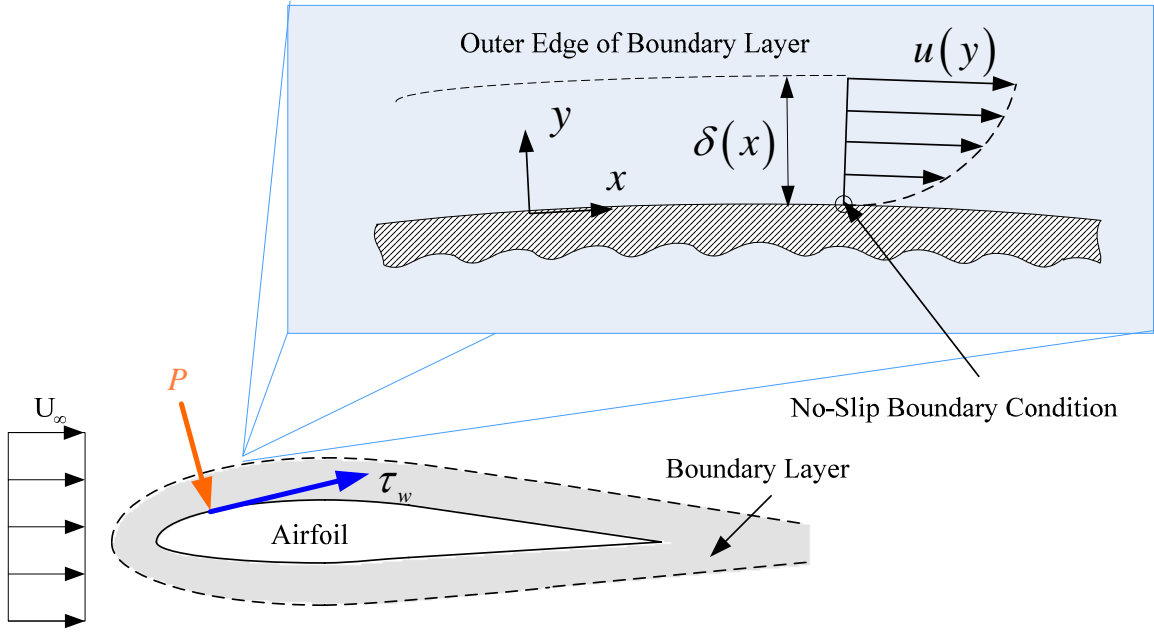


Figure 1-1. Schematic of wall shear stress in a laminar boundary layer on an airfoil section.

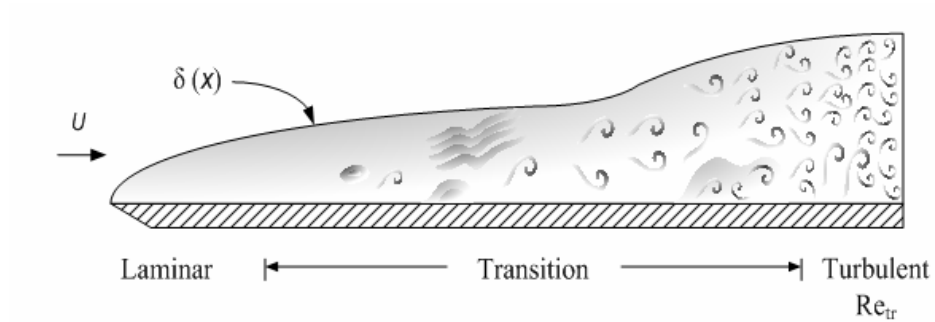


Figure 1-2. Schematic representation of the boundary layer transition process for a flat-plate flow at a ZPG [7].

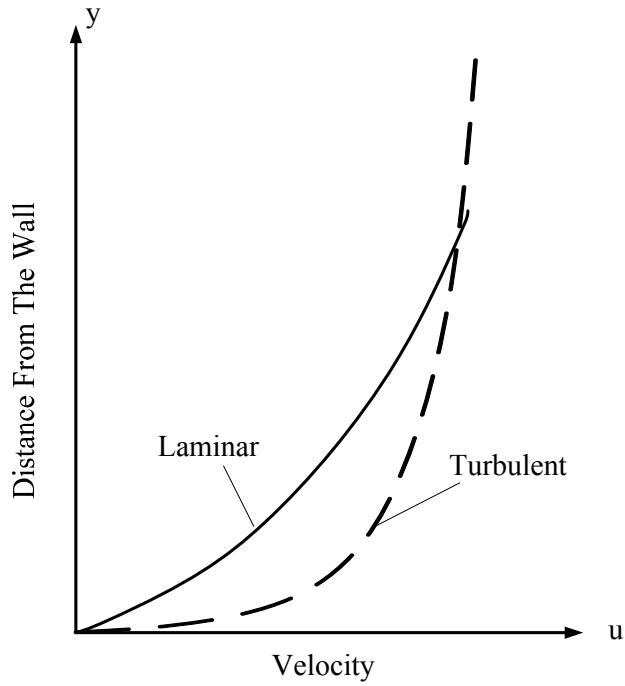


Figure 1-3. Schematic of typical velocity profile for low-speed laminar and turbulent boundary layers [9].

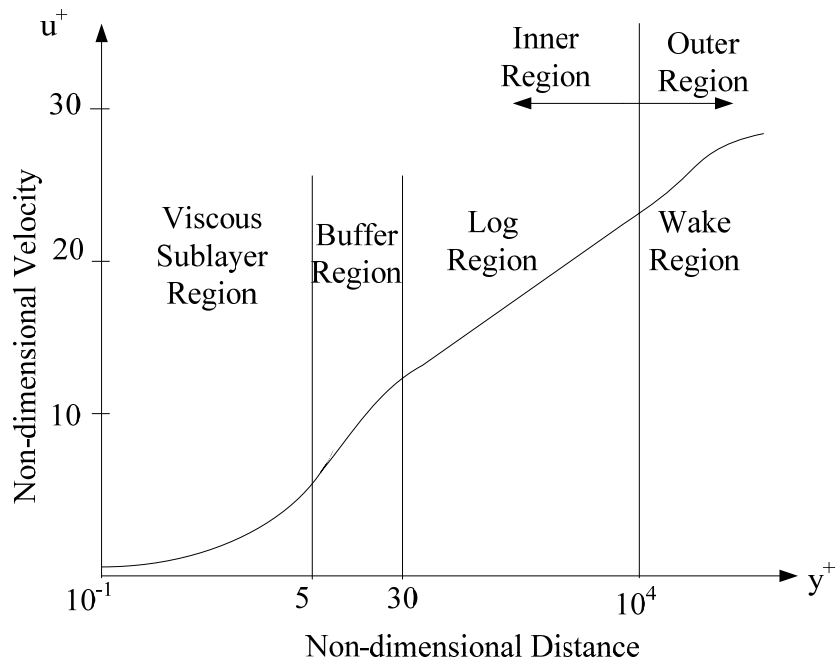


Figure 1-4. The structure of a typical turbulent boundary layer [8].

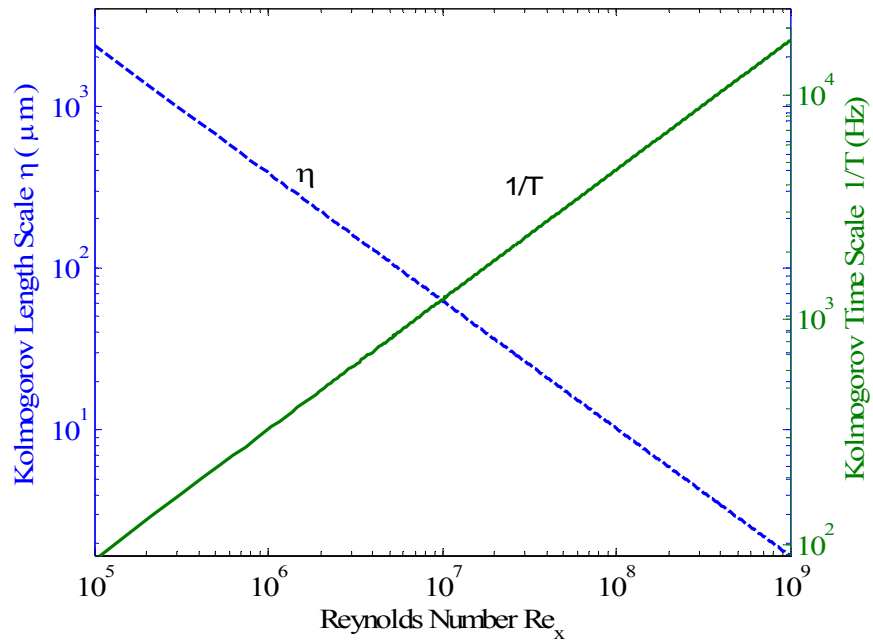


Figure 1-5. Estimates of Kolmogorov microscales of length and time as a function of Reynolds number based on a $1/7^{\text{th}}$ power-law profile.

CHAPTER 2 BACKGROUND

This chapter provides an overview of the techniques for shear stress sensor measurement with a focus on floating element sensors. Previous MEMS shear stress sensors are reviewed and their merits and limitations discussed. A side-implanted piezoresistive shear stress sensor is then proposed to achieve high spatial and temporal resolution and quantifiable uncertainties.

Techniques for Shear Stress Measurement

The current techniques employed in shear stress measurement are grouped into two categories: direct and indirect [27]. Indirect techniques infer the shear stress from other measured flow parameters, such as Joulean heating rate for thermal sensors, velocity profile for curve-fitting techniques or Doppler shift for optical sensors [27]. The uncertainty in these measurements is dominated by the validity of the model relating the flow parameter to wall shear stress [27]. The direct technique measures the integrated shear force generated by wall shear stress on surface [4]. This technique includes three areas: floating-element skin friction balance techniques, thin-oil-film techniques and liquid crystal techniques. The floating-element skin friction balance techniques are addressed in this dissertation. A floating element sensor directly measures the integrated shear force produced by shear stress on a flush-mounted movable “floating” element [27]. Direct measurement techniques are more attractive since no assumptions must be made about the relationship between the wall shear stress and the measured quantity and/or fluid properties. In addition, direct sensors can be used to calibrate indirect devices.

Conventional shear stress sensors and MEMS-based shear stress sensors are described in the following sections, with specific focus on the MEMS floating element technique.

Conventional Techniques

Many conventional techniques have been developed to measure the wall shear stress [28], including indirect measurement techniques such as surface obstacle devices and heat transfer/mass transfer-based devices, and direct measurement techniques such as a floating-element skin friction balance. Several review papers [27-29] catalog the merits and drawbacks of these devices in various flow situations and a wide range of applications. The indirect conventional techniques are summarized in the following paragraph.

Surface obstacle devices include the Preston tube, Stanton tube/razor blade and sub-layer fence. These devices are easy to fabricate and favorable in thick turbulent boundary layers. However, they are sensitive to the size and geometry of the obstacle in the turbulent boundary layer. The device can only measure mean shear stress, and unable to measure the time-resolved fluctuating shear stress. In addition, they rely on an empirical correlation between a 2-D turbulent boundary layer profile and property measured.

Heat transfer/mass transfer-based devices include hot films and hot wires. They have advantages of fast response, high sensitivity and simple structure. However, they are sensitive to temperature drift, have tedious calibration procedures, and suffer calibration repeatability problems due to heat loss to the substrate/air. In general, these devices are considered to be qualitative measurement tools [4].

The direct measurement techniques, known as “skin friction balance” or “floating element balance”, have been widely used in wind tunnel measurements since the early 1950’s [28]. These techniques measure the integrated shear force produced by the wall shear stress on a flush-mounted laterally-movable floating element [29]. The typical device is shown in Figure 2-1. The floating element is attached to either a displacement transducer or to part of a feedback

force-rebalance configuration. Winter [28] cataloged the limitations of this technique, which are summarized as follows:

- Compromise between sensor spatial resolution and detectable shear force.
- Measurement errors associated with misalignment, necessary gap and pressure gradient.
- Cross-axis sensitivity to acceleration, pressure, thermal expansion and vibration.

Some of these limitations can be significantly mitigated if the dimension of the device is reduced, which is a motivation for the development of MEMS floating element sensors.

MEMS-Based Techniques

MEMS is a revolutionary new field that extends silicon integrated circuit (IC) micromachining technology for fabrication of miniature systems. The MEMS-based sensors possess small physical size and large usable bandwidth. The utilization of these devices broadens the spectrum of applications, which range from fundamental scientific research to industrial flow control [6] and biomedical applications [30].

From the fluid dynamics perspective, MEMS-based sensors provide a means of measuring fluctuating pressure and wall shear stress in turbulent boundary layers because the micromachined sensors can be fabricated on the same order of magnitude of the Kolmogorov microscale [10]. Löfdahl and Gad-el-Hak reviewed MEMS-based pressure sensors for turbulent flow diagnosis [10] including background, design criteria, and calibration procedures. Recently, Naughton and Sheplak reviewed modern skin-friction measurement techniques, such as MEMS-based sensors, thin-oil film interferometry and liquid crystal coatings. They summarized the theory, development, limitations, uncertainties and misconceptions surrounding these techniques [4].

Several microfabricated shear stress sensors of both direct and indirect types have been reported. The indirect MEMS wall shear-stress sensors include thermal devices [31-34], laser-

based sensors [35], micro-pillars [36, 37] and micro-fences [38]. Thermal shear stress sensors operate on heat transfer principles. Laser Doppler sensors operate on the measurement of Doppler shift of light scattered by particles passing through a diverging fringe pattern in the viscous sublayer of a turbulent boundary layer to yield the velocity gradient. Micro-pillars are based on a sensor film with micropillars arrays that are essentially vertical cantilever arrays within the viscous sublayer. These sensors employ optical techniques to detect the wall shear stress in the viscous sublayer via pillar tip deflection. Micro-fences employ a cantilever structure to detect the shear stress via piezoresistive transduction.

Direct shear stress sensors include floating-element devices [18-25]. Three transduction schemes have been used in floating element sensors: capacitive [18, 21, 24], piezoresistive [19, 25] and optical [20, 22, 23].

Floating Element Sensors

Sensor Modeling and Scaling

The typical MEMS floating element shear stress sensor is shown in Figure 2-2. The floating element, with a length of L_e , width of W_e and thickness of T_e , is suspended over a recessed gap by four silicon tethers. These tethers act as restoring springs. The shear force induced displacement Δ of the floating element is determined by Euler-Bernoulli beam theory to be [11] (the detailed derivation is given in Appendix A)

$$\Delta = \frac{\tau_w L_e W_e}{4ET_e} \left(\frac{L_t}{W_t} \right)^3 \left(1 + \frac{2L_t W_t}{L_e W_e} \right), \quad (2-1)$$

where L_t , W_t and T_t are tether length, width and thickness respectively, and E is the elastic modulus of tether material. The mechanical sensitivity of the sensor with respect to the applied

shear force, $F = \tau_w W_e L_e$, is directly proportional to the mechanical compliance of the tethers $1/k$ [18]

$$C_y = \frac{1}{k} = \frac{\Delta}{F} = \frac{1}{4ET_t} \left(\frac{L_t}{W_t} \right)^3 \left(1 + \frac{2L_t W_t}{L_e W_e} \right). \quad (2-2)$$

The trade-off associated with spatial resolution versus decreasing shear stress sensitivity is illustrated in Equation (2-1) and Figure 2-3. For example, a sensor with floating element area of $100 \mu\text{m} \times 100 \mu\text{m}$, the integrated shear force is $O(10 \text{ pN})$ for a shear stress of $O(1 \text{ mPa})$, which requires the tethers to have a high compliance to get an appreciable element detection. The compliance is limited by the maximum shear stress achievable before failure occurs or before nonlinearity in the force-displacement relationship [4] becomes substantial. The minimum detectable shear stress is determined by the sensitivity and the total sensor noise [39].

Assuming a perfectly damped or under-damped system, the bandwidth is proportional to the first resonant frequency, $\sqrt{k/M}$, where M is the effective mass,

$$M \approx \rho L_e W_e T_t, \quad (2-3)$$

where ρ is the density of the floating element material and it is assumed that $L_e W_e \gg L_t W_t$.

Therefore, the shear stress sensitivity-bandwidth product is obtained as

$$\frac{1}{\sqrt{kM}} \propto \sqrt{\frac{1}{4E\rho L_e W_e T_t^2} \left(\frac{L_t}{W_t} \right)^3}. \quad (2-4)$$

The sensitivity-bandwidth product is a parameter useful in investigations of the scaling of mechanical sensors. MEMS technology enables the fabrication of sensors with small thickness and low mass, in addition to large compliance and a superior sensitivity-bandwidth product comparable to conventional techniques [4]. A MEMS floating element has lengths of

$L_e = W_e = O(1000 \mu\text{m})$ and $T_t = O(10 \mu\text{m})$, whereas conventional floating element lengths are $L_e = W_e = O(1 \text{ cm})$. Therefore, with the scaling of mass alone, MEMS-based sensors have a sensitivity-bandwidth product at least three-orders of magnitude larger than conventional sensors. MEMS-based sensors also possess spatial resolution at least one-order of magnitude higher than conventional sensors, which is vital for turbulence measurements to avoid spatial averaging [4].

Error Analysis and Challenges

Compared to conventional techniques, MEMS shear stress sensors have a negligible misalignment error. This error is limited by the flatness of the device die [18] because the floating element, tethers and substrate are fabricated monolithically in the same wafer. Other sources of misalignment include packaging and tunnel installation, with packaging the dominant source [4]. Packaging-induced compressive or tensile force may drastically alter the device sensitivity [18]. The necessary gap between the wall and floating element is also reduced, with a typical gap size smaller than $5 \mu\text{m}$ [4].

Effect of misalignment

Misalignment of the floating element results in the element not being perfectly flush-mounted with the wall surface, which disturbs the flow field around the sensor. The effective shear stress is estimated by integrating the “stagnation pressure (ρu_y^2)” over the floating element surface and dividing by the element area [39] to get

$$\tau_{MA} = \frac{\rho \int_0^{k_s} u_y^2 dz}{L_e}, \quad (2-5)$$

where k_s is the height of protrusion or recession above or below the wall. Streamwise velocity u_y is obtained via relationship between shear stress and velocity gradient in the sublayer,

$$\tau_w = \mu \frac{u_y}{z}, \quad (2-6)$$

where ρ and μ are the density and dynamic viscosity of the fluid, respectively, and z is the distance from the wall. Substituting Equation (2-6) into Equation (2-5) to obtain the effective shear stress yields

$$\tau_{MA} = \frac{1}{3} \frac{\rho k_s^3 \tau_w}{\mu^2 L_e}. \quad (2-7)$$

For a sensor with $L_e = 1000 \mu\text{m}$, $k_s = 10 \mu\text{m}$ under the surface, and $\tau_w = 5 \text{ Pa}$ in air, the misalignment error is about 0.12%. Therefore it may be neglected.

Effect of pressure gradient

Error due to a pressure gradient is also greatly decreased for MEMS sensors. As illustrated in Figure 2-4, there are two sources which introduce pressure gradient errors; one is the recessed gap beneath the floating element and the other is the net pressure force acting on the lip of the floating element [26]. The net force acting on the lip of the floating element is given as

$$F_p = T_i W_e \Delta P = T_i W_e \frac{dP}{dy} L_e. \quad (2-8)$$

The associated effective shear stress is obtained by dividing by the sensor area, $W_e L_e$,

$$\tau_p = \frac{dP}{dy} T_i. \quad (2-9)$$

The pressure gradient also introduces a shear stress underneath the floating element that can be estimated to first-order by assuming fully-developed Poiseuille flow,

$$\tau_g = \frac{g}{2} \frac{dP}{dy}, \quad (2-10)$$

where g is the height of the recessed gap beneath the floating element. The total effective shear stress acting on the floating element is

$$\tau_{eff} = \tau_w + \frac{dP}{dy} \left(T_t + \frac{g}{2} \right) = \tau_w \left(1 + \beta \left(\frac{T_t}{\delta^*} + \frac{g}{2\delta^*} \right) \right), \quad (2-11)$$

where $\beta = \frac{\delta^*}{\tau_w} \frac{dP}{dy}$ is called Clauser's equilibrium parameter, which is employed to compare the external pressure gradient to wall friction in a turbulent boundary layer [7]. The displacement thickness δ^* is a parameter quantifying the mass flux deficit due to viscous effects. As indicated in Equation (2-11), the error is dependent on the gap size and thickness of the floating element and independent of the size of the floating element. The smaller gap and thickness of the MEMS sensors result in smaller errors compared to conventional floating element sensors; the MEMS sensors provide approximately a two-order of magnitude improvement in lip force induced error. To get a more accurate estimate of these errors, direct numerical simulation of the flow around the sensor is required.

Effect of cross-axis vibration and pressure fluctuations

Errors due to stream-wise acceleration scale favorably for low mass MEMS sensors [28].

The equivalent shear stress due to acceleration is approximated as

$$\tau_a = \frac{F}{A_f} = \frac{Ma}{A_f} = \frac{\rho W_e L_e T_t a}{W_e L_e} = \rho T_t a, \quad (2-12)$$

where a is the acceleration and A_f is the surface area of the floating element, respectively.

Equation (2-12) indicates that the effective shear stress due to stream-wise acceleration is proportional to the tether thickness. Assuming the stream-wise acceleration is 1 g, for a

proposed optimum sensor design with element dimensions of $1000 \mu\text{m} \times 1000 \mu\text{m} \times 50 \mu\text{m}$, and the tethers dimension of $1000 \mu\text{m} \times 30 \mu\text{m} \times 50 \mu\text{m}$, the effective stress is found to be 1.14 Pa in the y -direction. Depending on the aerodynamic body acceleration levels, local acceleration measurements in conjunction with coherent power data analysis may be used to mitigate acceleration effects [40]. The stream-wise deflection is obtained from

$$\delta_c = \frac{Ma}{k_c} = MaC_y. \quad (2-13)$$

where k_c and C_y are the stream-wise stiffness and compliance of the tethers, respectively.

Therefore, the stream-wise acceleration sensitivity is proportional to C_y . Assuming flow over the floating element in the y -direction (Figure 2-4), the cross-axis compliances according to small-deflection beam theory are

$$C_x = \frac{L_t}{4EW_tT_t} \quad (2-14)$$

and

$$C_z = \frac{1}{4EW_t} \left(\frac{L_t}{T_t} \right)^3. \quad (2-15)$$

The ratios of transverse compliances to compliance in the flow direction are

$$\frac{C_y}{C_x} = \left(\frac{L_t}{W_t} \right)^2 \quad (2-16)$$

and

$$\frac{C_y}{C_z} = \left(\frac{T_t}{W_t} \right)^2. \quad (2-17)$$

If $T_t, W_t \sim O(50 \mu\text{m})$ and $L_t \sim O(1 \text{ mm})$, the compliance in the x -direction is four orders of magnitude less than the compliance in the flow direction (y -direction). Since the deflection is proportional to the compliance in the associated direction, the transverse deflection (x -direction)

is four-orders of magnitude smaller than in the flow direction (y -direction). Therefore, the transverse acceleration effect in x -direction is negligible. However, the compliances in the z - and y -directions are of the same order, and thus transverse acceleration effects in the z direction must be taken into account. This can be mitigated by using piezoresistive transduction scheme via a fully-active Wheatstone bridge configuration. The transverse acceleration and pressure in the z -direction supplies a common mode signal to the Wheatstone bridge, which can be rejected by the differential voltage output. It is critical to minimize the pressure sensitivity as pressure fluctuations in wall-bounded turbulent flows are much larger in magnitude than wall shear stress fluctuations [41]. Hu et al. [41] found that the wall pressure fluctuations is 7–20 dB (depending on frequency) higher than the fluctuations for the streamwise wall shear stress, and 15–20 dB higher than that for spanwise component. The detailed discussion is given in Chapter 3.

Previous MEMS Floating Element Shear Stress Sensors

Previous research in the floating element shear stress sensor is reviewed in this section. This review is divided into capacitive, optical and piezoresistive sensing in terms of transduction schemes. Their respective performance merits and drawbacks are discussed.

Capacitive Shear Stress Sensors

Realizing the merits of scaling shear stress sensors to the microscale, Schmidt et al. [18, 39] first reported the development of a micromachined floating element shear stress sensor with an integrated readout for applications in low speed turbulent boundary layers, As shown in Figure 2-5, the sensor was comprised a square floating element ($500\ \mu\text{m} \times 500\ \mu\text{m} \times 32\ \mu\text{m}$) suspended by four tethers ($1000\ \mu\text{m} \times 5\ \mu\text{m} \times 32\ \mu\text{m}$) and fabricated using polyimide/aluminum surface micromachining techniques. A differential capacitive scheme was employed to sense the

deflection of the floating element. This differential capacitive scheme is insensitive to the transverse movement to first order. The sensor was calibrated in a laminar flow using dry compressed air up to a shear stress of 1 Pa . The achieved minimum detectable shear stress was 0.1 Pa with a bandwidth of 10 kHz . The measurement data was in agreement with the design model. However, the sensor was sensitive to electromagnetic interference (EMI) due to the high input impedance, and suffered from the sensitivity drift due to moisture-induced polyimide property variation. In addition, the capacitive sensing scheme was limited to nonconductive fluids.

Pan et al. [21, 42] presented a force-feedback capacitive design that monolithically integrated sensing, actuation and electronics control on a single chip using polysilicon-surface-micromachining technology. The sensor has a comb finger structure with folded beam suspension. The folded beam provided higher sensitivity and internal stress relief. The floating element motion was measured by a differential capacitive sensing scheme while the folded beam served as mechanical springs (Figure 2-6). A linear measurement sensitivity of 1.02 V/Pa over a pressure range of 0.5 to 3.7 Pa was achieved in a 2-D continuum laminar flow channel. No dynamic response, linearity and noise floor results were reported. In addition, the front wire bonds may disturb the flow in turbulent flow measurements.

Zhe et al. [24] developed a floating element shear stress sensor using a differential capacitive sensing technique, with an optical technique as a self-test. The sensor was fabricated on an ultra-thin (50 μm) silicon wafer using wafer bonding and DRIE techniques. As shown in Figure 2-7, the sensor consisted of two sensor electrodes, two actuation electrodes, a floating element (200 μm in width and 500 μm in length) and a cantilever beam (3 mm in length). The shear stress was detected by a cantilever beam deflection, with a mechanical sensitivity of

1 $\mu\text{m}/\text{Pa}$. This sensor was capable of measuring a shear force as small as 5 nN that corresponded to a shear stress of 50 mPa . The static calibration in a rectangular channel shows a minimum detectable shear stress of 0.04 Pa with 8% uncertainty up to 0.2 Pa , which is the limit of the calibration technique. No frequency response results were reported.

Optical Shear Stress Sensors

Padmanabhan et al. [20] developed two generations of differential optical shutter-based floating element sensors for turbulent flow measurement. As shown in Figure 2-8, the floating element ($120\ \mu\text{m} \times 120\ \mu\text{m} \times 7\ \mu\text{m}$ and $500\ \mu\text{m} \times 500\ \mu\text{m} \times 7\ \mu\text{m}$) is suspended $1.0\ \mu\text{m}$ above the silicon substrate by four tethers. Two photodiodes were integrated into the substrate under the leading and trailing edges of the opaque floating element. The floating element motion induced by shear force causes the photodiodes shuttering. Under uniform illumination from above, the normalized differential photocurrent is proportional to the lateral displacement of the element and the wall shear stress. The sensor could measure a wall shear stress from 3 mPa up to 10 Pa , with a sensitivity of $0.4\ \text{V}/\text{mPa}$ (without integration of detection electronics). The dynamic response of the sensor was quantified up to the characterization limit of 4 kHz [43]. The measured shear stress was consistent with predicted theoretical values. The sensor showed very good repeatability, long-term stability, minimal drift, and EMI immunity. The main drawback to this sensor was that vibrations of the light source relative to the sensor resulted in erroneous signals.

Tseng et al. [22] developed a novel Fabry-Perot shear stress sensor that employed optical fibers and a polymer MEMS-based structure. The sensor was micromachined using micromolding, UV lithography and RIE processes. As shown in Figure 2-9, a membrane was used to protect the inner sensing parts and support the floating element displacement

measurement. The displacement of the floating element (400 μm high, 200 μm wide) induced by the wall shear stress on the membrane (1.5 mm \times 1.5 mm \times 20 μm) was detected via an optical fiber using Fabry-Perot interferometer. The sensor was tested in a steady laminar flow between parallel plates and the results demonstrated a shear stress resolution of 0.65 Pa/nm. The minimum detectable shear stress was 0.065 Pa. The fragile sensing parts were not exposed to the testing environment, making the sensor suitable for applications in harsh environments. This sensor was not tested in flows. The dynamic response and linearity of this sensor are questionable due to the potential buckling of diaphragm. Furthermore, cross-axis sensitivity due to vibration and pressure may be significant given the geometry of the sensing element.

Horowitz et al. [23] developed a floating-element shear stress sensor based on geometric Moiré interferometer (Figure 2-10). The device structure consisted of a silicon floating element (1280 μm \times 400 μm \times 10 μm) suspended 2.0 μm above a Pyrex wafer by four tethers (545 μm \times 6 μm \times 10 μm). The sensor was fabricated via DRIE and a wafer bonding/thin back process. When the device was illuminated through the Pyrex, light was reflected by the top and bottom gratings, creating a translation-dependent Moiré fringe pattern. The shift of the Moiré fringe was amplified with respect to the element displacement by the ratio of fringe pitch G to the movable grating pitch g_2 . The sensor die was flush-mounted on a Lucite plug front side, and the imaging optics and a CCD camera was installed on the backside for the displacement measurement. Experimental characterization indicated a static sensitivity of 0.26 $\mu\text{m}/\text{Pa}$, a resonant frequency of 1.7 kHz, and a noise floor of 6.2 mPa/ $\sqrt{\text{Hz}}$. Drawbacks to this sensor included an optical packaging scheme not feasible for wind tunnel measurement and limited bandwidth.

Piezoresistive Shear Stress Sensors

Shajii et al. [19] and Goldberg et al. [44] extended Schmidt's work to develop a piezoresistive based floating element sensor for polymer extrusion feedback control (Figure 2-11). The polyimide/aluminum composite floating element was replaced by single crystal silicon. These sensors were designed for operation in high shear stress (1 kPa – 100 kPa), high static pressure (up to 40 MPa) and high temperature (up to 300 °C) flow conditions. The floating element size was 120 μm \times 140 μm in Ng's design, and 500 μm \times 500 μm in Goldberg's design. The element motion was sensed by axial surface piezoresistors in the tethers via configuration these piezoresistors to a half Wheatstone bridge. This sensor was not suitable for turbulent flow measurement due to low sensitivity as it was designed for maximum shear-stress levels 5 orders-of-magnitude larger than those in a typical turbulent flow. However, Goldberg et al. [44] developed a backside contact structure to protect the wire-bonds from the harsh external environment, which reduced the flow disturbance and associated measurement uncertainty for turbulence measurement.

Barlian et al [25] developed a piezoresistive shear stress sensor for direct measurement of shear stress underwater. The sidewall-implanted piezoresistors measured the integrated shear force, and the top-implanted piezoresistors detected the pressure (Figure 2-12). The displacement of the floating element was detected using a Wheatstone bridge. The experimental measurements indicated the in-plane force sensitivity ranged from 0.041 – 0.063 mV/Pa, while the predicted sensitivity was 0.068 mV/Pa. The transverse sensitivity was 0.04 mV/Pa with a corresponding transverse resonant frequency of 18.4 kHz. This was done by using a mechanical cantilever as an input. The dynamic analysis was performed using a laser Doppler vibrometer with a piezoelectric shaker to drive the in-plane or out-of-plane motion. The in-plane resonant

frequency was experimentally found to be 19 kHz compared to a predicted value of 13.4 kHz . The integrated noise floor was 0.16 μV over bandwidth of 1 Hz –100 kHz . The sensitivity of the piezoresistors to changes in temperature was investigated in a de-ionized (DI) water bath, and the temperature coefficient of sensitivity was found to be 0.0081 $\text{k}\Omega/^{\circ}\text{C}$. No electrical characteristics of p/n junction isolation and flow characterization are reported and no fluid mechanics characterization was performed.

A Full-Bridge Side-Implanted Piezoresistive Shear Stress Sensor

According the above discussion, the most successful MEMS floating element sensor to date used integrated photodiodes to detect the lateral displacement via a differential optical shutter [20]. This sensor can detect the shear stress as low as 1.4 mPa . However, it is not suitable for wind tunnel testing because the sensing system is sensitive to tunnel shock and vibration. The capacitive transduction technique integrated the mechanical sensor and electronics on one chip to eliminate the parasitic capacitance [45], and has the capability to measure small signals. Unfortunately, the sensitivity drifted due to the charge accumulation in the electrodes [18], which can be mitigated by hermetic sealing [46] or by employing metal electrodes. However, the shear stress sensor must be exposed to the flow for shear stress measurement and wind tunnels are typically not humidity controlled environments.

The piezoresistive transduction scheme is widely used in commercial pressure sensors and microphones due to its low cost, simple fabrication, and higher reliability than capacitive transduction. In addition, piezoresistive technology can resolve sufficiently small forces up to $O(10^{-15}\text{ N})$ [47]. Shajii et al. [19] proposed a backside-contact, piezoresistive sensor to measure very high shear stress in a polymer extruder. Axial mode piezoresistive transducers [19, 25] for high-shear industrial applications have been fabricated using standard ion-implantation

techniques, but more sensitive bending-mode transducers require that the piezoresistors be located on the tether sidewall. This concept has been proposed by Sheplak et al.[48] and applied by Barlian et al. who presented an integrated pressure/shear stress sensors for underwater applications [25]. The authors did not present a comprehensive fluid-induced shear stress characterization of their sensor. Rather, the sensor was statically characterized using a mechanical cantilever and dynamically characterized using an acceleration input. In a conference paper, the authors presented some water flow results possessing a large uncertainty and an unexplained sensitivity that was larger than the value predicted by beam mechanics [49].

None of these devices have successfully transitioned to wind tunnel measurement tools because of performance limitations and/or packaging impracticalities [2]. For use in a wind tunnel, the sensor package must be flush mounted in an aerodynamic model, robust enough to tolerate humidity variations and immune to electromagnetic interference (EMI). We have attempted to address these limitations via the development of a fully-active Wheatstone bridge side-implanted piezoresistive sensor. This approach was motivated by the following two side-implanted piezoresistive transducer concepts. Chui et al. [50] first presented a dual-axis piezoresistive cantilever using a novel oblique ion implantation technique. Later, Partridge et al. [51] leveraged the side-implant process to fabricate a high performance lateral accelerometer.

The device structure developed in this dissertation is illustrated in Figure 2-13 which shows an isometric view of the floating element, sidewall implanted p-type silicon piezoresistors, heavily doped end-cap region, and bond pads. In this transduction scheme, the integrated force produced by the wall shear stress on the floating element causes the tethers to deform and thus induces a mechanical stress field. The piezoresistors respond to the stress field with a change in resistance from its nominal, unstressed value due to a change in the mobility (or number of

charge carriers) within the piezoresistor [52]. The conversion of the shear stress induced resistance change into an electrical voltage is accomplished via configuration of the piezoresistors into a fully-active Wheatstone bridge to increase the sensitivity of the circuit compared to half bridge configuration. This bridge requires the presence of a bias current through the piezoresistors, typically, it is driven by constant voltage excitation. This sensor is designed to measure shear stress only and to mitigate pressure sensitivity. An on-chip dummy bridge located next to the sensor is used for temperature corrections.

Ideally, common mode disturbances do not have any effect while differential disturbances are linearly converted into the bridge output. To achieve a differential signal, the piezoresistors are oriented such that the resistance modulation in each resistor of a given leg is equal in magnitude but opposite in sign. These conditions are achieved by placing the side implanted resistors facing one another such that when one resistor is in tension, the other is in compression. This results in equal mean resistance but opposite perturbation.

Once the transduction scheme is selected, the mechanical models and transduction sensing models need to be developed to get sensor performance, such as sensitivity, linearity, bandwidth, noise floor, dynamic range, MDS. The detailed discussion of the electromechanical modeling is given in Chapter 3.

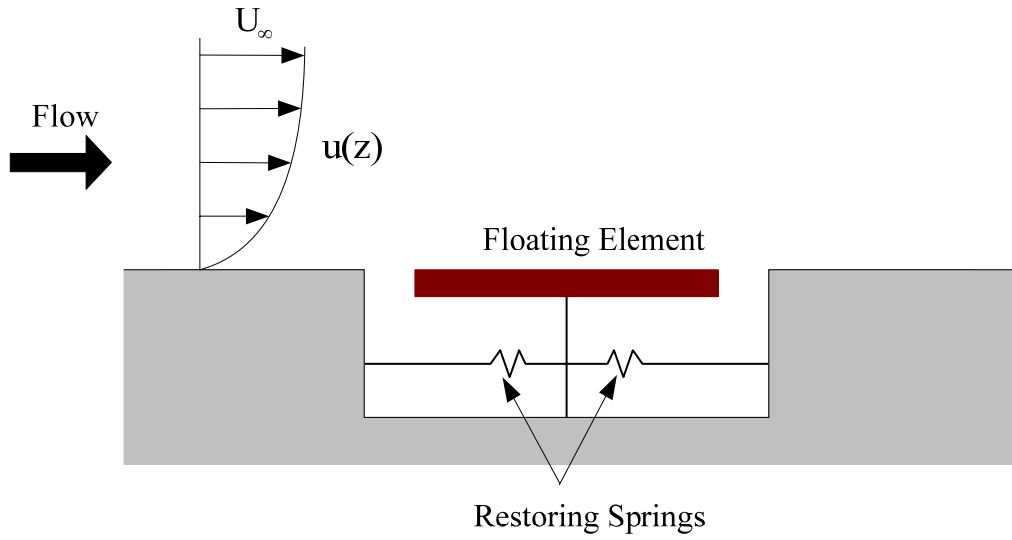


Figure 2-1. Schematic cross-sectional view of the floating element based sensor.

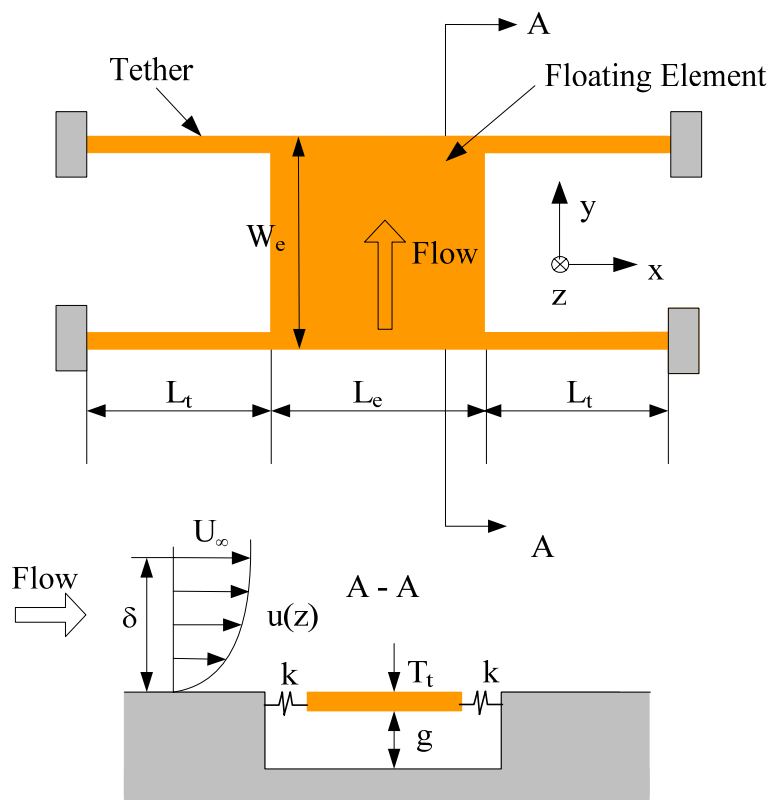


Figure 2-2. Schematic plan view and cross-section of a typical floating element sensor [4].

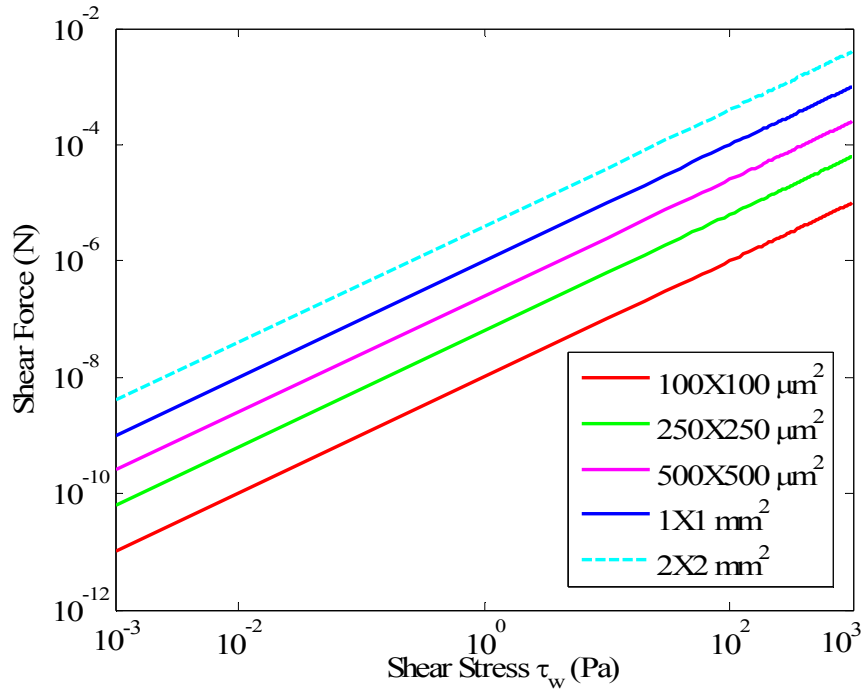


Figure 2-3. Integrated shear force variation as a function of sensor resolution for different element areas.

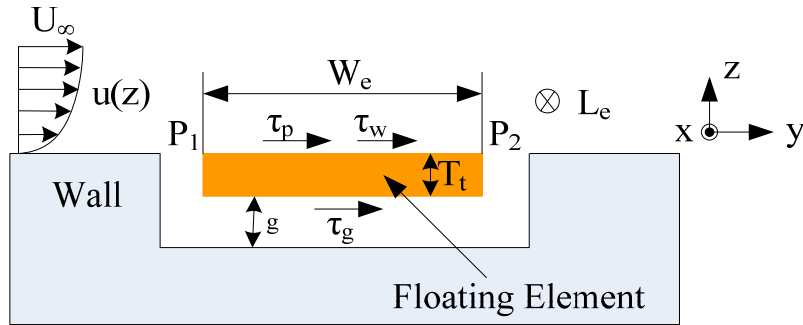


Figure 2-4. Schematic illustrating pressure gradient effects on the force balance of a floating element.

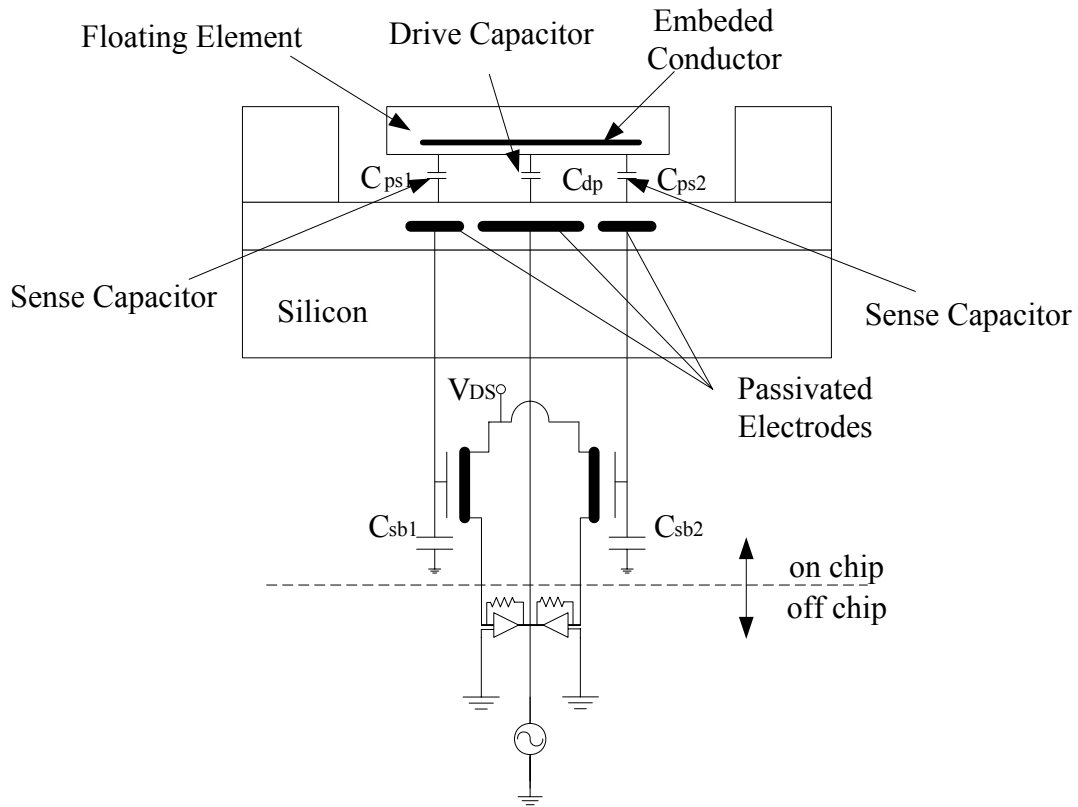


Figure 2-5. Schematic cross-sectional view of the capacitive floating element sensor developed by Schmidt et al. [18].

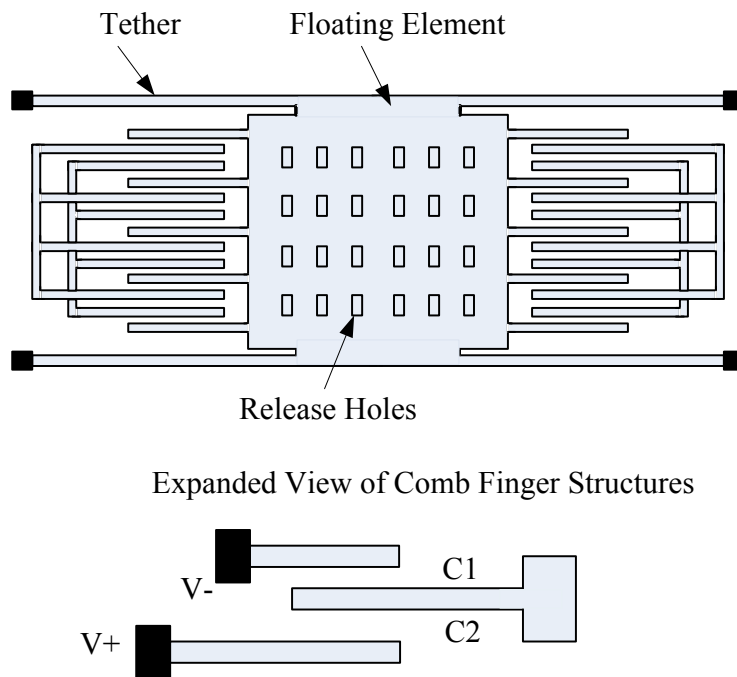


Figure 2-6. Plan-view of a horizontal-electrode capacitive floating element sensor [21].

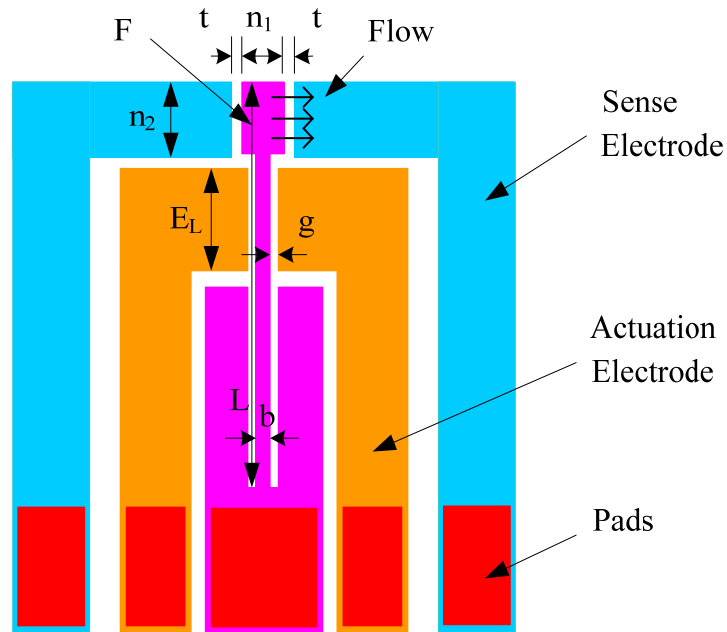


Figure 2-7. Schematic top-view of a differential capacitive shear stress sensor [24].

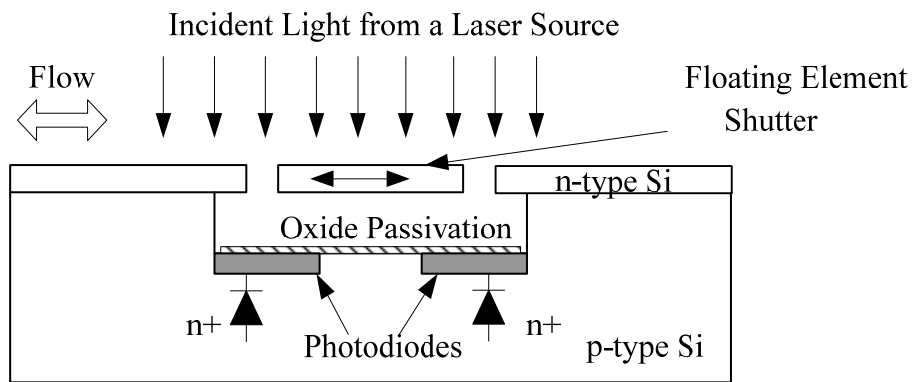


Figure 2-8. A schematic cross-sectional view of an optical differential shutter-based floating element shear stress sensor [11].

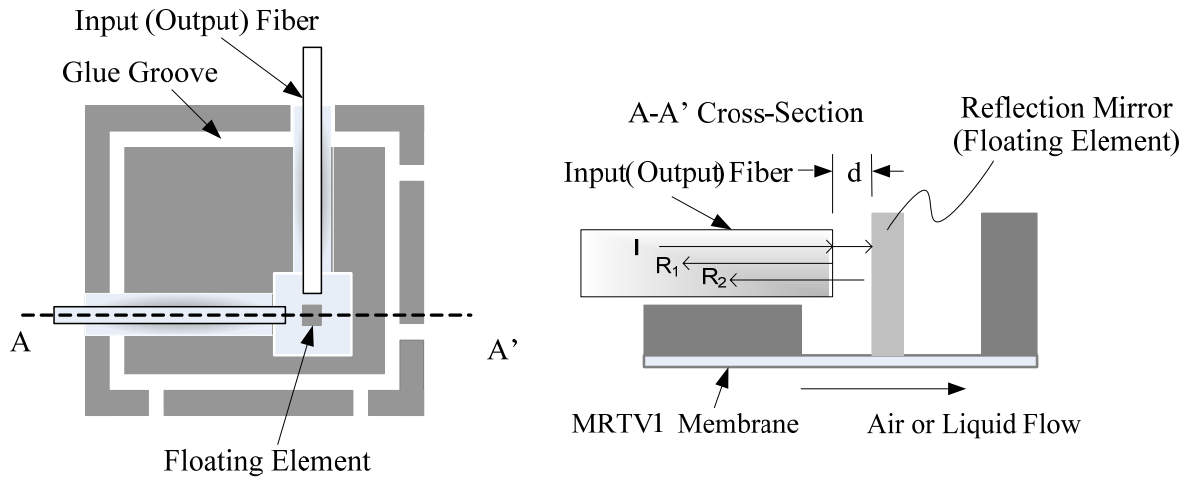


Figure 2-9. Schematic top and cross-sectional view of a Fabry-Perot shear stress sensor [22].

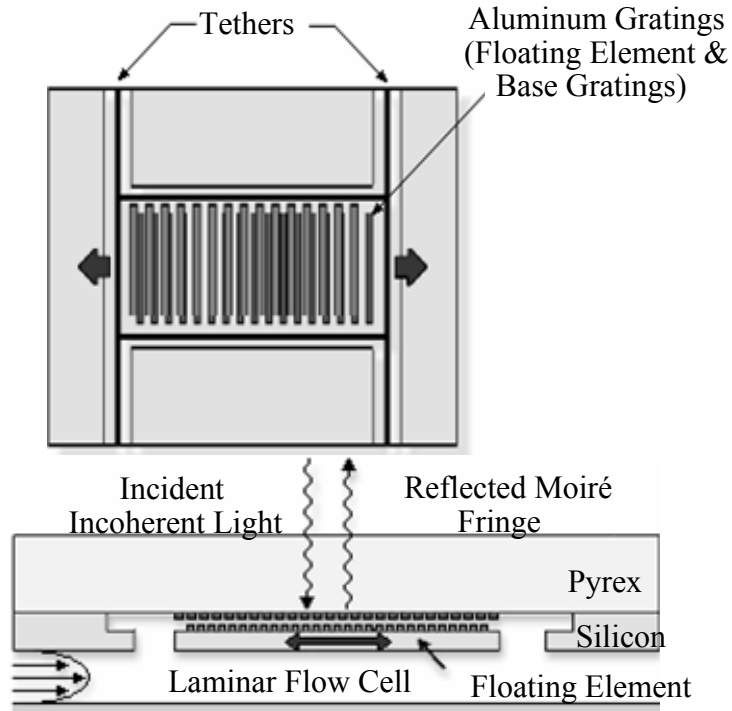


Figure 2-10. Top and cross-sectional view of Moiré optical shear stress sensor [23].

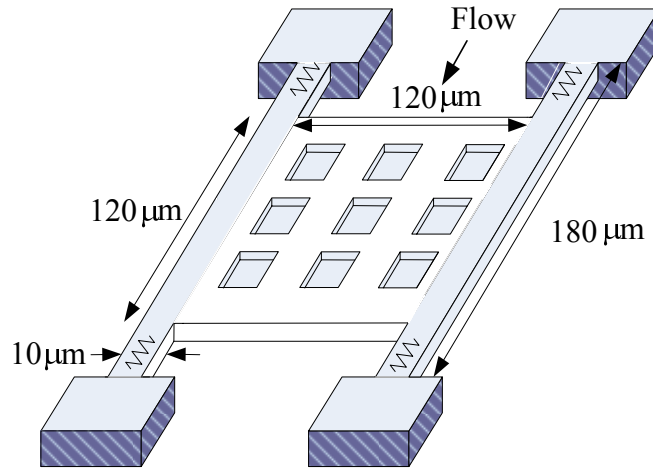


Figure 2-11. A schematic top view of an axial piezoresistive floating element sensor [19].

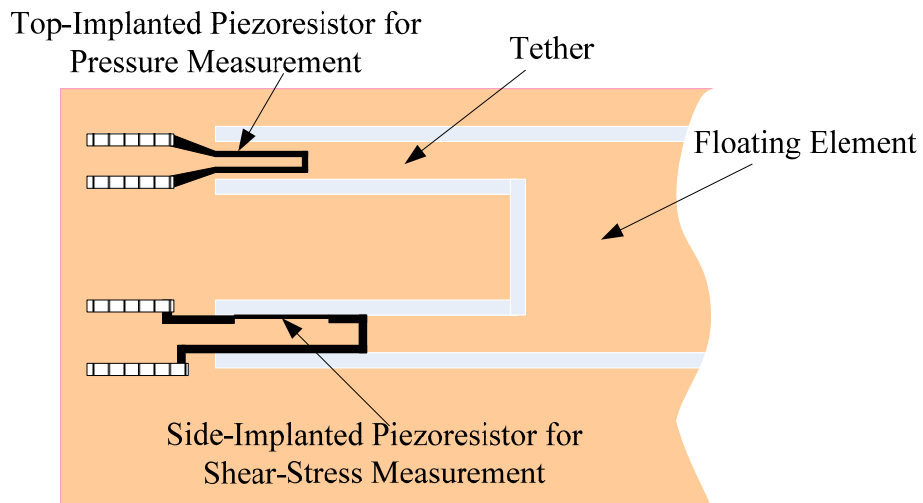


Figure 2-12. A schematic top view of a laterally-implanted piezoresistive shear stress sensor [25].

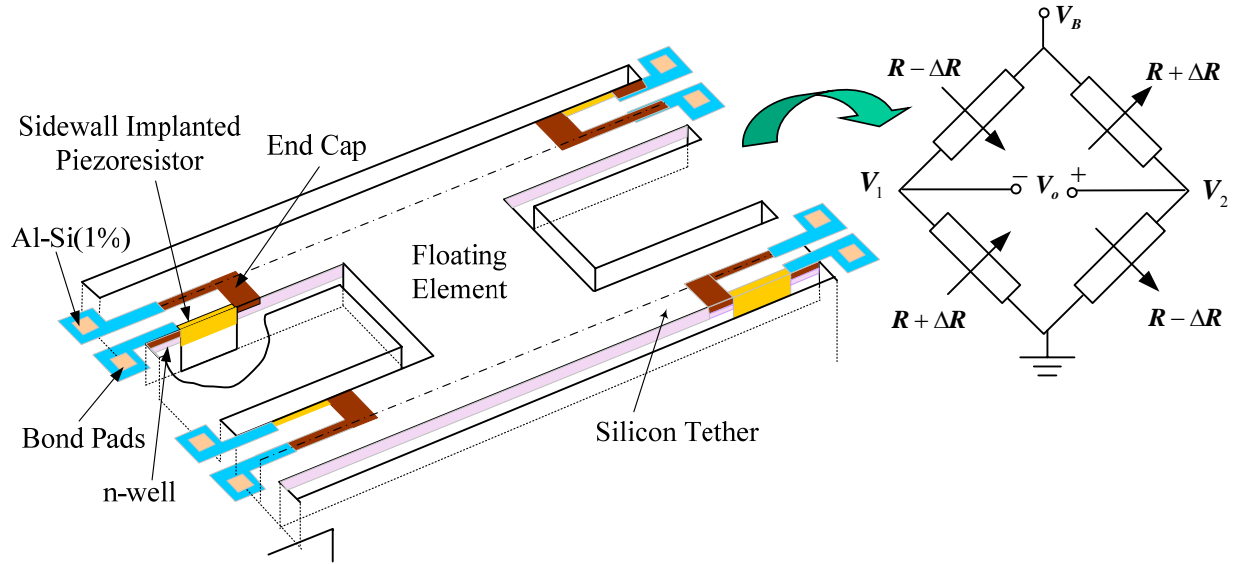


Figure 2-13. A schematic 3D view of the side-implanted piezoresistive floating element sensor.

CHAPTER 3 SHEAR STRESS SENSOR MODELING

This chapter presents the electromechanical modeling of the MEMS side-implanted piezoresistive shear stress sensor. These models are leveraged for use in finding an optimal sensor design (detailed discussion in Chapter 4). Formulation of the objective function for performance optimization begins with structural and electronic device models of the shear stress sensors. The structural response directly determines the mechanical sensitivity, bandwidth, and linearity of the dynamic response. The piezoresistor design determines the overall sensitivity and contributes to the electronic noise floor of the device. The organization of this chapter is as follows.

First, the mechanical modeling is discussed, including quasi-static modeling and dynamic response analysis. Linear and non-linear quasi-static behaviors are presented. Lumped element modeling is employed to find the dynamic behavior of the sensor. These analytical models were verified using finite element analysis (FEA) in CoventorWare[®].

Second, the piezoresistive sensing electromechanical model is developed, where the resistance and piezoresistive sensitivity for non-uniform doping are derived via stress averaging and a conductance-weighted piezoresistance coefficient. Two dominant electrical noise sources in the piezoresistive shear stress sensor, $1/f$ noise and thermal noise, as well as amplifier noise are considered to determine the noise floor.

Finally, some device specific issues are addressed, including transverse sensitivity, acceleration sensitivity, pressure sensitivity, junction isolation issues and temperature compensation via a dummy bridge.

Quasi-Static Modeling

In this section, the sensor structure is discussed and modeled. Quasi-static models for small and large floating element deflections that make use of Euler-Bernoulli beam theory and the von Kármán strain assumption, respectively, are presented. Two methods are used in large deflection analysis, an energy method and an exact analytical method.

Structural Modeling

Floating element sensors are composed of four tethers and a square floating element. A schematic of the piezoresistive shear stress sensor is shown in Figure 3-1. The floating element is suspended above the surface of the silicon wafer by tethers, each of which is attached at its end to the substrate. Side-implanted boron in the sidewalls of the tethers forms the four piezoresistors. These resistors are aligned in the $\langle 110 \rangle$ direction and located near the edge zone of the tethers to achieve the maximum sensitivity. Two resistors are oriented along opposite sides of each tether. When the fluid flows over the floating element, the integrated shear force causes the tethers to deform and induces a bending stress.

For the mechanical analysis, the floating elements and tethers are assumed to be homogeneous, linearly elastic, and symmetric. In practice, this is not strictly valid as the beam is partially covered by thin silicon dioxide and silicon nitride layers. The floating element is assumed to move rigidly under the applied shear stress, and the motion is permitted in-plane only. The tethers are assumed to be perfectly clamped on the edge. The effects of pressure gradient and gap errors are ignored. Furthermore, the Young's modulus and Poisson ratio are assumed to be constant and do not change with processing.

Small Deflection Theory

Assuming that $L_t \gg W_t$, T_t , the tethers can be modeled as a pair of clamped-clamped beams with a length of $2L_t$, subjected to a uniform distributed load Q (per unit length) and a central point load P [39], as shown in Figure 3-2. The distributed load is due to the shear stress acting on the tethers and is given as

$$Q = \tau_w W_t. \quad (3-1)$$

The point load, P , is the effect of the resultant shear force on the floating element and is given by

$$P = \tau_w W_e L_e / 2, \quad (3-2)$$

where the factor of 1/2 comes from the symmetry of the problem. The maximum deflection and bending stress distribution is obtained using Euler Bernoulli beam theory. The detailed derivation is given in Appendix A. The lateral displacement of the beam is given by

$$w(x) = \frac{-\tau_w}{4EW_t^3 T_t} \left[(3W_e L_e L_t + 8W_t L_t^2) x^2 - (2W_e L_e + 8W_t L_t) x^3 + 2W_t x^4 \right] \quad (0 \leq x \leq L_t), \quad (3-3)$$

where $E = 168 \text{ GPa}$ is the Young's modulus of silicon in the $\langle 110 \rangle$ direction [53]. The maximum deflection occurs at the center of the beam and is obtained by substituting $x = L_t$ into Equation (3-3) to get

$$\Delta = \frac{\tau_w W_e L_e}{4ET_t} \left[\frac{L_t}{W_t} \right]^3 \left[1 + 2 \frac{W_t L_t}{W_e L_e} \right]. \quad (3-4)$$

This corresponds to the floating element displacement. The second term in the brackets of Equation (3-4) is a correction for the distributed wall shear stress on the tethers. Equation (3-4) indicates that the important parameters affecting the scaling of the device are the area of the floating element, $W_e L_e$, ratio of the tether length to the tether width, L_t/W_t , and ratio of the area

of a tether to that of the floating element, $W_t L_t / W_e L_e$. If the tether surface area $W_t L_t \ll W_e L_e$, the stiffness is approximated as

$$\frac{1}{k} = \frac{\Delta}{\tau_w W_e L_e} = \frac{1}{4ET_t} \left[\frac{L_t}{W_t} \right]^3. \quad (3-5)$$

This indicates that the stiffness is proportional to the tether thickness and ratio of the tether width and length. The bending stress distribution through the width and length of the tether is given by

$$\sigma_t(x, y) = \frac{\tau_w W_e L_e L_t}{W_t^2 T_t} \left(1 - \frac{2y}{W_t} \right) \left[\left(\frac{3}{4} + \frac{2W_t L_t}{W_e L_e} \right) - \left(\frac{3}{2} + \frac{6W_t L_t}{W_e L_e} \right) \left(\frac{x}{L_t} \right) + \frac{3W_t L_t}{W_e L_e} \left(\frac{x}{L_t} \right)^2 \right] \begin{matrix} (0 \leq x \leq L_t) \\ (0 \leq y \leq W_t) \end{matrix}, \quad (3-6)$$

where $x = 0$ is at the end of the beam, and $y = 0$ is on the side wall surface. Equation (3-6) indicates that the maximum shear stress is located at the end of the beam and on the side wall surface ($x, y = 0$ in Figure 3-2).

Linear Euler-Bernoulli beam theory [54] fails for sufficiently large wall shear stresses because the mid-plane of the beam is strained [46]. The beam grows stiffer as the deflection becomes large. Furthermore, the nonlinear motion generates undesired harmonic distortion in the frequency domain. The sensor is required to maintain a linear relationship between shear stress and displacement in order to preserve spectral fidelity for time resolved measurement. This requirement places a nonlinear constraint in the sensor design optimization (discussed in Chapter 4). A large deflection mechanical model was therefore developed for use in determining this constraint.

Large Deflection Theory

Large deflection theory provides a measure of the maximum shear stress that may be measured while maintaining mechanical linearity. Two analysis techniques are pursued to

determine the nonlinear mechanical behavior of the sensor: the strain energy method [46] and an exact analytical method. The detailed derivations are given in Appendix A.

Energy method

The deflection predicted by the strain energy method [46] is obtained by assuming a trial function which meets both the clamped boundary condition and symmetry condition of the beam,

$$w(x) = \frac{\Delta_{NL}}{2} \left[1 + \cos\left(\frac{\pi(L_t - x)}{L_t}\right) \right] \quad (3-7)$$

where Δ_{NL} is the floating element deflection. The trial function is substituted into the expression for strain energy in the beam and the principle of minimum potential energy is applied. The result is

$$\Delta_{NL} \left[1 + \underbrace{\left(\frac{3}{4}\right)\left(\frac{\Delta_{NL}}{W_t}\right)^2}_{N-L \text{ term}} \right] = \frac{\tau_w W_e L_e}{4ET_t} \left[\frac{L_t}{W_t} \right]^3 \left[1 + 2 \frac{W_t L_t}{W_e L_e} \right]. \quad (3-8)$$

Comparing this result to Equation (3-4), one can see that cubic nonlinearity term has been added. The mechanical response of the floating element sensor will be linear provided that the nonlinear term is small with respect to unity; that is, if the displacement of the sensor is small in comparison to the tether width, $(\Delta_{NL}/W_t)^2 \ll 1$. The nonlinear term is cubic and therefore represents a Duffing spring behavior, or stiffening of the beam as deflections become large. This means that the nonlinear deflection is smaller than the ideal linear deflection for large shear stresses.

Exact analytical model

In the large deflection model, the neutral axis tension force F_a is taken into account. The average axial tension force is obtained by integrating the neutral axis strain along the length of

the beam. It then serves as a constitutive equation between axial force and strain. The detailed model development procedure is given in Appendix A. The maximum deflection predicted by the exact analytical method is obtained using von Kármán strain assumption,

$$\Delta_{AL} = -\frac{P}{2\lambda F_a} \sinh(\lambda L_t) - \frac{\cosh(\lambda L_t) - 1}{F_a \lambda \sinh(\lambda L_t)} \left(QL_t + \frac{P}{2} - \frac{P}{2} \cosh(\lambda L_t) \right) + \frac{QL_t^2}{2F_a} + \frac{PL_t}{2F_a}, \quad (3-9)$$

where the axial force F_a is given by

$$F_a = \frac{ET_t W_t}{2L_t} \int_0^{L_t} \left(\frac{dw(x)}{dx} \right)^2 dx, \quad (3-10)$$

and λ is given by

$$\lambda = \sqrt{12F_a / ET_t W_t^3}. \quad (3-11)$$

There are five variables, four boundary conditions and one constitutive equation. But the equation is indeterminate, so the final solution is obtained using an iterative technique to find λ , and therefore obtain the maximum deflection.

Lumped Element Modeling

Lumped element modeling is used to represent the fluidic to mechanical transduction of the shear stress sensor and facilitates the prediction of the dynamic response. The main assumption of LEM is that the length scale of the physical phenomena of interest is be much larger than the characteristic length scale of the device [55]. For the shear stress sensor, this means that the bending wavelength of the beam must be much larger than the length of the tethers. The LEM provides a simple way to estimate the dynamic response of a system for low frequencies, up to just beyond the first resonant frequency, which is appropriate for design purposes [56].

There are several types of elements in the lumped element model. For example, in a lumped mechanical system, mass represents the storage of kinetic energy, compliance of a spring (inverse of stiffness) represents the storage of potential energy, and a damper represents the loss of energy through dissipation. Similarly, in lumped electrical systems, generalized potential energy is stored in a capacitor, generalized kinetic energy is stored in an inductor, and energy is dissipated via a resistor.

From a LEM perspective, the two sets of tethers are modeled as a spring possessing an effective compliance C_{me} . In an impedance analogy, this compliance shares a common displacement with the effective mass M_{me} of the tethers and floating element as well as the damper, R_d , of the system. The main source of damping is the viscous damping underneath the element, and thermoelastic damping, compliant boundaries and vibration radiation to the structure boundaries are neglected in this research. Therefore, the sensor is modeled as a spring-mass-dashpot system, as schematically shown in Figure 3-3. In the equivalent circuit, the voltage and current are analogous to force and velocity, respectively. The motion of the mass-spring-dashpot system is described by the classic second-order differential equation,

$$F(t) = M_{me} \frac{d^2\Delta}{dt^2} + R_d \frac{d\Delta}{dt} + 1/C_{me} \Delta . \quad (3-12)$$

Therefore, the frequency response function of the device is found to be

$$H(j\omega) = \frac{\Delta(j\omega)}{F(j\omega)} = \frac{1}{(j\omega)^2 M_{me} + j\omega R_d + 1/C_{me}} , \quad (3-13)$$

where the angular frequency $\omega = 2\pi f$, f is the cyclic frequency, and $j = \sqrt{-1}$. Assuming a lightly damped system, the first resonant frequency f_r is

$$f_r = \frac{1}{2\pi\sqrt{C_{me}M_{me}}}. \quad (3-14)$$

The detailed derivation of the lumped elements is given in Appendix A. The effective mechanical compliance is determined by equating the potential energy stored in the beam to that of an equivalent lumped system and is

$$C_{me} = \frac{1}{2ET_t} \left(\frac{L_t}{W_t} \right)^3 \left(1 + 2 \frac{W_t L_t}{W_e L_e} \right)^2 \left/ \left(1 + 4 \frac{W_t L_t}{W_e L_e} + \frac{64}{15} \left(\frac{W_t L_t}{W_e L_e} \right)^2 \right) \right. . \quad (3-15)$$

The effective mass is obtained by equating the kinetic energy of the sensor to that of a lumped system and is

$$M_{me} = \rho_{si} W_e L_e T_t \left(1 + \frac{1494}{315} \frac{W_t L_t}{W_e L_e} + \frac{2238}{315} \left(\frac{W_t L_t}{W_e L_e} \right)^2 + \frac{1024}{315} \left(\frac{W_t L_t}{W_e L_e} \right)^3 \right) \left/ \left(1 + 2 \frac{W_t L_t}{W_e L_e} \right)^2 \right. , \quad (3-16)$$

where $\rho_{si} = 2331 \text{ kg/m}^3$ is the density of silicon [53].

Finite Element Analysis

To verify the analytical models, a finite element analysis with a clamped boundary condition on the edge of the tethers is performed. The material properties of silicon and the geometry of a representative structure are given in Table 3-1.

Finite element analysis is performed in CoventorWare[®] using the multi-mesh model by partitioning the continuum solid model into plate and tether volumes. A fine mesh is used in the tethers because of the large stress gradients with respect to those found in the plate. These volumes are joined to form one volume via *RigidLink* after meshing. The mesh is composed of parabolic *Manhattan brick* elements. A mesh refinement study revealed sufficient elements dimensions are $3 \mu\text{m}$, $0.5 \mu\text{m}$ and $1 \mu\text{m}$ in length, width and thickness within the tethers,

respectively, and 10 μm , 10 μm , 1 μm within the plate. Since the device is symmetric, only half of the structure is analyzed in the model, with 6600 elements in the analysis.

A representative displacement field of the tethers at $\tau_w = 5 \text{ Pa}$ is shown in Figure 3-4. The comparison in Figure 3-4 indicates that the nonlinear analytical model is in agreement with FEA simulation results. Figure 3-5 shows the maximum displacement of the floating element as a function of applied shear stress for analytical linear and nonlinear models, nonlinear energy method model and FEA model. This comparison in Figure 3-5 indicates that all results are in agreement in the linear range (50 Pa approximately), while the nonlinear analytical model, nonlinear energy method model and FEA models agree in this nonlinear deflection region. Figure 3-6 shows the stress distribution using analytical linear model (Equation (3-6)) and FEA results along the tether length on the sidewall surface ($y = 0$) for the representative structure. Figure 3-6 demonstrates that the analytical model is in agreement with the FEA model. The bending stress varies from tensile to compressive in a parabolic distribution along the tether length. Figure 3-6 shows that the maximum stress occurs on the edge zone ($x, y = 0$) of the tether.

The resonant frequency obtained from LEM (12.44 kHz) and FEA (12.47 kHz) agree well, as shown in Table 3-2. The next 5 modes were also found using FEA and are given in Table 3-3. The first six mode shapes are shown in Figure 3-7. The in-plane resonant frequency (second mode) is 17.08 kHz, greater than the out-of-plane resonant frequency (first mode) because the tether width is greater than the tether thickness for the verification studies (Table 3-1). Clearly, the representative dimensions used for model verification are not a preferred design, let alone an optimized design.

Piezoresistive Transduction

In 1954, Smith [52] discovered the piezoresistance effect in silicon and germanium. The piezoresistance effect is defined as the change of semiconductor resistivity due to a change in carrier mobility that results from an applied mechanical stress. In piezoresistive transduction, the resistance modulation is a function of the applied stress and piezoresistive coefficients (π_{ij}) [57].

For the cubic crystal structure of silicon under small strain, the correlation of normalized piezoresistivity ($\Delta\rho/\rho$) and stress for reduced tensor notation reduces to

$$\frac{1}{\rho} \begin{Bmatrix} \Delta\rho_1 \\ \Delta\rho_2 \\ \Delta\rho_3 \\ \Delta\rho_{23} \\ \Delta\rho_{13} \\ \Delta\rho_{12} \end{Bmatrix} = \begin{bmatrix} \pi_{11} & \pi_{12} & \pi_{12} & 0 & 0 & 0 \\ \pi_{12} & \pi_{11} & \pi_{12} & 0 & 0 & 0 \\ \pi_{12} & \pi_{12} & \pi_{11} & 0 & 0 & 0 \\ 0 & 0 & 0 & \pi_{44} & 0 & 0 \\ 0 & 0 & 0 & 0 & \pi_{44} & 0 \\ 0 & 0 & 0 & 0 & 0 & \pi_{44} \end{bmatrix} \begin{Bmatrix} \sigma_1 \\ \sigma_2 \\ \sigma_3 \\ \tau_{23} \\ \tau_{13} \\ \tau_{12} \end{Bmatrix}, \quad (3-17)$$

where $\Delta\rho$ is the change in resistivity, σ_i are normal stresses along the cubic crystal $\langle 100 \rangle$ axes, and τ_{ij} are shear stresses.

For a given resistor geometry, there are two piezoresistive coefficients used for piezoresistive sensing analysis in terms of stress orientation with respect to the current. The longitudinal piezoresistive coefficient captures the effect of an applied stress in the same direction as the current, and the transverse piezoresistance coefficient captures the effect of an applied stress in the direction perpendicular to the current. The longitudinal and transverse piezoresistive coefficients in terms of the fundamental piezoresistive coefficients and direction cosines are given by, respectively [58],

$$\pi_l = \pi_{11} + 2(\pi_{44} + \pi_{12} - \pi_{11})(l_1^2 m_1^2 + l_1^2 n_1^2 + m_1^2 n_1^2), \quad (3-18)$$

and

$$\pi_t = \pi_{12} - (\pi_{44} + \pi_{12} - \pi_{11})(l_1^2 l_2^2 + m_1^2 m_2^2 + n_1^2 n_2^2), \quad (3-19)$$

where (l_1, m_1, n_1) is the set of direction cosines between the longitudinal direction and the crystal axis, and (l_2, m_2, n_2) is the set of direction cosines between the transverse direction and the crystal axis. The direction cosines are given in terms of Euler's angles [59]

$$\begin{bmatrix} l_1 & m_1 & n_1 \\ l_2 & m_2 & n_2 \\ l_3 & m_3 & n_3 \end{bmatrix} = \begin{bmatrix} c\phi c\theta c\psi - s\phi s\psi & s\phi c\theta c\psi + c\phi s\psi & -s\theta c\psi \\ c\phi c\theta s\psi - s\phi c\psi & -s\phi c\theta s\psi + c\phi c\psi & -s\theta s\psi \\ c\phi s\theta & s\phi s\theta & c\theta \end{bmatrix}, \quad (3-20)$$

where $c\phi = \cos(\phi)$, $s\phi = \sin(\phi)$, and etc. The geometry of the Euler's angle is shown in Figure 3-8. In this research, a (100) wafer is used, thus $\theta = 0$, $\psi = 0$ and ϕ sweeps from 0 to 180 degree in Figure 3-8. Therefore, the matrix (3-20) reduces to,

$$\begin{bmatrix} l_1 & m_1 & n_1 \\ l_2 & m_2 & n_2 \\ l_3 & m_3 & n_3 \end{bmatrix} = \begin{bmatrix} c\phi & s\phi & 0 \\ -s\phi & c\phi & 0 \\ 0 & 0 & 1 \end{bmatrix}. \quad (3-21)$$

The piezoresistive coefficients, π_{11} , π_{12} and π_{44} are given in Table 3-4 for both p-type and n-type piezoresistors at room temperature for low doping concentrations.

For this piezoresistive device, the floating element sensor features integrated side-implanted diffused resistors [25, 50, 51] in the element tethers for piezoresistive detection. In this transduction scheme, the integrated force produced by the wall shear stress on the floating element causes the tethers to deform and thus creates a mechanical stress field in the tethers. The piezoresistors respond to the mechanical stress field with a change in resistance from its nominal unstressed value [46] as indicated by

$$\frac{\Delta R}{R} = \frac{\Delta \rho}{\rho} = \pi_l \sigma_l + \pi_t \sigma_t, \quad (3-22)$$

where ρ and R are the resistivity and resistance of the piezoresistor, respectively, Δ signifies the perturbation in the resistance and resistivity due to the piezoresistive effect, σ_l is the bending stress along the beam, and σ_t is the transverse stress. For a beam subjected to pure bending, Equation (3-22) simplifies to

$$\frac{\Delta R}{R} = \pi_l \sigma_l. \quad (3-23)$$

Piezoresistive Coefficients

The piezoresistive coefficients depend on crystal orientation, doping type and level, and temperature. This dependence is typically expressed as a product of the coefficient's low-doped room temperature value π_0 and a piezoresistive factor $P(N, T)$ [59]

$$\pi(N, T) = \pi_0 P(N, T), \quad (3-24)$$

where N is the doping concentration and T is the temperature. For a (100) wafer, the dependence of the piezoresistive coefficient on the crystal direction is given in Figure 3-9 and Figure 3-10 for p-type and n-type piezoresistors, respectively. This indicates that the maximum piezoresistive coefficient for p-type silicon is in the $\langle 110 \rangle$ direction, while for n-type silicon the maximum is in the $\langle 100 \rangle$ direction. Also note that n-type silicon has a larger achievable piezoresistive coefficient than p-type silicon. The longitudinal and transverse piezoresistive coefficients π_l and π_t in the $\langle 110 \rangle$ direction for n-type and p-type silicon are given in Table 3-5 [52]. As shown in Table 3-5, piezoresistors in p-type silicon are more sensitive than for n-type in the $\langle 110 \rangle$ direction, which is parallel or perpendicular to the flat of a (100) wafer. In this design, the p-type piezoresistors are chosen due to its high sensitivity in the $\langle 110 \rangle$ direction and

because of the lower temperature sensitivity at higher doping concentrations compared to n-type piezoresistors [60].

Many theoretical [59] and experimental [61-63] studies have reported the dependence of the piezoresistive factor $P(N,T)$ on doping concentration at room temperature. Kanda's model [59] is most popular and is accurate for low concentrations. However, when compared to experimental data [61-63], Kanda's model under predicts the roll-off of $P(N,T)$ for concentrations above 10^{17} cm^{-3} . For doping concentration above 10^{17} cm^{-3} , the fundamental piezoresistive coefficient is expressed as a product of its lightly-doped room temperature value π_0 and the experimentally fitted piezoresistive factor $P(N,T)$ [47],

$$\pi(N,T) = \pi_0 P(N,T) = \pi_0 \log\left(\frac{1.53 \times 10^{22} \text{ cm}^{-3}}{N}\right)^{0.2014}. \quad (3-25)$$

The piezoresistive factor is plotted in Figure 3-11 versus concentration at room temperature. The piezoresistive coefficient is also temperature dependent. At higher doping concentrations, there will be a reduction in both thermal noise and $1/f$ noise compared to lower doping concentrations [47]. In addition, the temperature dependence of the piezoresistance coefficient is reduced significantly as the concentration increases at low doping concentration. For doping concentrations above 10^{20} cm^{-3} , the piezoresistance coefficient is almost independent of temperature variation [61]. However, the sensitivity degrades due to the reduced piezoresistive coefficient at a high doping level [62]. Thus, there is a tradeoff between sensitivity and noise floor. This tradeoff suggests optimization is necessary to obtain the best performance, as will be discussed in chapter 4.

Piezoresistive Sensitivity

For the structure shown in Figure 3-12, the side-implanted piezoresistors are fabricated by first implanting p-type impurities (boron) into the sidewall, followed by a diffusion step to drive-in and to electronically activate the impurities. The impurities diffuse laterally, and the resulting impurity concentration profile decreases from the surface of the side wall to the junction depth. If the unstrained impurity profile as a function of depth, $N(y)$, is known, the piezoresistive coefficient profile $\pi(y)$ can be determined. As shown in Equation (3-6), the stress varies along the beam, and varies across the junction depth, y_j , as well. Therefore, the product of the stress and the piezoresistive coefficient distributions need to be integrated in the electromechanical model.

Several models have been developed for piezoresistive sensitivity. Tortonese [64] and Harley [65] built a two-step model for non-uniform doping concentration and formulated an efficiency factor β to be inserted into the numerator of the surface sensitivity equation. In integrating across the beam, their model does not account for the junction isolation of diffused resistors. Senturia [46] presents the piezoresistive coefficient dependence of the doping concentration, but does not account for stress variation as a function of depth. Sze's model [57] addresses stress variations across the resistors (y -direction) and incorporates a conductance-weighted piezoresistance coefficient. Sze, however, did not account for the stress variation along the piezoresistor (x -direction). Based on Harley's work, a new model was developed by involving stress averaging along the tether length and across the depth of piezoresistor, and using a conductance-weighted piezoresistive coefficient.

Two issues need to be considered in calculating the piezoresistive response. One is that the piezoresistors are typically formed by diffusion, thus have a non-uniform doping profile with

respect to junction depth. The second issue is that piezoresistors also span a finite area on the device, and hence have non-uniform stress with respect to length and depth. The derivation of the resistance of the piezoresistor begins with the non-uniform doping concentration that varies from the sidewall surface to the junction depth (y -direction). The stress varies in this direction as well. As shown in Figure 3-12, the resistor can be considered as a stack of slices, where each slice has a slightly different doping concentration and stress. The current flow is in x direction, so the slices (dy) are connected electrically in parallel because they share the same potential. The stress also varies along the length of the resistor (x - direction). Thus, the resistor is also segmented along its length. These segments (dx) are connected in series due to the same current flow. The mechanical model assumes that $L_t \gg W_t$ and T_t , thus the differential resistance of a unit cell for a small segment dx and a small slice dy with width of W_r is given by

$$dR_{unit}(x, y) = \frac{1}{dG_{unit}(x, y)} = \frac{\rho_e(x, y) dx}{W_r dy}, \quad (3-26)$$

where it is assumed that $y = 0$ at the surface and $y = W_t/2$ at the neutral axis. In Equation (3-26), $\rho_e(x, y)$ is the stressed resistivity determined by [46]

$$\rho_e(x, y) = \rho_{eo}(y)(1 + \pi_l(y)\sigma_l(x, y)), \quad (3-27)$$

where $\rho_{eo}(y)$ is the unstressed resistivity and $\sigma_l(x, y)$ is given in Equation (3-6). For non-uniform doping, $\rho_{eo}(y)$ is given by [66]

$$\rho_{eo}(y) = \frac{1}{\mu_p(y)qN_A(y)}, \quad (3-28)$$

where $q = 1.602 \times 10^{-19}$ C is the electronic charge of an electron and $\mu_p(y)$ is the boron mobility. In this research, the mobility is obtained from [67]. To simplify the calculation process,

we use conductance $G = 1/R$ rather than resistance in the derivation. The total conductance for segment dx is obtained by summing the conductance of each unit

$$dG_{slice} = \sum_0^{y_j} dG_{unit} = \frac{1}{dx} \int_0^{y_j} \frac{W_r dy}{\rho_{eo}(y)(1 + \pi_l(y)\sigma_l(x, y))}. \quad (3-29)$$

The total resistance is determined by summing the resistance of the small dx segments,

$$R + \Delta R = \int_{L_R}^{L_R+L_r} 1/dG_{slice} = \int_{L_R}^{L_R+L_r} \frac{1}{\int_0^{y_j} \frac{W_r dy}{\rho_{eo}(y)(1 + \pi_l(y)\sigma_l(x, y))}} dx, \quad (3-30)$$

where $L_R = 10 \mu\text{m}$ is the overlap end cap and it does not change the resistance value. The total unstressed resistance is similarly found by integrating along the length of the resistor using the unstressed resistivity,

$$R = \sum_{L_R}^{L_R+L_r} 1/dG_{slice} = \int_{L_R}^{L_R+L_r} \frac{1}{\int_0^{y_j} \frac{W_r dy}{\rho_{eo}(y)}} dx. \quad (3-31)$$

Then the resistance modulation is obtained by arranging Equation (3-30) and (3-31),

$$\frac{\Delta R}{R} = \frac{R + \Delta R - R}{R} = \frac{\int_0^{y_j} \frac{dy}{\rho_{eo}(y)}}{L_r} \int_{L_R}^{L_R+L_r} \frac{1}{\int_0^{y_j} \frac{dy}{\rho_{eo}(y)(1 + \pi_l(y)\sigma_l(x, y))}} dx - 1. \quad (3-32)$$

Electromechanical Sensitivity

The four side-wall implanted piezoresistors form a full Wheatstone bridge circuit that provides sensitivity enhancement for a small change in resistance. As illustrated in Figure 3-13, when the tether deflects in the y direction, piezoresistors 1 and 3 experience a compressive stress while 2 and 4 experience a tensile stress. These resistors experience a change in resistance

of $-\Delta R$ and ΔR , respectively. For an ideal bridge, $R_1 = R_3 = R - \Delta R$ and $R_2 = R_4 = R + \Delta R$, so that the output voltage, V_o , for a given bias voltage V_B , is

$$V_o = \left(\frac{R_4}{R_3 + R_4} - \frac{R_1}{R_1 + R_2} \right) V_B = \frac{\Delta R}{R} V_B. \quad (3-33)$$

The sensitivity of the piezoresistive sensor is defined as the change of output voltage per unit of applied shear stress and for a linear sensor is expressed as

$$S_{EM} = \frac{\partial V_o}{\partial \tau_w} = \frac{V_o}{\tau_w}. \quad (3-34)$$

Substituting in Equation (3-33), the electromechanical sensitivity is rewritten as

$$S_{EM} = \frac{\Delta R}{R} \frac{V_B}{\tau_w}. \quad (3-35)$$

Noise Model

The key sources of the electrical noise in piezoresistive sensors are thermal noise, low frequency $1/f$ noise, and amplifier noise [65]. Physical fluctuations of the floating element at an equilibrium temperature, T , can result in random motion of the device; however, the contribution of thermomechanical displacement noise has been found to be much smaller than the electronic noise sources except at mechanical resonance [47]. For an ideally balanced Wheatstone bridge, the bias source noise will be common mode rejected.

Thermal Noise

Thermal noise, also known as “Nyquist” or “Johnson noise”, is produced when electrons are scattered by thermal vibration of the lattice structure [68]. Since higher temperatures lead to increased vibrational motion, thermal noise power spectral density (PSD) is directly proportional to temperature. Moreover, thermal noise is present in thermodynamic equilibrium, and its PSD is independent of frequency since random thermal vibrations are not characterized by discrete

time constants. The thermal noise PSD (S_{vT}) is modeled by Nyquist [68], which was experimentally verified by Johnson [69], as

$$S_{vT} = 4k_B TR, \quad (3-36)$$

where $k_B = 1.38 \times 10^{-23} \text{ J/K}$ is the Boltzmann constant, R is the total resistance in the resistor, and T is the temperature in Kelvin. In a piezoresistor, the rms noise voltage, V_{iR} , due to thermal noise is obtained by taking the square root of the thermal noise PSD integrated over the bin width of interest $\Delta f = f_2 - f_1$ [68],

$$V_{iR} = \sqrt{\int_{f_1}^{f_2} S_{vT} df} = \sqrt{4k_B TR \Delta f}, \quad (3-37)$$

1/f Noise

The dominant noise source for most ion-implanted piezoresistors is 1/f noise. Hooge [70] first reported that the 1/f noise PSD of a piezoresistor is inversely proportional to the total number of carriers in the resistor when an external dc bias voltage is applied, and is given by

$$S_{v1/f} = \frac{\alpha_H V_R^2}{N_c f}, \quad (3-38)$$

where V_R is the voltage across the resistor, N_c is the total number of ionized carriers in the resistor, f is frequency, and α_H is Hooge parameter, with the experimental values ranging from 5×10^{-6} to 2×10^{-3} [71]. Hooge's parameter is sensitive to bulk crystalline silicon imperfections and the interface quality. Low frequency noise occurs under non-equilibrium conditions and its spectra is proportional to the square of the applied voltage. Two physical mechanisms have been proposed to account for the low frequency noise: random trapping/detrapping of carriers at the

surface and bulk electronic traps, and random mobility fluctuations [72]. The noise power of $1/f$ noise is obtained by integrating Equation (3-38) over a frequency range of operation

$$V_{1/fR} = \sqrt{\frac{\alpha_H V_R^2}{N_c} \ln\left(\frac{f_2}{f_1}\right)}. \quad (3-39)$$

The total number of ionized carriers in the resistors for the piezoresistor geometry in Figure 3-12 is given as

$$N_c = L_r W_r \int_0^{y_j} N_A(y) dy, \quad (3-40)$$

where $N_A(y)$ is the p -type doping concentration. As indicated in Equation (3-39), $1/f$ noise increases for small volumes and highly resistive piezoresistors.

In this dissertation, the typical input noise of a low noise amplifier at 1kHz, 4 nV/ $\sqrt{\text{Hz}}$ [73], is used in the noise floor model. For an ideally balanced Wheatstone bridge assuming a unity gain amplifier, the total rms output noise voltage V_N is

$$V_N = \sqrt{\frac{1}{4} \frac{\alpha_H V_B^2}{N_c} \ln\left(\frac{f_2}{f_1}\right) + 4k_B TR \Delta f + (4e-9)^2 \Delta f}, \quad (3-41)$$

where the first, second and third terms in Equation (3-41) are the contribution of $1/f$ noise, thermal noise, and the amplifier noise, respectively. The detailed derivation of Equation (3-41) is given in Appendix B. Since narrow bin turbulence spectra are desired, a figure of merit bin width of $\Delta f = 1$ Hz centered at 1 kHz is used in this dissertation; therefore, $f_1 = 999.5$ Hz and $f_2 = 1000.5$ Hz.

The minimum detectable shear stress (MDS) or input noise, τ_{\min} , is the minimum shear stress that the shear stress sensor can resolve in the presence of noise, and is defined as

$$\tau_{\min} = \frac{V_N}{S_{EM}}. \quad (3-42)$$

The dynamic range (DR) is then given by

$$DR = 20 \log \left(\frac{\tau_{\max}}{\tau_{\min}} \right). \quad (3-43)$$

Device Specific Issues

In this section, a few specific design issues are addressed, including transverse sensitivity, acceleration sensitivity, pressure sensitivity, temperature compensation and device junction isolation issues.

Transverse Sensitivity

Transverse sensitivity was discussed in Chapter 2 (Equation (2-16)), and restated here briefly. Recall that the transverse mechanical sensitivity in the x -direction can be neglected due to the large differences in bending versus axial stiffness, while transverse mechanical sensitivity in the z direction is of the same order as in the flow direction. The x -direction also possesses electromechanical rejection for an ideally balanced bridge.

Assuming the flow is in the y direction, when the sensor is subjected to an x -axis acceleration, piezoresistors 1 and 2 experience a tensile stress while 3 and 4 experience a compressive stress. These resistors experience a change in resistance of ΔR (piezoresistors 1 and 2 and $-\Delta R$ (piezoresistors 3 and 4), respectively (Figure 3-14 (a)). The resistances in the bridge become $R_1 = R_2 = R + \Delta R$, $R_3 = R_4 = R - \Delta R$. The output voltage, V_o , for a given bias voltage V_B , is given by

$$V_o = \frac{R_1}{R_1 + R_2} - \frac{R_3}{R_3 + R_4} = \frac{R + \Delta R}{2R + 2\Delta R} - \frac{R - \Delta R}{2R - 2\Delta R} = 0. \quad (3-44)$$

When the fluctuating pressure load acts in the z direction, the stress distribution in all four tethers is the same, leading to equal resistance perturbations (ΔR) in all four piezoresistors. The reaction of the Wheatstone bridge due to pressure is shown in Figure 3-14 (b). The total pressure effect is to supply a common mode signal into this differential sensing scheme, which does not affect the voltage output. Therefore, the ideal electromechanical sensitivity due to the x-axis load and pressure disturbance is ideally equal to zero. In reality, there will still be transverse sensitivity due to bridge mismatch.

Temperature Compensation

The output voltage of a piezoresistive sensor is dependent on temperature due to the thermal sensitivity of the resistance, strain and piezoresistive coefficient [46]. In this dissertation, it is assumed that the thermal coefficient of resistance will dominate over thermal strain effects and changes in the piezoresistive coefficient. The typical temperature coefficient of resistance for a laterally implanted sensor is reported to be $0.0081 \text{ k}\Omega/^{\circ}\text{C}$, which is much larger than the shear stress sensitivity [25]. Since it is impossible in practice to have absolute temperature control in a wind tunnel, temperature compensation of the output signal must be employed. It is important that the temperature is measured as close as possible to the sensing element to avoid compensation errors due to temperature gradients in the flow. In this thesis, the temperature compensation of the resistors are achieved using a double bridge configuration [74]. As shown in Figure 3-15, two Wheatstone bridges are used on one chip; one is the active Wheatstone bridge with output that is a function of shear stress and temperature, while the other is a dummy compensation Wheatstone bridge with output that acts as a thermometer and only depends on temperature. The dimension of the compensation bridge resistors is identical to the active bridge and is kept as close as possible to the active bridge (safe distance of $100 \mu\text{m}$

suggested for the peripheral circuits [75]). The detailed temperature compensation procedure for the non-ideal case of a statically unbalanced bridge is discussed in Chapter 6.

For ideally balanced Wheatstone bridge, the power supply noise is just a common mode signal to the bridge and would not affect the bridge voltage output. In most physically realized devices, the bridge is not exactly balanced. Therefore, the power supply noise contribution to the noise scales with the bridge offset voltage output normalized by the bias voltage.

Device Junction Isolation

One design issue is the difficulty of realizing a junction-isolated, laterally diffused resistor in the sidewall of a tether. As shown in Figure 3-16, the p-type piezoresistor (with resistance R_s), the p⁺⁺ interconnects (with resistance R_L) and the n-type substrate form a p/n diode. For an ideal p/n diode, the leakage current is negligible in the reverse bias region [76]. When the reverse voltage exceeds a certain value, the reverse current will increase rapidly and the diode will breakdown. To ensure the current flows exclusively through the p-type regions, the p/n junction must be reverse-biased for all possible bias voltages along the entire length of the piezoresistor and interconnect. This section addressed design issues associated with this design constraint.

Two issues must be taken into account in the design: (1) maintaining junction isolation and (2) avoiding p/n junction breakdown while achieving the desired piezoresistor sensitivity. When a voltage is applied between the two p⁺⁺ interconnects, the p/n junction voltage varies linearly with position due to a linear voltage drop across a distributed resistance. For junction isolation, the p/n junction must be reverse-biased at all spatial locations.

Under reverse bias, a p/n junction develops a space charge layer due to the depletion of carriers [76]. In order to maintain electrical isolation, it is necessary to ensure that the space

charge layers for adjacent p-type regions extending into the n-type substrate do not overlap or ‘punch-through’. The space charge layers punch-through will cause the corresponding p regions to become shorted, resulting in a non-functional device. Assuming uniform doping, the acceptor concentration in the p region is assumed to be N_A , and the donor concentration in the n region is assumed to be N_D . The space charge layer widths on the p-side (x_p) and n-side (x_n) are given as a function of the junction voltage V_j [76],

$$x_p(V_j) = \sqrt{\frac{2\epsilon_{Si}}{q} \frac{N_D}{N_A(N_A + N_D)} (V_{bi} - V_j)}, \quad (3-45)$$

and

$$x_n(V_j) = \sqrt{\frac{2\epsilon_{Si}}{q} \frac{N_A}{N_D(N_A + N_D)} (V_{bi} - V_j)}, \quad (3-46)$$

where $\epsilon_{Si} = 1.045 \times 10^{-12}$ F/cm is the silicon permittivity, and the intrinsic number of electrons is $n_i = 10^{10}$ /cm³ in silicon at room temperature. The built-in voltage is given as

$$V_{bi} = \frac{kT}{q} \ln \left(\frac{N_A N_D}{n_i^2} \right) \quad (3-47)$$

In order to electrically isolate the p⁺⁺ regions, the entire length of the p/n junction must be reverse-biased ($V_j < 0$). The space charge layer width in the p and n region, x_p and x_n , respectively, increases with reverse bias. The total space charge width on the n side is given by

$$W(V_j) = x_n(V_j) + x_n(-(V_B + V_j)). \quad (3-48)$$

If the total space charge layer width on the n side, $W(V_j)$, increases to the width between the piezoresistor and the p⁺⁺ interconnect, L_1 , or to the width between the p⁺⁺ interconnects, L_2 , the space charge layers will punch-through, causing the corresponding p regions to be shorted.

To avoid punch-through, $W(V_j) \ll L_1$ must be satisfied for all junction voltages, V_j . Additionally, lateral diffusion that occurs during high temperature process steps, leading to an increase in the actual width of the p-type region compared to the designed width, must be taken into account. Therefore, the total isolation width is approximated by

$$W_{iso}(V_j) = 2L_d + x_n(V_j) + x_n(-(V_B + V_j)), \quad (3-49)$$

where L_d is the lateral diffusion width estimated from the net effect of high temperature process time on the diffusion length (thermal budget) [77]. The total thermal budget $(Dt)_{tot}$ is equal to the sum of the diffusion \times time, Dt , products for all high temperature cycles affecting the lateral diffusion, $(Dt)_{tot} = \sum D_i t_i$, where D_i and t_i are the diffusion coefficient and time associated with each processing step.

In this design, the doping profile is non-uniform, and the acceptor concentration in the p region $N_A(y)$ and the donor concentration in the n region $N_D(y)$ vary with depth, as shown in Figure 3-17. The non-uniform doping profiles are obtained by FLOOPS[®] simulation [78], where sidewall boron implantation in amorphosized silicon is simulated by SRIM [79] and then imported to FLOOPS[®]. The cross-sectional view of the isolation width for a doping profile at a bias voltage of 10 V is shown in Figure 3-18 and Figure 3-19, which are associated with the A-A and B-B cuts shown in Figure 3-20. The dimensions of the tether width W_t , the sidewall implanted piezoresistor depth L_4 , the p⁺⁺ interconnect width L_3 , and the space parameters, L_1 , L_2 and L_5 are listed in Table 3-6 for the actual device.

There is a tradeoff between the p⁺⁺ interconnect widths, L_3 and L_4 , and the punch-through width L_1 . A large value of L_3 and L_4 is desired to reduce the lead resistance. The

resulting narrow gap, L_1 , may cause p/n junction punch-through. On the edge of the tethers, the p⁺⁺ interconnects are tilted 24 degrees from the tether centerline to increase the isolation gap spacing. For the worst case, $V_j = -10$ V at left and 0 V on the right, as shown in Figure 3-20, there is about 9 μm between adjacent p⁺⁺ interconnects assuming a lateral diffusion of ~ 1.1 μm . Meanwhile, a crossover between the piezoresistor and p⁺⁺ interconnects must be avoided. As shown in Figure 3-19, the space charge layer of the piezoresistor in the n-well increases as the depth increases. If the space between the piezoresistor and the p⁺⁺ interconnect is too close, there will be crossover and the p-region will punch through. A top view of the isolation width is shown in Figure 3-20. The blue region is the tether, the cyan region is the p⁺⁺ interconnects, the green region is the piezoresistor, and the pink line is the final isolation width considering lateral diffusion and space charge diffusion to the n-well at $V_j = -10$ V (worst case).

In order to minimize the space charge width in the n-well, one can increase the doping concentration of the n-well, N_D . There is, however, a tradeoff between increased n-well doping concentration and reduced reverse breakdown voltage. With increasing doping, the internal electric field increases and the reverse junction breakdown voltage decreases [80, 81]. The breakdown voltage decreases from ~ 50 V to ~ 10 V when the impurity concentration increases from $1.0 \times 10^{16} \text{ cm}^{-3}$ to $1.0 \times 10^{17} \text{ cm}^{-3}$.

The curvature of the tether corner and the curvature of the junction regions must also be considered. A sharp corner dramatically increases the mechanical stress, which could lead to possible failure of the materials [82]. Additionally, a sharp corner in the p/n junction may increase the local electric field and decrease the breakdown voltage [83]. Thus, the corner is rounded. The stress concentration factor, K , depends on the fillet radius for a given thickness [82] and is relatively high when the ratio of the fillet radius and tether width is less than 0.5. In

this design, K is chosen as 0.9. In addition, 4 slots in the substrate near the edge of each tether are designed to relieve stress concentrations that arise during fabrication [51].

In order to avoid these issues, a metal contact design is employed, where the metal lines run on the top of the tethers to connect either side of the laterally implanted piezoresistors, as shown in Figure 3-21. Because there are two 50 μm deep trenches on both sides of the tether for tether release, the fabrication process of this design is very challenging and is discussed in detail in Chapter 5.

Summary

Electromechanical modeling of a side-implanted piezoresistive floating element shear stress sensor has been developed for aerospace applications. Two Wheatstone bridges are employed, an active bridge for shear stress sensing and a dummy bridge for temperature compensation. The predicted sensitivity, noise floor, dynamic range and MDS have been modeled and verified by FEA.

To accurately resolve the fluctuating shear stress in a turbulent boundary layer, the shear stress sensor is desired to possess a small size, large usable bandwidth and a low MDS. MDS depends on the geometry of sensors and piezoresistors, dopant profile, process parameters, and sensor excitation. To achieve a low MDS, it is favorable to maximize sensitivity and minimize noise. However, there are tradeoffs between sensitivity and noise floor. It is necessary to perform design optimization to balance these conflicting requirements. Additionally, the sensor design is constrained by temporal and spatial resolution requirements as well as structural limits. The detailed optimization is discussed in Chapter 4.

Table 3-1. Material properties [53] and geometry parameters used for model validation.

Density of silicon ρ_{Si} (kg/m ³)	2330
Young's modulus in [110] orientation E (GPa)	168
Poisson ratio ν_p	0.27
Length of tethers L_t (μm)	400
Thickness of the tethers T_t (μm)	3
Width of the tethers W_t (μm)	4
Length of the square floating element L_e (μm)	150

Table 3-2. Resonant frequency and effective mass predicted by LEM and FEA for the representative structure given in Table 3-1.

	Frequency (kHz)	Effective Mass (kg)
LEM	12.44	1.66e-10
FEA	12.47	1.72e-10

Table 3-3. First 6 modes and effective mass predicted by FEA for the representative structure given in Table 3-1.

Mode Domain	Frequency (kHz)	Effective Mass (kg)
1	12.47 (translational in z -direction)	1.72e-10
2	17.08 (translational in y -direction)	1.74e-10
3	34.95 (rocking mode about x -axis)	6.82e-10
4	162.33 (rocking mode about y -axis)	1.81e-11
5	170.11 (rocking mode about z -axis)	1.84e-11
6	219.50 (translational in x -direction)	1.70e-11

Table 3-4. Piezoresistive coefficients for n-type and p-type silicon [53].

	π_{11} (10^{-11}Pa^{-1})	π_{12} (10^{-11}Pa^{-1})	π_{44} (10^{-11}Pa^{-1})
n-type	-102.2	53.4	-13.6
p-type	6.6	-1.1	138.1

Table 3-5. Piezoresistive coefficients for n-type and p-type silicon in the <110> direction [53].

	$\pi_l (*10^{-11}\text{Pa}^{-1})$	$\pi_t (*10^{-11}\text{Pa}^{-1})$
n-type	-31.2	-17.6
p-type	71.8	-66.3

Table 3-6. Space parameter dimensions for junction isolation.

W_t	L_t	L_2	L_3	L_4	L_5
30 μm	9 μm	13.6 μm	15 μm	1 μm	33 μm

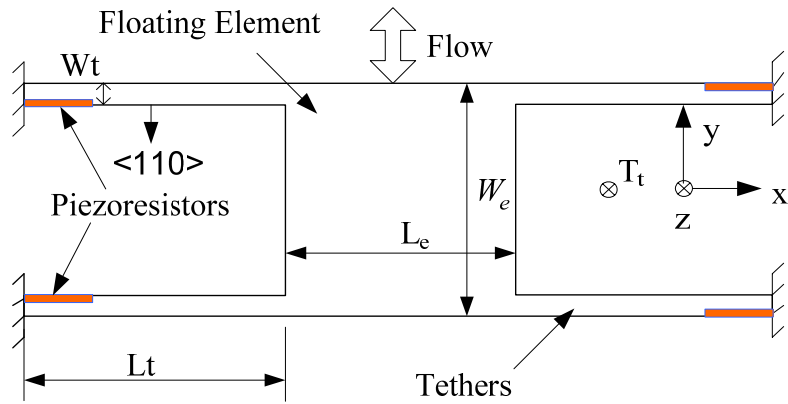


Figure 3-1. Schematic top view of the structure of a piezoresistive floating element sensor.

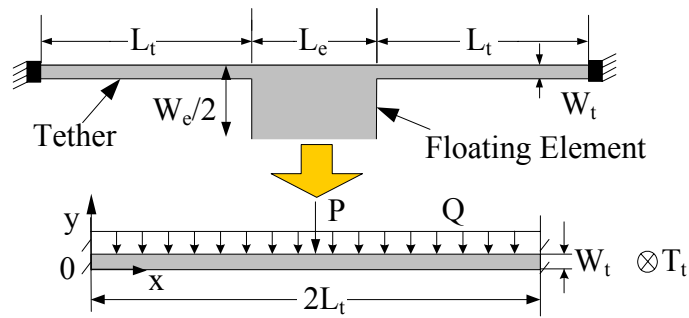


Figure 3-2. The simplified clamped-clamped beam model of the floating element structure.

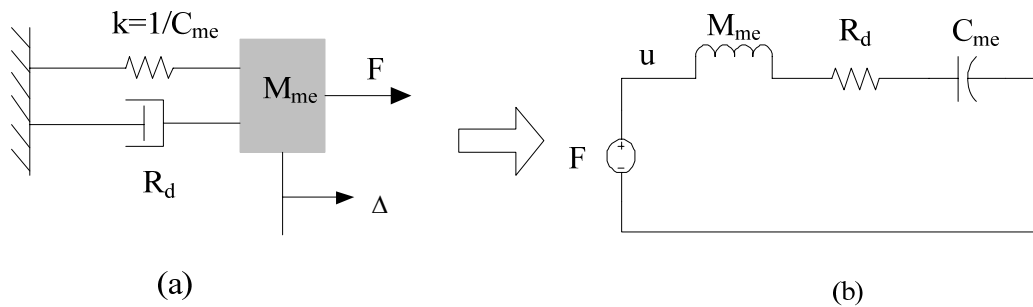


Figure 3-3. Lumped element model of a floating element sensor: (a) spring-mass-dashpot system (mechanical) and (b) equivalent electrical LCR circuit.

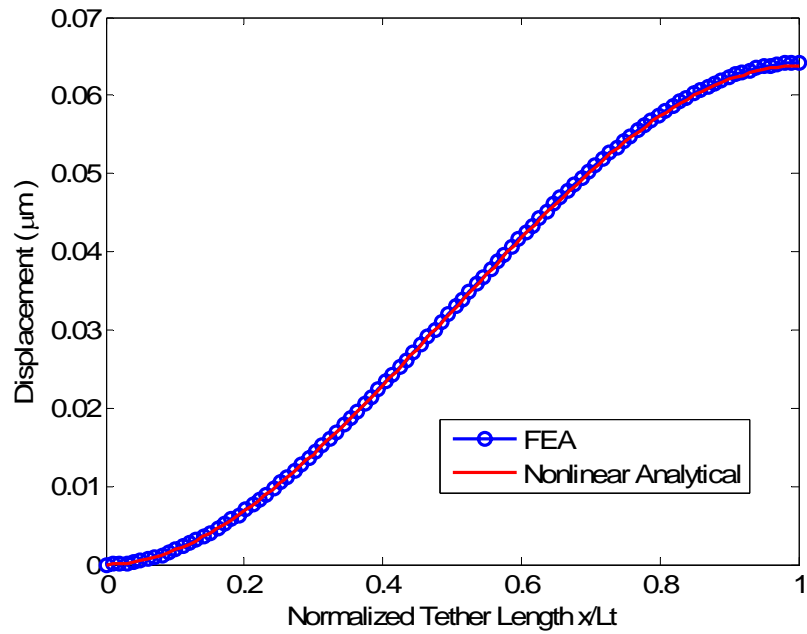


Figure 3-4. Representative results of displacement of tethers for the representative structure given in Table 3-1 at $\tau_w = 5 \text{ Pa}$.

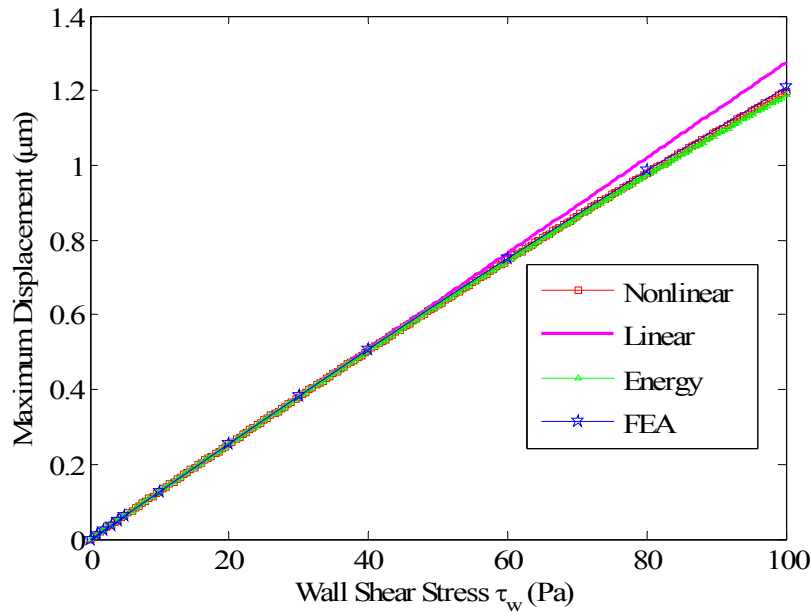


Figure 3-5. Representative load-deflection characteristics of analytical models and FEA for the representative structure given in Table 3-1 and $\tau_w = 5 \text{ Pa}$.

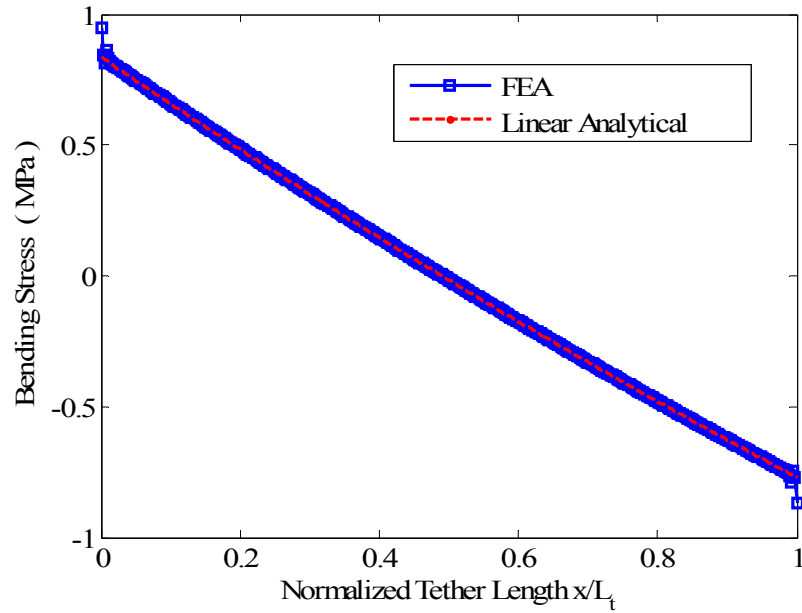


Figure 3-6. Verification of the analytically predicted stress profile (Equation (3-6)) with FEA results for the representative structure of Table 3-1 and $\tau_w = 5 \text{ Pa}$.

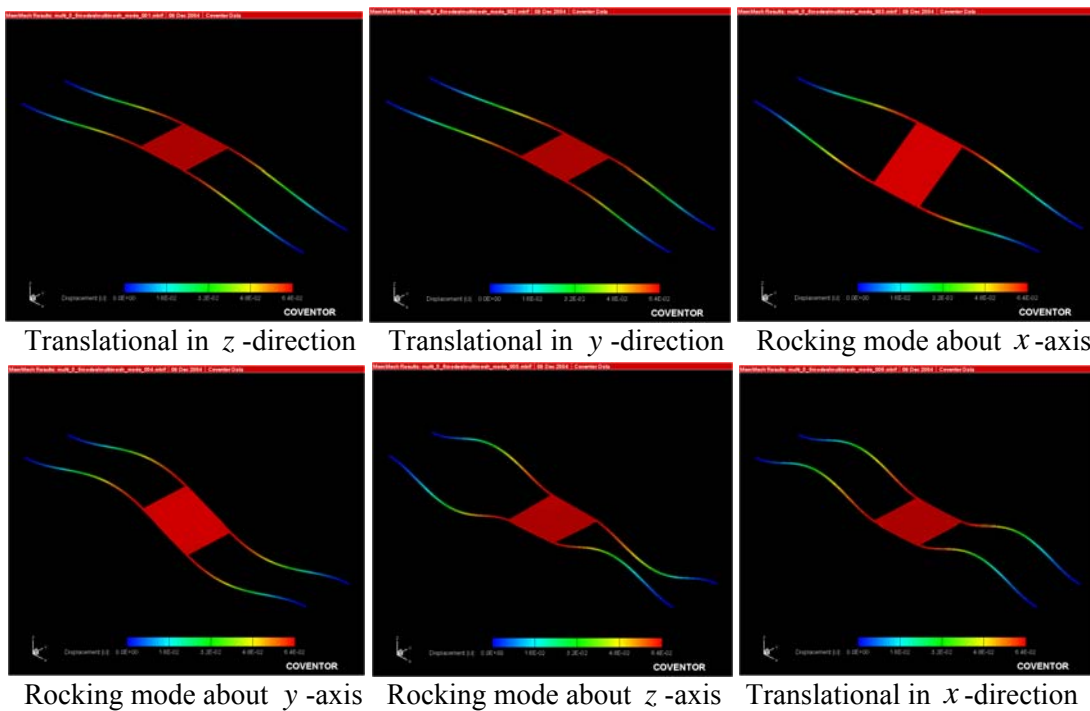


Figure 3-7. The mode shape for the representative structure of Table 3-1 and $\tau_w = 5 \text{ Pa}$.

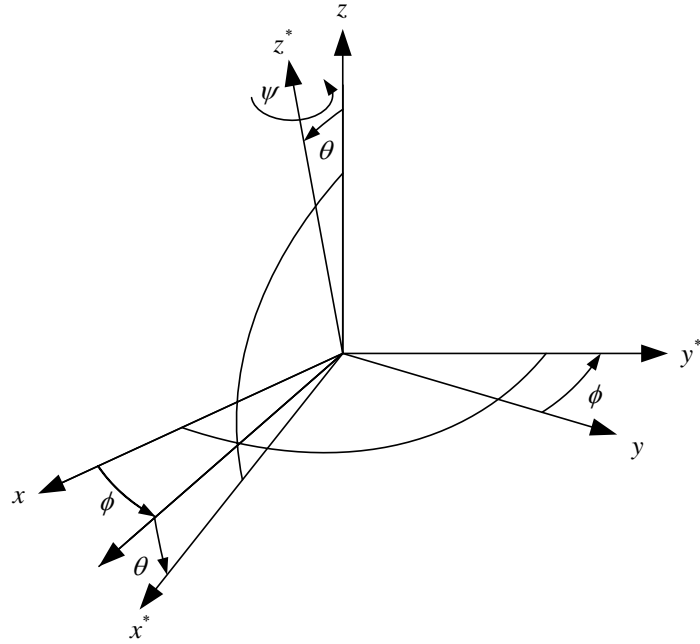


Figure 3-8. Geometry used in computation of Euler's angles [59].

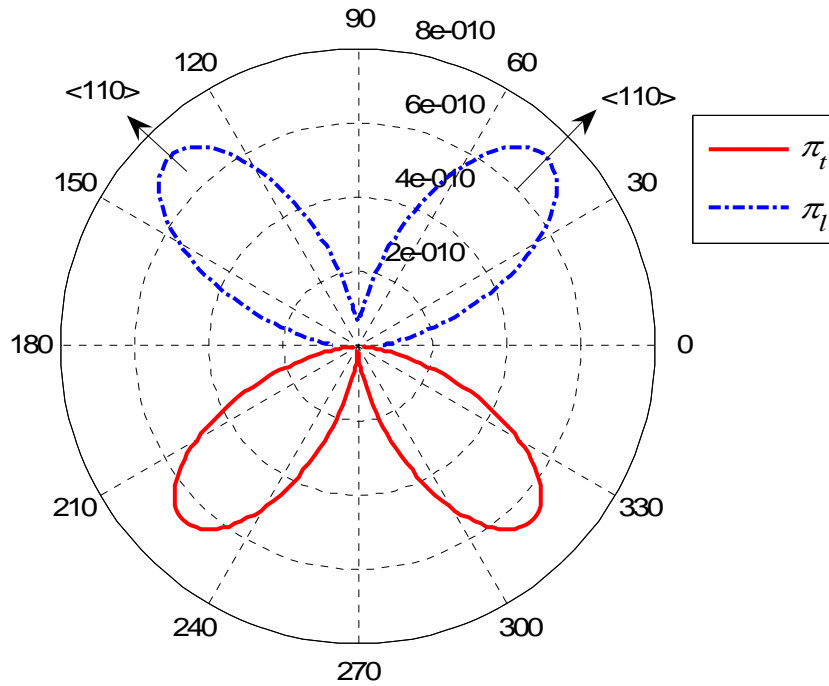


Figure 3-9. Polar dependence of piezoresistive coefficients for p-type silicon in the (100) plane.

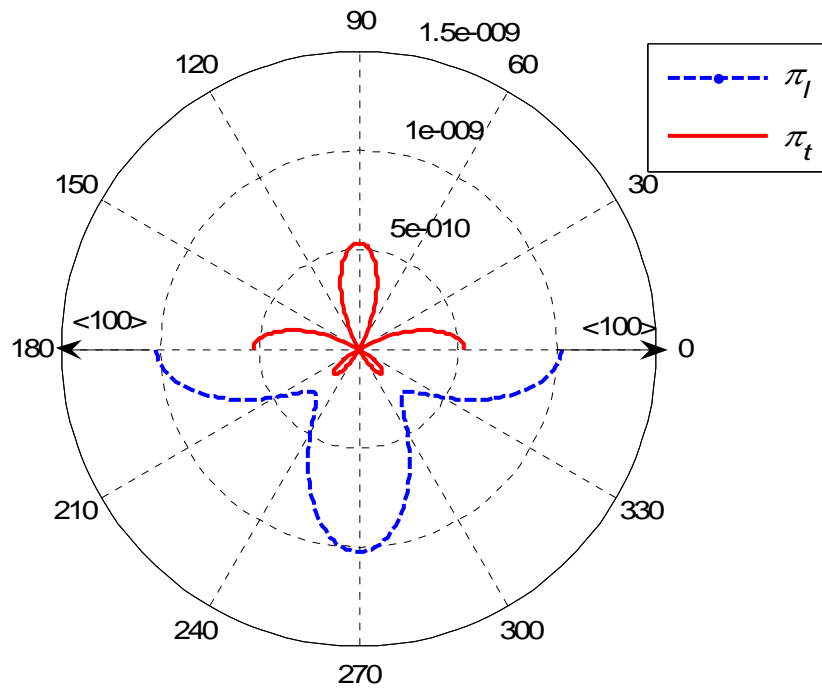


Figure 3-10. Polar dependence of piezoresistive coefficients for n-type silicon in the (100) plane.

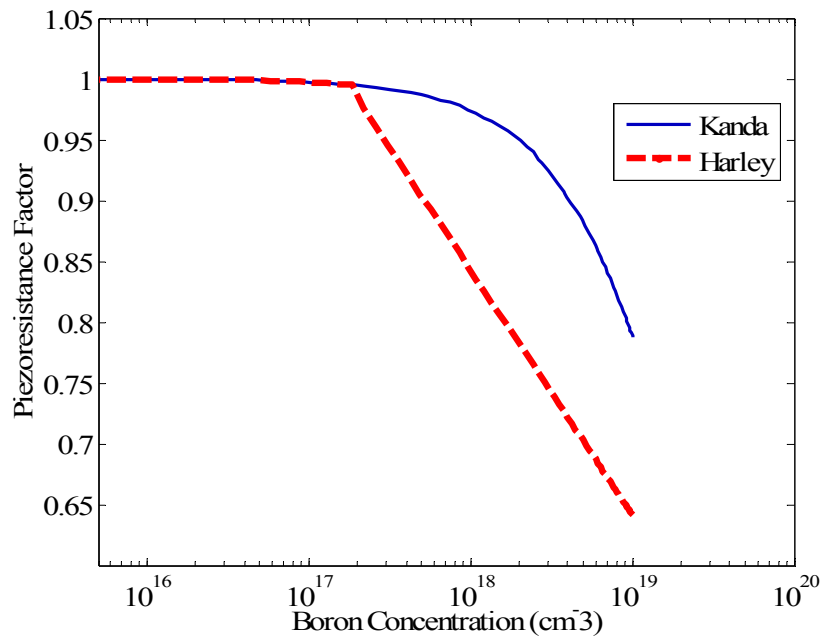


Figure 3-11. Piezoresistive factor as a function of impurity concentration for p-type silicon at 300K [47].

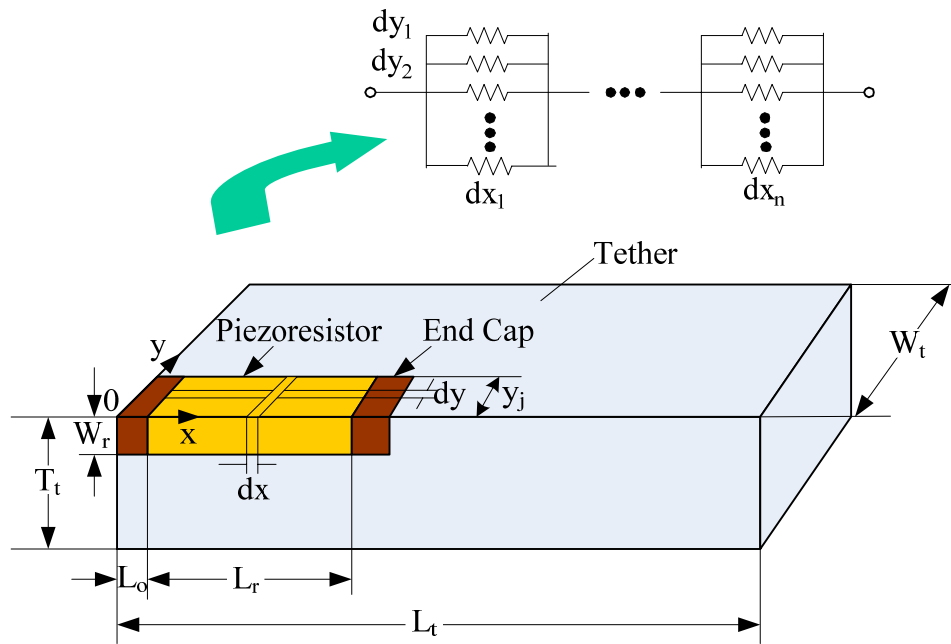


Figure 3-12. Schematic illustrating the relevant geometric parameters for piezoresistor sensitivity calculations.

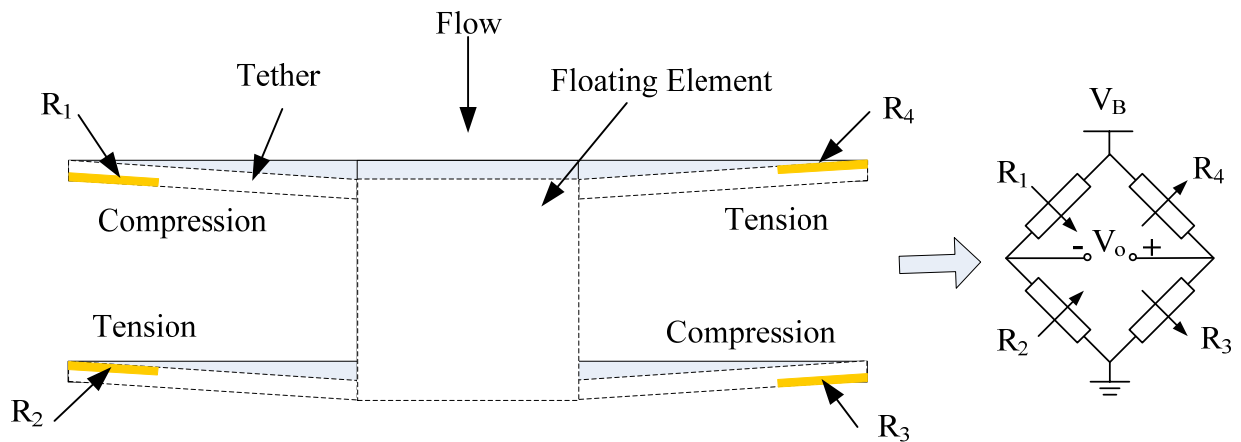


Figure 3-13. Schematic representative of a deflected side-implanted piezoresistive shear stress sensor and corresponding resistance changes in Wheatstone bridge.

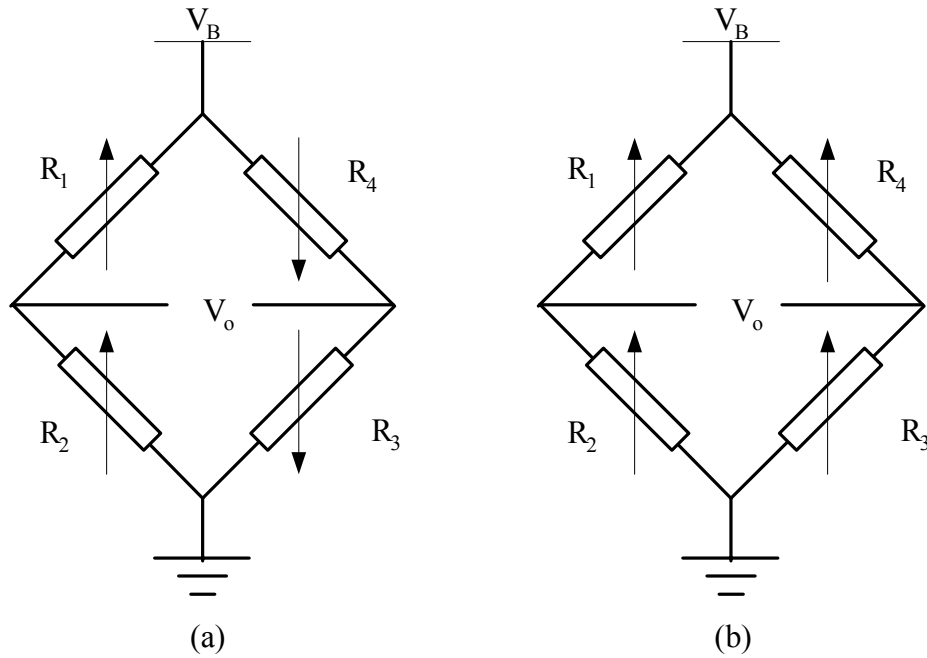


Figure 3-14. Wheatstone bridge subjected to cross-axis acceleration (a) and pressure (b).

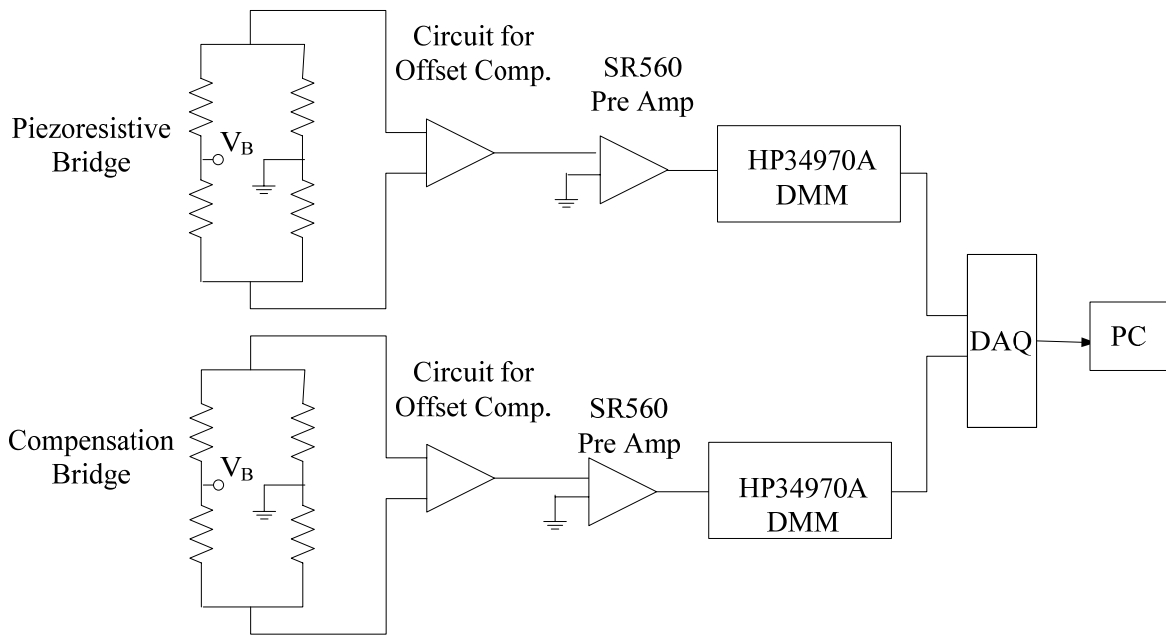


Figure 3-15. Schematic of the double-bridge temperature compensation configuration.

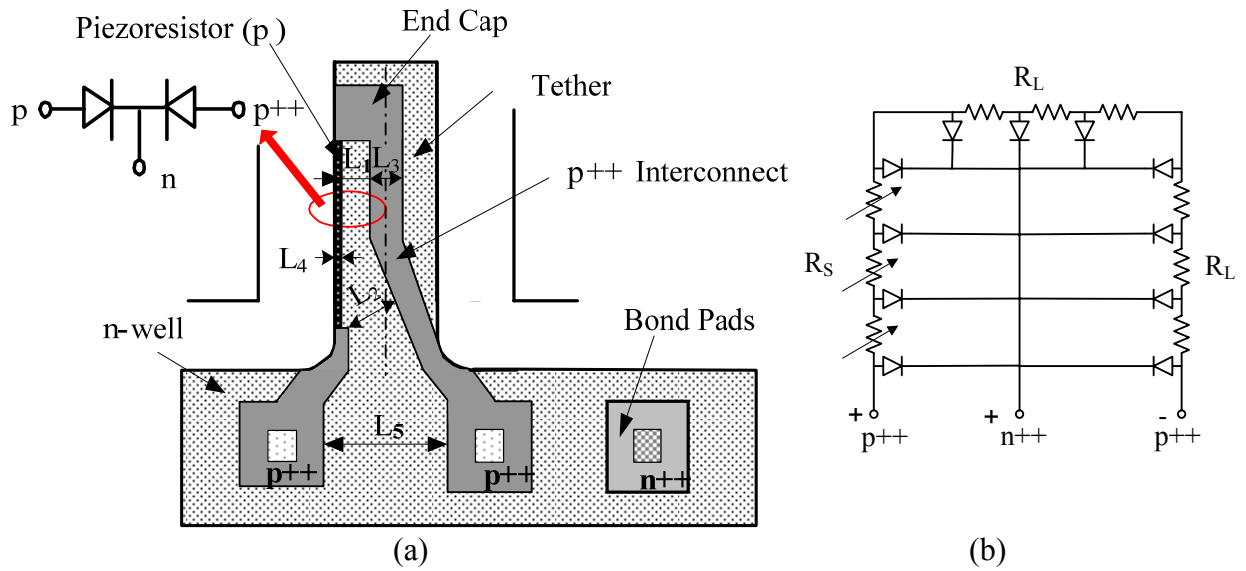


Figure 3-16. Top view schematic of the side-implanted piezoresistor and p++ interconnect in an n-well (a) and equivalent electric circuit indicating that the sensor and leads are junction isolated (b).

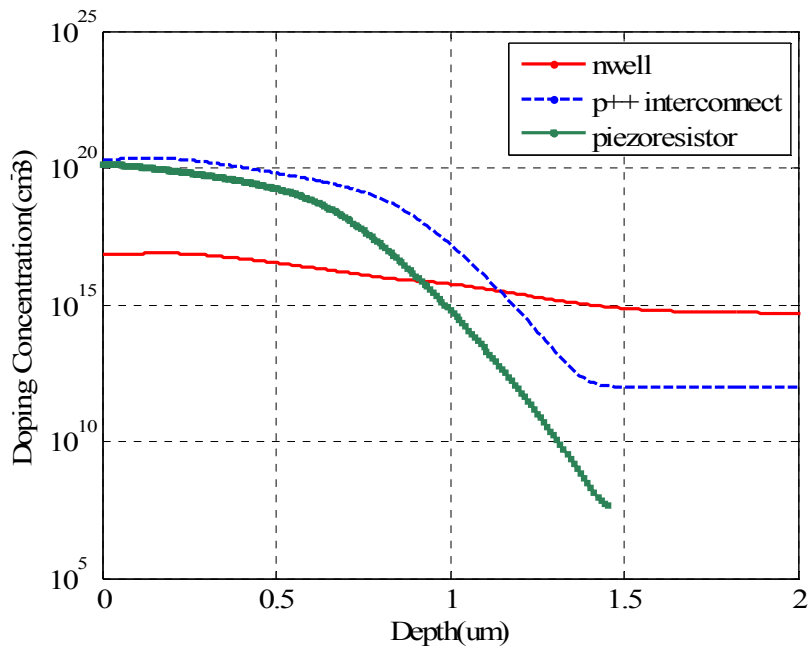


Figure 3-17. Doping profile of n-well, p++ interconnect, and piezoresistor using FLOOPS simulation.

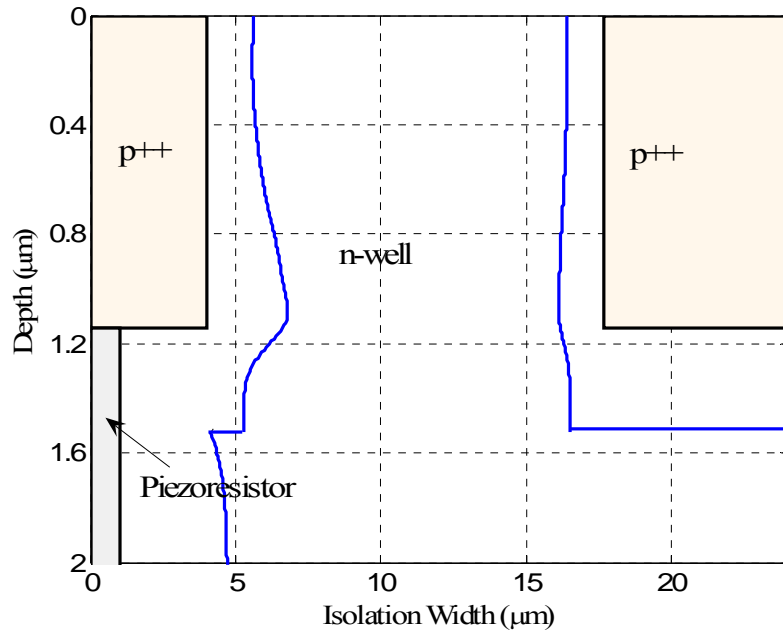


Figure 3-18. Cross view of isolation width between p++ interconnects (A-A cut in Figure 3-20).

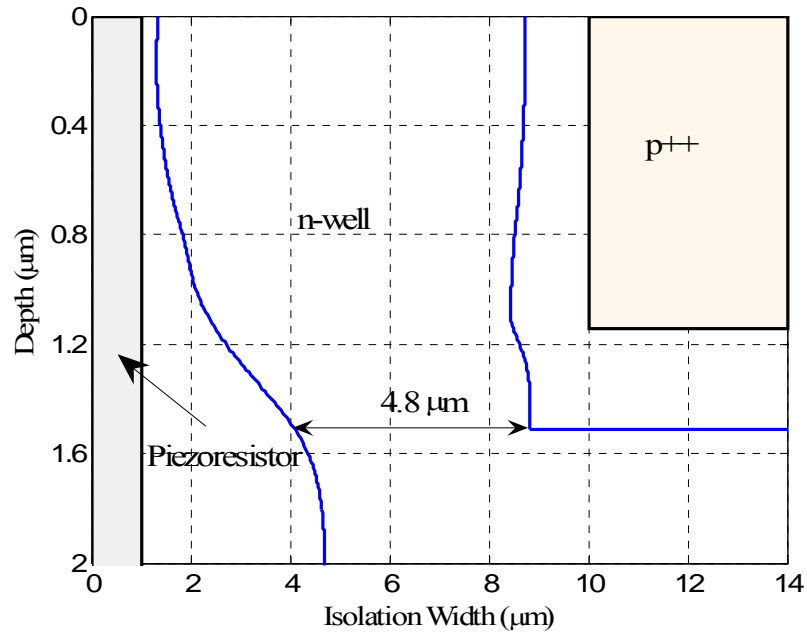


Figure 3-19. Cross view of isolation width between p++ interconnect and piezoresistor (B-B cut in Figure 3-20).

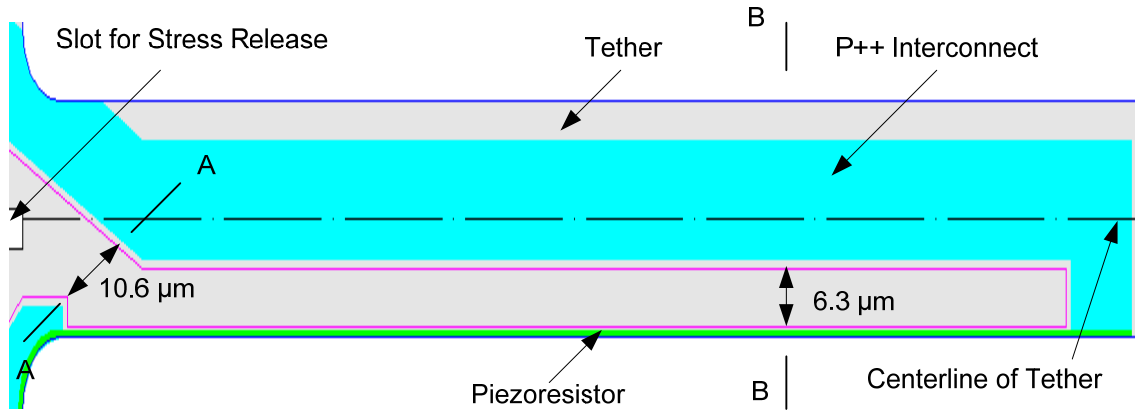


Figure 3-20. Top view of the isolation widths on a sensor tether.

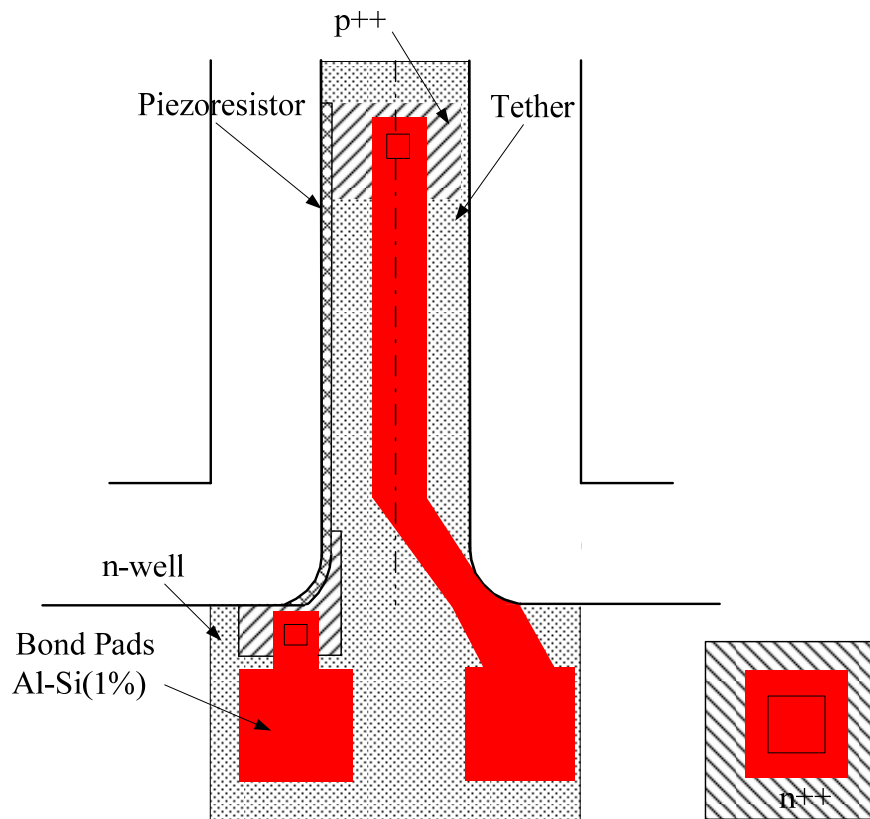


Figure 3-21. Top view schematic of the side-implanted piezoresistor with a metal line contact.

CHAPTER 4 DEVICE OPTIMIZATION

This chapter presents the nonlinearly constrained design optimization of a micromachined floating element piezoresistive shear stress sensor. First, the problem formulation is discussed, including the objective function and constraints based on flow conditions. Next, the optimization methodology is outlined. The optimization results are then presented and discussed. Finally, a post-optimization sensitivity analysis of the objective function is performed.

Problem Formulation

The objective function is selected based on tradeoffs identified between the sensitivity and noise floor of the shear stress sensor. The constraints are formed due to physical bounds, manufacturing limits and operational requirements [84], and are dependent on the flow conditions of the desired applications.

The objective function and constraints are functions of the design variables, including the geometry of the floating element structure and the piezoresistors, the surface doping concentration, and sensor excitation. The detailed discussion of the design variables chosen is presented in next subsection.

Design Variables

The objective function and constraints depend on geometry of sensors structures and piezoresistors, process related parameters, and sensor operational parameters. The geometry parameters include tether length L_t , tether width W_t , tether thickness, T_t , floating element length L_e , and piezoresistor length L_r , piezoresistor width W_r . The process related parameters include piezoresistor surface concentration N_s and junction depth y_j (assuming a uniform doping profile). The sensor operational parameter is the supplied bias voltage.

The geometry parameters of the sensor structure determine the mechanical characteristics of the sensor, such as sensitivity, linearity and bandwidth. Design issues related to the tether width W_t and tether thickness T_t are addressed here. As discussed in Chapter 3, the minimum tether width W_t is set to 30 μm to avoid p/n junction punch through. The tether thickness must be larger than the tether width to ensure that the cross-axis resonant frequency is larger than the in-plane resonant frequency. As shown in the representative structure in Table 3-1, the first mode is out of plane due to the tether thickness larger than the tether width. The increases in tether thickness results in bending stress decreases (Equation (3-6)), and thus sensitivity decreases (Equation (3-23)). On the other hand, the piezoresistor related parameters, such as piezoresistor length L_r , piezoresistor width W_r , and p/n junction depth y_j and surface concentration N_s , are related to noise floor and sensitivity.

For each design optimization, different tether thickness, junction depth and tether width may be achieved, but all designs are fabricated in one wafer due to economic constraints. Thus these parameters for each design must be set to the same value. In this research, the tether thickness is set to 50 μm considering the sensitivity of the shear stress sensor and SOI wafer availability. Due to the rough sidewall surface near the buried oxide layer after DRIE process and no passivation on the bottom of the tethers after final release, the high $1/f$ noise and current leakage became issues in the piezoresistor design [85]. Partridge et al.[51] investigated the accelerators with piezoresistors implanted in the top 15 μm (total thickness), 5 μm , 3 μm of the flexures, and found that 3 μm case has large sensitivity and low $1/f$ noise. In this research, piezoresistor width $W_r = 5 \mu\text{m}$ is chosen to avoid current leakage while maintaining high

performance. A junction depth of $y_j = 1 \mu\text{m}$ is chosen taking account the piezoresistor and p++ interconnection and the manufacturing constraint.

In summary, six design variables are included in the optimization design, and they are tether length L_t , tether width W_t , floating element length L_e , and piezoresistor length L_r , piezoresistor surface doping concentration N_s and bias voltage V_B .

Objective Function

As stated in Chapter 1, to accurately recognize the fluctuating wall shear stress in the turbulent boundary layer, the measurement device must possess sufficiently high spatial and temporal resolution as well as a low MDS, which is defined as the ratio of noise floor to the sensitivity. Therefore, lowering the noise floor and increasing sensitivity are favorable in shear stress sensor design to achieve a low MDS [84]. Some parameters, such as junction depth, surface doping concentration and bias voltage, affect both sensitivity and noise floor creating tradeoffs between these performance parameters. The following discusses the tradeoffs in sensitivity and noise floor and the arrival at the MDS as the objective function of the optimization.

Junction depth, y_j , and surface doping concentration, N_s , are two major factors involved in processing that affect sensitivity and noise floor. As discussed in chapter 3, changes in N_s while keeping y_j constant invoke tradeoffs between noise and sensitivity. If N_s increases, the resistivity of the piezoresistor decreases and the total carrier number increases. This leads to the reduction of thermal noise and $1/f$ noise. Conversely, sensitivity decreases due to the reduction of the piezoresistive coefficient π_l from high doping concentration (Equation (3-23)).

The bias voltage V_b also affects both sensitivity and noise floor. As V_b increases, the sensitivity increases (Equation (3-35)) because the output voltage is directly proportional to the bias voltage. The voltage noise contribution from $1/f$ noise also increases squarely as indicated by Equation (3-38).

By establishing the MDS as the objective function, a balance between noise floor and sensitivity is achieved. Previous researchers have investigated the potential and methods in piezoresistive sensor optimization. Harley and Kenny [47] presented an informal graphical design optimization guidelines in the form of design charts by varying the dimensions of the cantilever, the geometry of the piezoresistor, doping level, and process issues related to sensitivity and noise floor. Papila et al. [84] performed a piezoresistive microphone Pareto design optimization, in which the tradeoff between pressure sensitivity and electronic noise is investigated. The Pareto curve indicated that the MDS in units of pressure is the appropriate parameter for performance optimization.

Constraints

The constraints are determined by physical bounds, fabrication limits and performance requirements [84]. The constraints used in this optimization and their associated physical explanations are listed below:

- Piezoresistor geometry: $L_r/L_t \leq 0.4$, as discussed in Chapter 3, stress changes sign at the longitudinal center of the tether (shown in Figure 3-6). Thus, the sensitivity will be reduced if the length of the piezoresistor is larger than $L_t/2$. As a result, the maximum piezoresistor length is limited to 40% of the tether length
- Resistance: $R_s/R_L \geq 3$, represents a balance between the sensor resistance R_s being 3 times larger than the interconnect resistance R_L , but small enough to minimize electromagnetic interference (EMI).
- Frequency: $f_r \geq f_{\min}$, puts a bandwidth constraint in the design. The constraint changes with flow conditions.

- Power consumption: $P_{ow} \leq 0.1$, where $P_{ow} = V_B^2 / (R_S + R_L)$. When P_{ow} increases to a large value, the temperature of the piezoresistor will increase due to Joule heating resulting in voltage drift and eventually electromigration.
- Nonlinearity: $|\Delta_{NL} - \Delta_L| / \Delta_{NL} \leq 3\%$, device linearity is required to keep spectral fidelity for time-resolved measurements.
- In-plane resonant frequency: $T_t > W_t$. To avoid disturbing the flow at the sensor resonance, the tether thickness T_t is required to be larger than tether width W_t to ensure the onset of the in-plane resonant frequency occurs before the out of plane. In this dissertation, the minimum tether width is $30 \mu\text{m}$ and its upper bound is set to $40 \mu\text{m}$, thus the tether thickness is set to $50 \mu\text{m}$.
- Lower bounds (LB) and upper bounds (UB): $LB \leq (L_t, W_t, W_e, L_r, N_s, V_B) \leq UB$, present the limitation of the design variables. LB and UB are given in Table 4-2 based on the candidate shear stress design specifications and design issues related to fabrication.

In summary, both the objective function and constraints are nonlinear. Therefore, the optimal performance design deals with solving the constrained nonlinear optimization problem.

Candidate Flows

Several sensor specifications associated with various flow phenomena, ranging from low speed flow to supersonic and hypersonic flow, are listed in Table 4-1. Here τ_{\max} is the maximum shear stress to be measured and constrained by non-linearity, f_{\min} is the minimum resonant frequency to provide adequate temporal resolution and $L_{e\max}$ is the maximum floating element size that determines the lowest tolerable spatial resolution, $W_{t\min}$ is the minimum tether width that is limited by the junction isolation, and T_t is the minimum thickness that is constrained by the in-plane resonant frequency. The temporal and spatial resolution f_{\min} and $L_{e\max}$ are chosen to approach the Kolmogorov time and length scales, but are sufficiently conservative to yield a proof of concept device.

Methodology

The design problem is formulated to find the optimum dimensions of the floating element and tethers, geometry and surface doping concentration of piezoresistors, and bias voltage for each candidate flow. Mathematically, the optimization seeks to minimize the MDS subject to constraints. The key points regarding the optimization of the minimum detectable shear stress, τ_{\min} , are summarized below:

Design variables: L_t, W_t, W_e, L_r, V_B and N_s .

Objective function: minimize $F(X) = \tau_{\min}$, where X is the design variable vector.

Constraints:

$$\begin{aligned}
 g_1 &= L_r / (0.4L_t) - 1 \leq 0; & g_2 &= f_{\min} / f_r - 1 \leq 0; & g_3 &= 1 - R_s / 3R_L \leq 0; \\
 g_4 &= 10V_B^2 / (R_s + R_L) - 1 \leq 0; & g_5 &= |\delta_{NL} - \delta_L| / 0.03\delta_{NL} - 1 \leq 0; \\
 g_i &= LB_i / x_i - 1 \leq 0, \quad i = 6, 8, \dots, 11; & g_j &= x_j / UB_j - 1 \leq 0, \quad j = 12, 13 \dots 17.
 \end{aligned}$$

where $x_i = L_t, W_t, W_e, L_r, N_s$ and V_B . Since the magnitudes of design variables differ by several order of magnitude (Table 4-2), all variables are non-dimensionalized to avoid singularities in the program. This nonlinear constrained optimization is implemented using the function *fmincon* in MATLAB[®] (2006b) [86] optimization Toolbox, which employs sequential quadratic programming (SQP) for nonlinear constrained problems and calculates the gradients by finite difference method. The optimum value of N_s for different designs might be different. All designs, however, are fabricated on one wafer. Therefore, surface concentration, N_s , for all designs must be set to the same value. In this dissertation, the optimal N_s for first three cases were the same and is $N_s = 7.7 \times 10^{19} \text{ cm}^{-3}$. This value was chosen as the surface concentration for

all designs. The optimization was re-implemented using this fixed concentration following the same steps described above.

The SQP method is a local optimizer and is highly dependent on the initial value. The initial designs are selected randomly, and a number of local optimum solutions from different initial designs were obtained. The solution identifies one best design points as the optimal solution. A global optimization algorithm using particle swarms [87] is also employed to investigate the possibility of improving the optimum solutions. It is found that global optimization solution is very similar to the optimization results obtained by *fmincon* function. The global optimization results have a large computational cost.

Optimization Results and Discussion

In the optimization, the doping profile is assumed to be uniform to simplify the modeling. The Gaussian profile is more accurate than a uniform profile, but it is not employed in this research to avoid computational cost. The doping concentration for p++ interconnect is achieved as $2.0 \times 10^{20} \text{ cm}^{-3}$, with a junction depth of $1 \mu\text{m}$ for all designs. In this research, the material properties of silicon is fixed.

The resulting optimization design is shown in Table 4-3. The highlights are active constraints. Since the low resistance results in low thermal noise, but the power dissipation increases. Therefore, the power constraint is always active (close for case 9). For each device, the dynamic range from the optimum design is in excess of 75 dB. Kuhn-Tucker conditions [88] are conducted to check the optimality and active constraints, which are stated as follows:

- Lagrange multipliers λ_j are nonnegative, and satisfy equation (4-1)

$$\frac{\partial F}{\partial x_i} - \sum_{j=1}^{n_g} \lambda_j \frac{\partial g_j}{\partial x_i} = 0 \quad i=1,2,\dots,m, \quad (4-1)$$

where n_g is the total number of constraints, and m is the total number of design variables.

Lagrange multipliers λ_j are obtained by the *fmincon* *MATLAB* function.

- The corresponding λ_j is zero if a constraint is not active. The active constraints for each case are indicated in bold font in Table 4-3.

Once the optimum design for uniform doping is obtained, non-uniform doping profiles are applied to achieve the final performance of the sensor. The optimization flow chart is shown in Figure 4-1. The non-uniform doping profiles are obtained by FLOOPS simulation [26], where sidewall boron implantation to amorphous silicon is simulated by SRIM simulation [79] and imported to FLOOPS. The surface concentration of the piezoresistor, the piezoresistive interconnection, and n-well are achieved to $7.7 \times 10^{19} \text{ cm}^{-3}$, $2.0 \times 10^{20} \text{ cm}^{-3}$, and $7 \times 10^{16} \text{ cm}^{-3}$, respectively, as shown in Figure 3-17. The results indicate that non-uniform doping profiles yield approximately a 5 dB decrease in dynamic range. Therefore, implementing a Gaussian profile as part of the optimization would result in a more accurate model and thus optimal design.

Sensitivity Analysis

Due to parameter uncertainty caused by process, τ_{\min} may achieve different values than theoretical optimization. The sensitivity analysis is implemented to understand sensitivity of MDS to the variations of the design variables, constraints, and fixed parameters at the optimum design. Therefore, sensitivity analysis is a post-optimization step, which involves two parts:

- Sensitivity of the objective function to design variables at the optimum design.
- Sensitivity of the objective functions to the fixed parameters at the optimum design, where the effect of a change in the active constraints on the objective function is taken into account.

For the sensitivity analysis with respect to the design variables, logarithmic derivative [88] is employed to measure the sensitivity of MDS to uncertainty of design parameters at the optimum design,

$$\frac{\partial \log(\tau_{\min})}{\partial \log(x_i)} = \frac{\partial \tau_{\min}}{\partial x_i} \frac{x_i}{\tau_{\min}}, \quad (4-2)$$

where $x_i = L_t, W_t, W_e, L_r, V_B$ and N_s .

For the sensitivity analysis with respect to the fixed parameters, equation (4-2) is invalid if the nonlinear inequality constraints are active. Lagrange multipliers based on the Kuhn-Tucker conditions [88] is employed to calculate the sensitivity of the optimal solution to the fixed parameters. Assuming that the objective function and the constraints depend on a fixed parameter p , so that the optimization problem is defines as,

$$\begin{aligned} & \text{minimize } F(X, p) \\ & \text{such that } g_j(X, p) \geq 0 \quad j=1,2,\dots,17. \end{aligned} \quad (4-3)$$

The gradient of F with respect to p is given as [88],

$$\frac{dF}{dp} = \frac{\partial F}{\partial p} - \lambda^T \frac{\partial g_a}{\partial p}, \quad (4-4)$$

where g_a denotes the active constraint functions and $g_a = 0$ from Kuhn-Tucker conditions. The equation (4-4) indicates that the Lagrange multipliers are a measure of the effect of a change of the constraints to the objective function. Lagrange multipliers $\lambda = 0$ for active constraints, otherwise it is obtained by

$$\lambda = (N^T N)^{-1} N^T \nabla F, \quad (4-5)$$

where N and ∇F are defined as

$$N = \frac{\partial g_j}{\partial x_i}, \quad j=1,2,\dots,17, i=1,2,\dots,6 \quad (4-6)$$

and
$$\nabla F = \frac{\partial F}{\partial x_i} \quad i=1,2\dots6. \quad (4-7)$$

The sensitivity of τ_{\min} to uncertainty of the fixed parameters is given as

$$\frac{\partial \tau_{\min} / \tau_{\min}}{\partial p / p} = \left(\frac{\partial \tau_{\min}}{\partial p} - \lambda^T \frac{\partial g_a}{\partial p} \right) \frac{p}{\tau_{\min}}. \quad (4-8)$$

λ can be obtained from the output of *fmincon* function directly. The fixed parameters are

$$p = y_j, W_r, T_r, N_s.$$

For case 1, power is the active inequality constraint, and the associated Lagrange multiplier, $\lambda = 0.0026179$, is obtained from MATLAB calculation. Therefore, Equation (4-2) is employed to calculate the sensitivity of MDS to uncertainty of design parameters (L_t , W_t , W_e , L_r and V_b) at the optimum design. Equation (4-8) is employed for the fixed parameters (y_j , W_r , T_r and N_s). Figure 4-1 shows the sensitivity of τ_{\min} to uncertainty of the design variables and fixed parameters for case 1, i.e., 10% change of the tether width causes 19% change of the minimum detectable shear stress. It is illustrated that τ_{\min} is sensitive to variation of tether width, W_t , tether length, L_t , floating element width, W_e , and junction depth, y_j . The MDS is less sensitive to variation of piezoresistor length L_r . In summary, τ_{\min} is very sensitive to uncertainties of tether and element dimensions, junction depth and width of the piezoresistors, and less sensitive to uncertainties of piezoresistor length.

Summary

This section described the choice of objective function and associated constraints. The optimization has been implemented for nine designs, from low Reynolds number flow to supersonic and hypersonic flow. The optimization results indicate that the dynamic range exceeds 75 dB for all designs based on a uniform doping profile. Accounting for non-uniform

doping profile results in a 5 dB decrease in dynamic range. The sensitivity analysis indicates that the MDS is very sensitive to uncertainties of tether and element dimensions, junction depth and width of the piezoresistors, and less sensitivity to uncertainties of piezoresistor length.

Table 4-1. The candidate shear stress sensor specifications.

Device	Low Speed			Supersonic, High Re			Hypersonic, Underwater		
	1	2	3	4	5	6	7	8	9
τ_{\max} (Pa)	5	5	5	50	50	100	100	500	500
f_{\min} (kHz)	5	5	10	10	50	50	100	100	200
$L_{e\max}$ (μm)	1000	1500	1000	1000	1000	1000	500	500	500
$W_{t\min}$ (μm)	30	30	30	30	30	30	30	30	30
T_t (μm)	50	50	50	50	50	50	50	50	50

Table 4-2. Upper and lower bounds associated with the specifications in Table 4-1.

	Design Variables and $LB-UB$						Flow Description	
	L_t (μm)	W_t (μm)	L_e (μm)	L_r (μm)	V_B (V)	N_s (cm^{-3})	τ_{\min} (Pa)	f_{\min} (kHz)
1	100 - 1000	30-40	100 - 1000	50 - 400	5 - 10	5e+18 - 2e+20	5	5
2	100 - 1000	30-40	100 - 1500	50 - 400	5 - 10	5e+18 - 2e+20	5	5
3	100 - 1000	30-40	100 - 1000	50 - 400	5 - 10	5e+18 - 2e+20	5	10
4	100 - 1000	30-40	100 - 1000	50 - 400	5 - 10	5e+18 - 2e+20	50	10
5	100 - 1000	30-40	100 - 1000	50 - 400	5 - 10	5e+18 - 2e+20	50	50
6	100 - 1000	30-40	100 - 1000	50 - 400	5 - 10	5e+18 - 2e+20	100	50
7	100 - 1000	30-40	100 - 500	50 - 400	5 - 10	5e+18 - 2e+20	100	100
8	100 - 1000	30-40	100 - 500	50 - 400	5 - 10	5e+18 - 2e+20	500	100
9	100 - 1000	30-40	100 - 500	50 - 400	5 - 10	5e+18 - 2e+20	500	200

Table 4-3. Optimization results for the cases specified in Table 4-1 (bold for active constraints).

Parameter	Case1	Case2	Case3	Case4	Case5	Case6	Case7	Case8	Case9
τ_{\max} (Pa)	5	5	5	50	50	100	100	500	500
L_t (μm)	1000	1000	1000	991.2	343.6	348.7	308.8	500.4	500
W_t (μm)	30	30	30	30	30	30.7	30	30	30
W_e (μm)	1000	1500	983.5	996.1	1000	993.3	499.1	250.2	100
L_r (μm)	228.5	228.5	228.5	228.5	98.8	99.9	88.6	126.8	117.7
V_B (V)	10	10	10	10	6.8	6.8	6.5	7.6	6.0
P_{ow} (W)	0.1	0.1	0.1	0.1	0.1	0.1	0.1	0.1	0.07
f_r (kHz)	9.8	6.60	10	10	50.53	50.01	130.15	104.07	231.11
R_S (Ω)	851	851	851	851	368	372	330	470	438
R_L (Ω)	149	149	149	149	94	94	89	105	102
S_M (V/Pa)	3.65e-5	7.92e-5	3.54e-5	3.58e-5	6.64e-6	6.40e-6	1.47e-6	1.13e-6	4.20e-7
V_N (nV)	21.1	21.1	21.1	21.1	11.0	10.97	10.95	11.19	9.54
τ_{\min} (mPa)	0.58	0.27	0.60	0.33	1.66	1.72	7.44	9.88	2.28e-2
DR (dB)	78.7	85.4	78.5	103.7	89.6	95.3	82.6	94.1	86.8

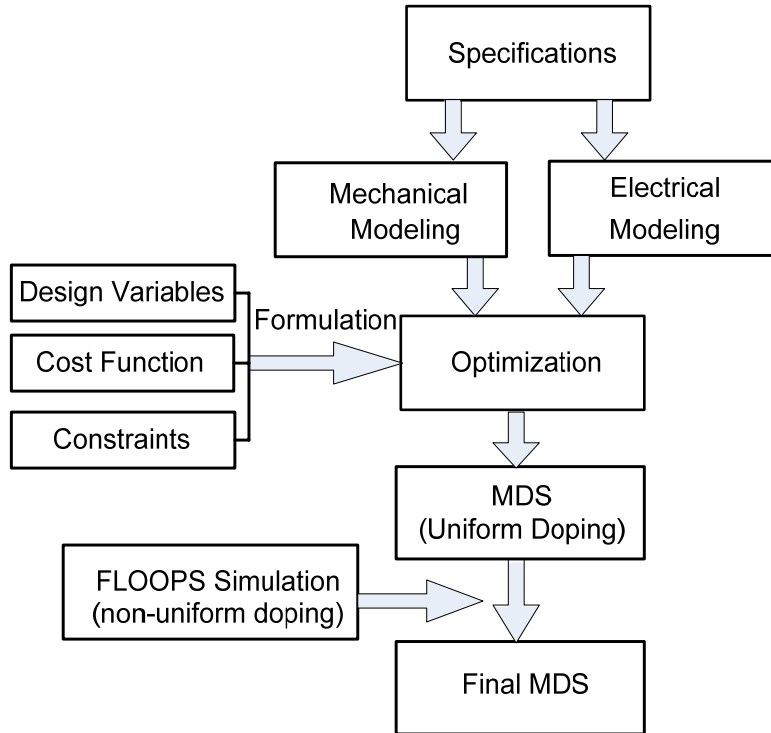


Figure 4-1. Flow chart of design optimization of the piezoresistive shear stress sensor.

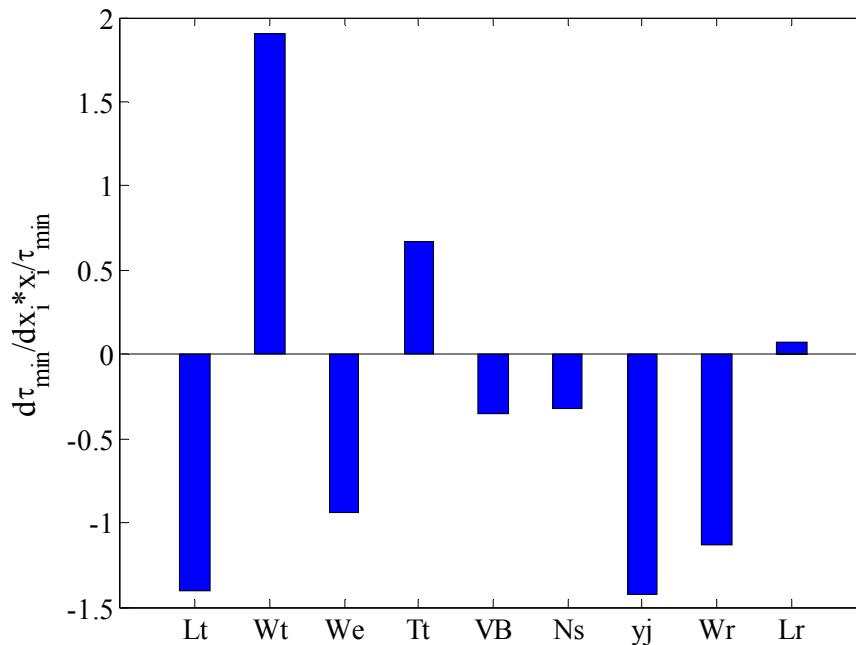


Figure 4-2. Logarithmic derivative of objective function τ_{\min} with respect to parameters (Case1).

CHAPTER 5 FABRICATION AND PACKAGING

The fabrication process and packaging of the side-implanted piezoresistive shear stress sensor are presented in this chapter, with the aid of masks and schematic cross section drawings. A detailed process flow is given in Appendix C, which lists all the process parameters, equipments and labs for each step. The detailed packaging approach for wind tunnel testing is also presented.

Fabrication Overview and Challenges

The first generation of the shear stress sensor is fabricated in an 8-mask, silicon bulk-micromachining process. All the masks are generated using AutoCAD[®] 2002 and manufactured in Photo Sciences, Inc (PSI). It is described in detail in the following sections. Some challenges in this process are addressed before starting the process flow:

- Side-implanted piezoresistors: boron is side implanted into the silicon tethers to form the piezoresistors with an oblique angle of 54° normal to the top surface. The traditional piezoresistor is formed by top implantation. The doping profile for side-implantation is simulated via FLOOPS, and the accuracy of the profile needs to be judged only after device testing.
- Trench filling: 50- μm -deep trenches were etched on the top surface to define the tethers. Trench filling is required to obtain good photoresist coverage before subsequent deposition and patterning of the metallization layer.
- Junction isolation: the space between piezoresistors and p⁺⁺ interconnects should be larger than the isolation width to avoid p/n punch through, as discussed in chapter 3.

Fabrication Process

The fabrication process starts with a 100-mm (100) silicon-on-insulator (SOI) wafer with a 50- μm -thick 1~5 $\Omega\text{-cm}$ n-type silicon device layer above a 1.5- μm -thick buried silicon dioxide (BOX) layer. The corresponding background doping concentration is from $2.5 \times 10^{15} \text{ cm}^{-3}$ to $5 \times 10^{14} \text{ cm}^{-3}$. The total wafer thickness is 450 μm . A brief overview of the process is as follows. The four side-implanted piezoresistors are first formed by boron oblique implantation.

The structure of the sensor is then defined by DRIE Si etch. Thermal dry oxide is grown for high quality passivation. Al-Si (1%) is deposited and patterned to form the bond pads. PECVD nitride is deposited as a moisture barrier layer. Finally, the structure is released from the backside via DRIE Si and RIE of the oxide and nitride. The process flow is broken down into 8 major steps as follows:

- a. The n-well formation:** the fabrication begins with the formation of the n-well by a phosphorus blanket implantation (Figure 5-1 (2)). An energy of 150 keV and a dose of $4.0 \times 10^{12} \text{ cm}^{-2}$ are used to achieve a surface concentration of $6.5 \times 10^{16} \text{ cm}^{-3}$ to control the space-charge layer thickness of the reverse-biased p/n junction-isolated piezoresistors.
- b. Reverse bias contact:** a 100 nm thin oxide layer is then deposited via plasma-enhanced chemical vapor deposition (PECVD) and patterned, then etched via buffered oxide etch (BOE) in preparation of the reverse-bias contact implant. This step also creates alignment marks on the top surface. Phosphorus is then implanted with energy of 80 keV and dose of $9.0 \times 10^{13} \text{ cm}^{-2}$ to achieve a n⁺⁺ region with a surface concentration of $1.8 \times 10^{18} \text{ cm}^{-3}$ (Figure 5-1 (4)). The device is then annealed at 1000 °C for 450 minutes to drive-in the impurities.
- c. Piezoresistor interconnects:** the oxide is selectively removed by BOE. Then, a two-step Ge preamorphization implant is performed to minimize the effect of random channeling tail caused by the subsequent high-dose boron implantation [66], which provides a heavily doped Ohmic body contact. The preamorphization implant energies are 160 keV and 50 keV, respectively, and a dose of 10^{15} cm^{-2} . This preamorphization is to ensure no more than 2% of the implanted boron dose penetrates into the substrate [89]. Then boron is implanted into the silicon with a dose of $1.2 \times 10^{16} \text{ cm}^{-2}$ and an energy of 50 keV to provide Ohmic contacts (Figure 5-1 (5)). The resulting surface concentration and junction depth, $x_{j,p}$, while taking into account the

thermal budget of the entire process, are simulated by FLOOPS to be $1.96 \times 10^{20} \text{ cm}^{-3}$ and $1 \text{ } \mu\text{m}$, respectively. The interconnect region begins from the edge of the tether and distributes symmetrically along the centerline of the tethers to minimize the sensitivity error, with a larger width on the end cap to decrease the resistance. The FLOOPS simulation file is given in Appendix D.

d. “Nested” mask release: a $1 \text{ } \mu\text{m}$ oxide layer is deposited via PECVD and patterned via reactive ion etch (RIE) [90] to serve as a nested mask for the deep reactive ion etch (DRIE) [91] that defines the tethers and floating element (Figure 5-1 (7)). New alignment marks are also created in this step.

e. Side wall etch and side wall implantation: the wafers are then patterned using the mask SIM (Figure 5-1 (8)). To ensure good contact between the piezoresistor and the p++ interconnect, the SIM mask has a $4 \text{ } \mu\text{m}$ overlap with the p++ interconnect on the edge of the tether, $10 \text{ } \mu\text{m}$ overlap with the p++ interconnect on the end cap, and $4 \text{ } \mu\text{m}$ overlap with sidewall. Prior to DRIE, the native oxide or oxide residues are etched via BOE about one minute. The Si is then etched vertically to approximately $8 \text{ } \mu\text{m}$ deep by DRIE to form the trenches for the sidewall oblique implant, as shown in Figure 5-2 (scanning electron microscope (SEM) top view). The trench width is set to $(5 + 1.1 \text{ } \mu\text{m}) \times \tan(54^\circ) \approx 8.5 \text{ } \mu\text{m}$ to achieve a $5 \text{ } \mu\text{m}$ implant, where 54° is the implant tilt angle from the normal axis, and $1.1 \text{ } \mu\text{m}$ is the thickness of the oxide layer. The sidewall implantation is restricted on the top $5 \text{ } \mu\text{m}$ to ensure the silicon surface on which the boron implanted is smooth and avoid forming the current leakage path on the bottom [85]. This can reduce the $1/f$ noise at low frequency [85]. The basic recipes on STS DRIE system and Unaxis RIE systems are shown in Appendix E.

The extruded oxide resulting from the DRIE is etched via BOE (6:1) for one minute, as shown via the scanning electron microscope image in Figure 5-3. This avoids the protruded oxide blocking the implant dosage to the side wall. Hydrogen annealing (1000° C, 10 mTorr for 5 minutes) [92] is performed to smooth the scallops on the sidewalls that arise from the DRIE process, which will improve the noise floor [25]. A 0.1 μm oxide layer is thermally grown as a thin implant oxide layer on the sidewall, which must be accounted for in the thermal budget.

After a two-step Germanium preamorphization implant, boron is then implanted with an energy of 50 keV, a dose of 2×10^{16} cm⁻² (two times of the simulation dose to compensate the solubility loss at high dosage) and an oblique angle of 54° to achieve a 5 μm shadow side wall implantation (shown in Figure 5-1 (9)).

f. Tether definition: the oxide on the trench bottom is then etched via DRIE while the oxide on the sidewall is left to protect the doped sidewall, as shown in Figure 5-4. This is a time-controlled process: an over-etch will expose silicon on the edge of the sidewall of the tether (Figure 5-5), while an under-etch will create a “silicon grass” effect [93] after the subsequent DRIE silicon etch due to the oxide residues that acts as a micromask (Figure 5-6). The channels/trenches are then etched via DRIE with the BOX as an etch stop, as shown in Figure 5-7 (note the rough surface is caused by the dicing saw). The tether sidewall oxide is then etched for two minutes by BOE (6:1). Subsequently, the wafers are annealed at 1000° C for 60 min to drive in the boron to form the piezoresistors. A 0.1 μm thin dry oxide layer was thermally grown at 975° C as an electrical passivation layer. The temperature 975° C is selected to avoid excessive diffusion and excessive compressive stress when the temperature is below 950° C [94]. Meanwhile, the boron is segregated into the oxide from the silicon.

g. Metallization and nitride passivation: since there are 50- μm -deep trenches on the wafer for tether release, it is necessary to fill the trench to achieve good photoresist coverage before subsequent wafer patterning. A two-step trench filling process is performed as follows: first, a thin layer of photoresist AZ1512 is coated and soft baked, then a thick photoresist AZ9260 is coated and soft baked; second, the wafer is flood exposed for 300 seconds and developed using developer AZ400 until the surface is clear. Thus, the trench can be reduced from 50 μm to only 5~6 μm deep if following the above process once or twice.

After filling the trenches with photoresist, the oxide is patterned and then etched via BOE (6:1) to open contact vias for Al sputtering. This step is very critical for the quality of the metal contact. Since the boron laden silicon dioxide etches much slower than the standard oxide etching (1000 $\text{\AA}/\text{min}$), an over etch is required to remove all oxide to ensure an Ohmic contact. Any residual oxide left over will result in Schottky diode effect. A 1- μm -thick layer of Al-Si (1%) is sputtered and patterned via RIE to form the metal interconnects (Figure 5-1 (12)). A 200-nm-thick, low-stress silicon nitride layer is deposited via PECVD to form a protective moisture barrier. The bond pads are exposed by patterning and plasma etching the silicon nitride via RIE.

h. Backside release: to protect the device, the front side of the wafer is coated with a 10- μm -thick photoresist layer. The wafers are then patterned from the backside using front-to-back alignment. The structure is released from the backside using DRIE up to the BOX layer (Figure 5-1 (14)), along with an oxide and nitride etch using RIE (Figure 5-1 (15)). Finally, a post-metallization anneal is performed in forming gas (4% H_2 , 96% N_2) at 450° C for 1 hour [95]. This annealing allows the aluminum to react with the native oxide to remove the tunneling oxide, and allow the hydrogen to passivate the interface traps. This improves the contact resistance and

reduces the electrical noise floor [25]. The fabricated device is shown in Figure 5-8 and the close view of the piezoresistors is shown in Figure 5-9. The trenches between each device were patterned and created during back side release, thus the die can be easily separated by tweezers.

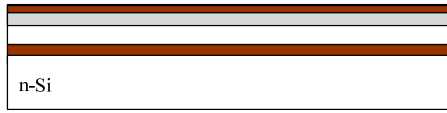
Sensor Packaging for Wind Tunnel Testing

After fabrication, the individual die (6.2 mm×6.2 mm) were then packaged in a custom printed circuit board (PCB) (20 mm×20 mm) designed for modularity. The PCB layout was performed using Protel and was manufactured by a commercial vendor, Sierra Proto Express. The MEMS device die and PCB were then packaged by Engent Inc. The MEMS die are flush-mounted into a machined cavity in the PCB and sealed with epoxy at the perimeter. The aluminum bond pads are then bonded to gold pads on the PCB. Subsequent to the bonding process, the wire bonds are covered by non-conductive epoxy to protect the wire bonds from the gas flow in the calibration wind tunnel or flow cell. The roughness of the epoxy is less than 300 μm and is located (3.2 mm) downstream of the sensing element to mitigate flow disturbances. The PCB package is then flush-mounted into a Lucite package, which in turn is flush mounted in an aluminum plate to minimize flow disturbance. Figure 5-10 shows the PCB embedded in the Lucite package. Copper wires (gauge 26) pass from underneath up through the vias in the PCB and are soldered to PCB via rings. The wire is reinforced by the glue on the backside of the Lucite package.

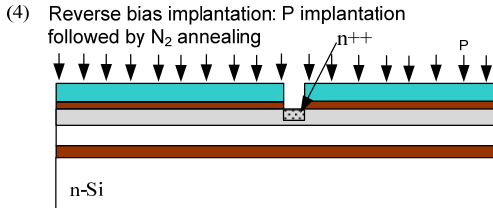
An interface circuit board was designed for offset compensation and signal amplification, as shown in Figure 5-11. This board includes two sets of compensation circuitry: one for active bridge, another for dummy bridge. Each circuit has two amplifying stages: the first stage is used to null the amplified offset, and the second stage is to amplify the compensated signal. The detailed description of the interface circuit for offset compensation is given in Chapter 6. This

board is attached on the backside of the device package and supported by two screws that connect it to the Lucite packaging. The copper wires for the signal output and voltage supply from the Lucite plug are soldered to this board. There are eight BNC connectors for the amplified signal outputs and power supplies.

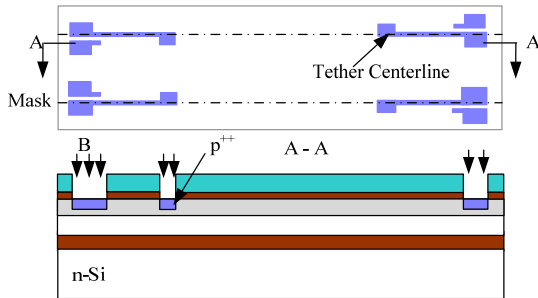
- (1) Starting with SOI wafer with 50um top Si layer
- (2) Blanket P implantation to create n-well



- (3) PECVD oxide (0.1um). Pattern & BOE etch oxide

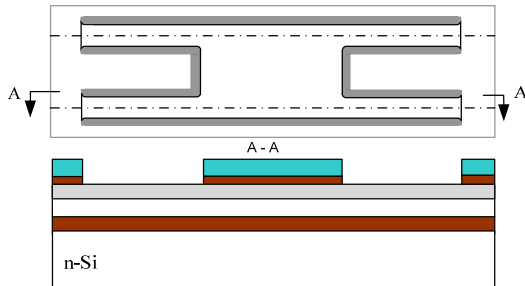


- (5) Pattern & wet etch oxide followed by "piezo" contact implantation

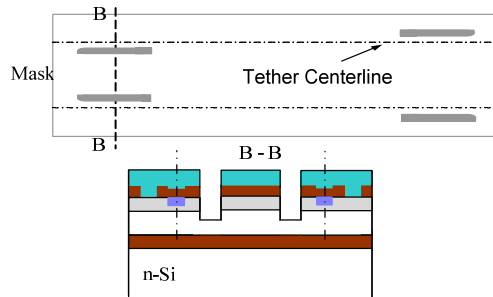


- (6) PECVD oxide (1um)

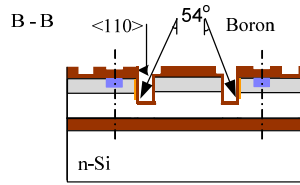
- (7) Pattern & dry etch oxide



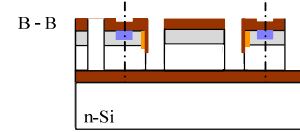
- (8) Pattern & DRIE trench ~10um for side wall implantation followed by H2 annealing



- (9) Thermal oxidation followed by side wall B implantation

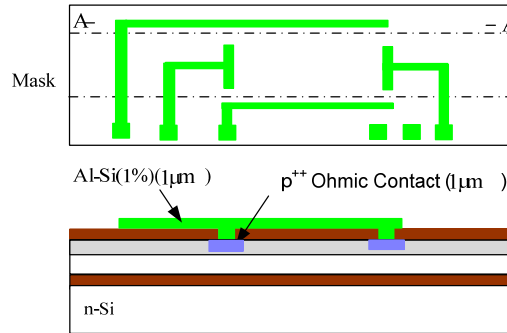


- (10) Remove top oxide(0.1um) & DRIE Si (50um) to define tethers



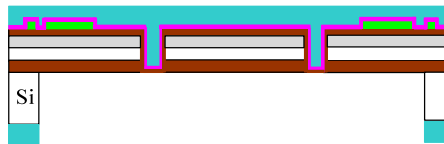
- (11) Wet etch oxide(0.1um), thermal diffusion and thermal oxidation

- (12) Trench filling, Wet etch oxide to open contact vias followed by Al-Si(1%) sputtering and Al etch via RIE

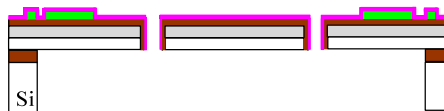


- (13) PECVD silicon nitride then pattern it to expose the bond pads

- (14) Backside Si DRIE etch



- (15) RIE etch oxide and nitride to release the structure



- (16) Forming gas anneal at 450 degree for 1 hour

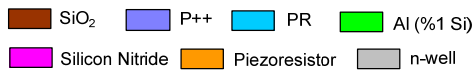


Figure 5-1. Process flow of the side-implanted piezoresistive shear stress sensor.

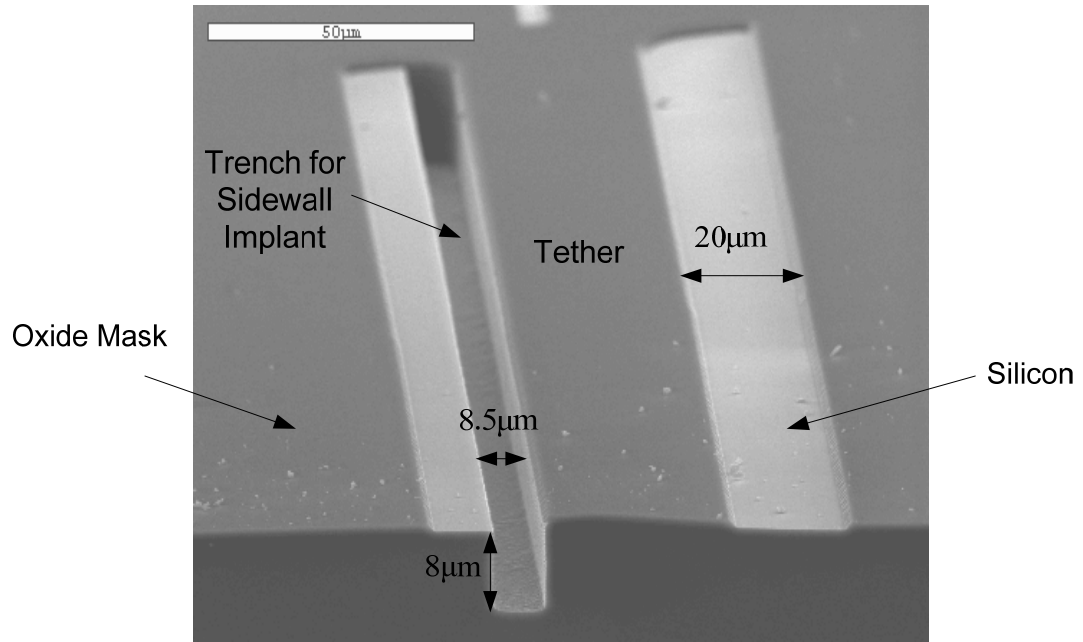


Figure 5-2. SEM side view of side wall trench after DRIE Si.

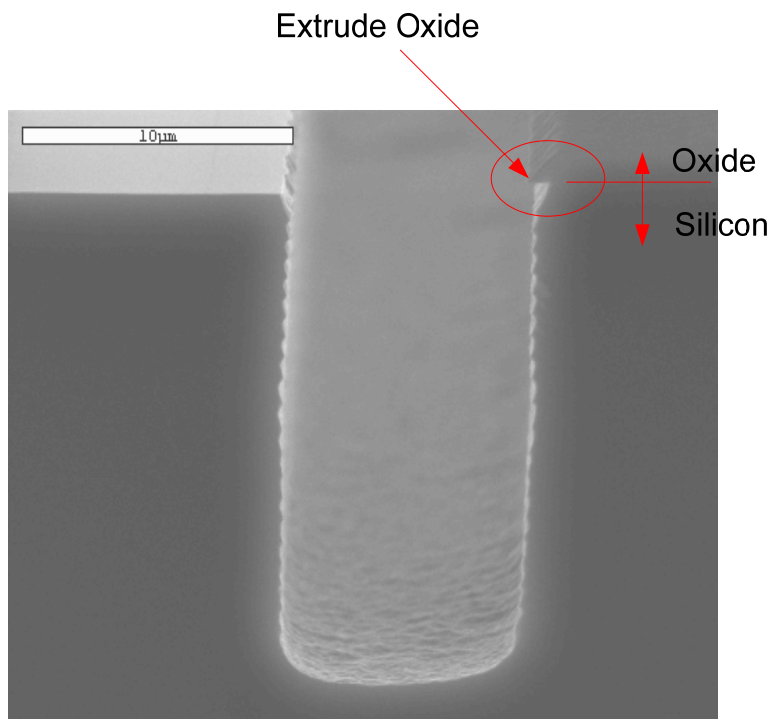


Figure 5-3. SEM side view of the notch at the interface of oxide and Si after DRIE.

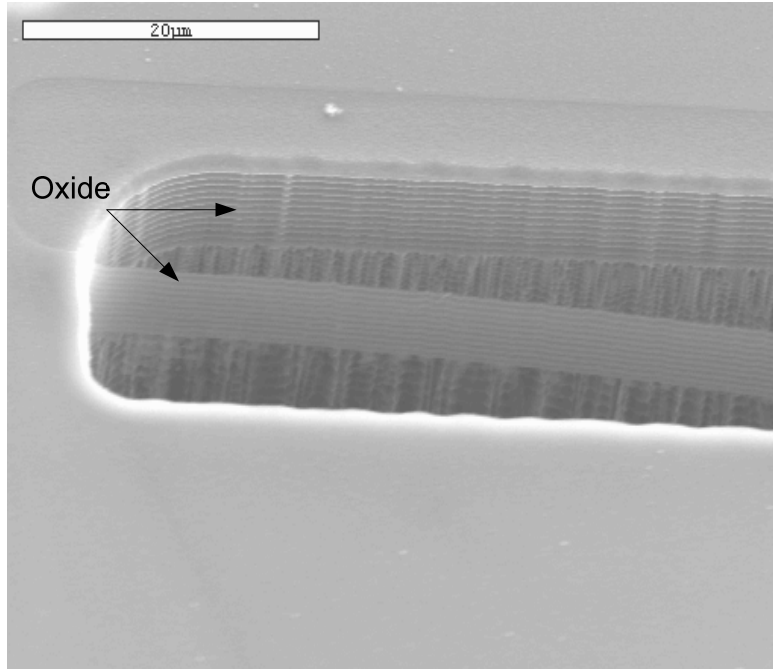


Figure 5-4. SEM top view of the trench after DRIE oxide and Si.

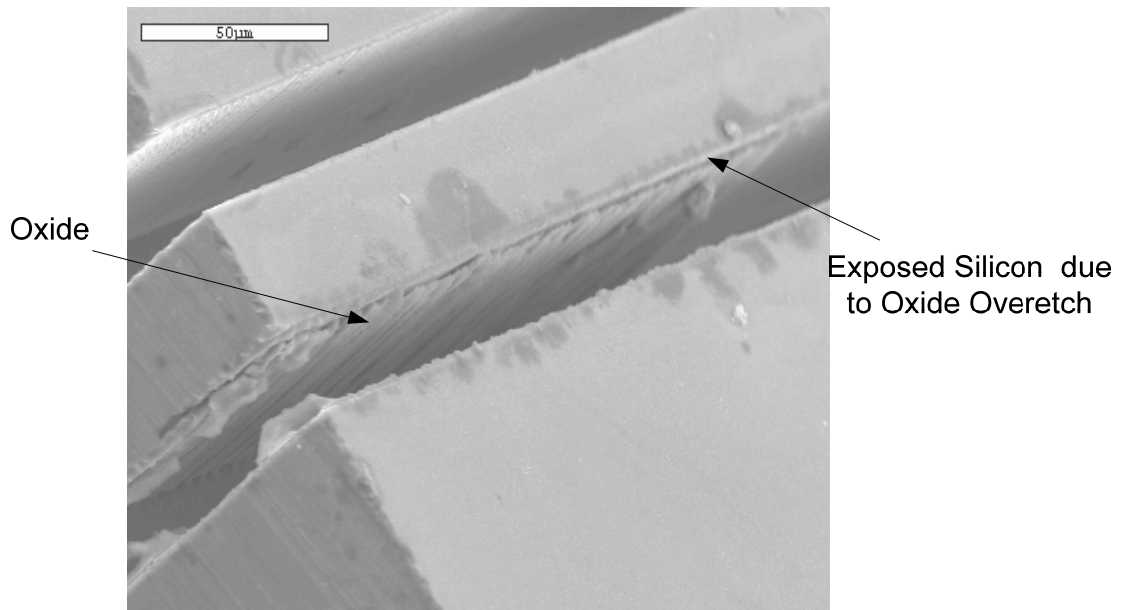


Figure 5-5. SEM top views of the trench after DRIE oxide and Si with oxide overetch.

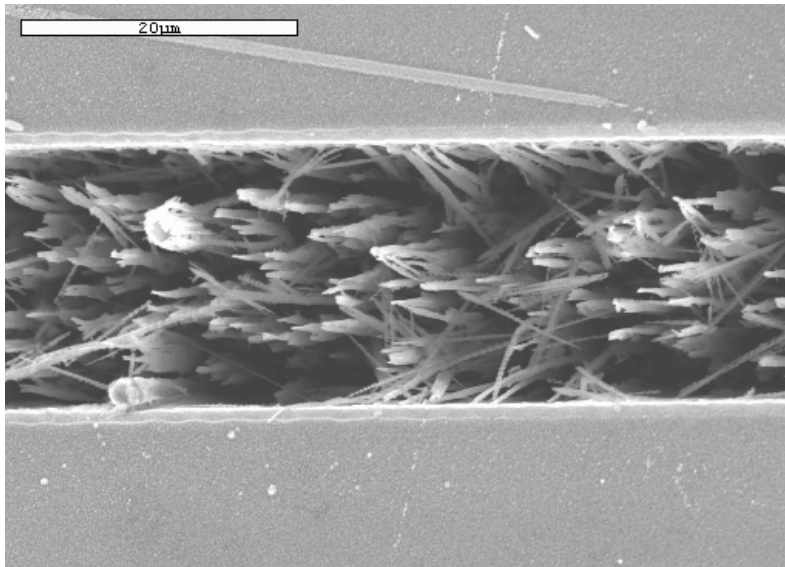


Figure 5-6. SEM top views of the trench with silicon grass through a micromasking effect due to oxide underetch.

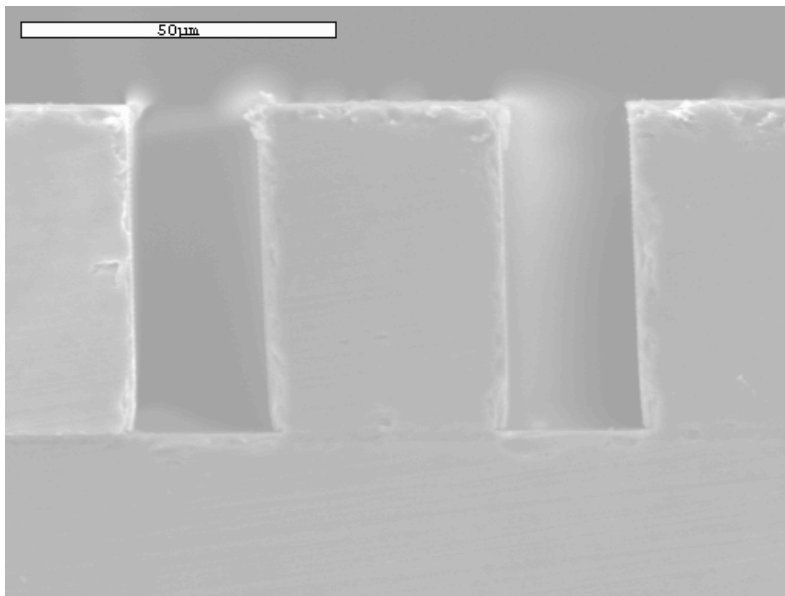


Figure 5-7. SEM side view of the trench after DRIE oxide and Si.

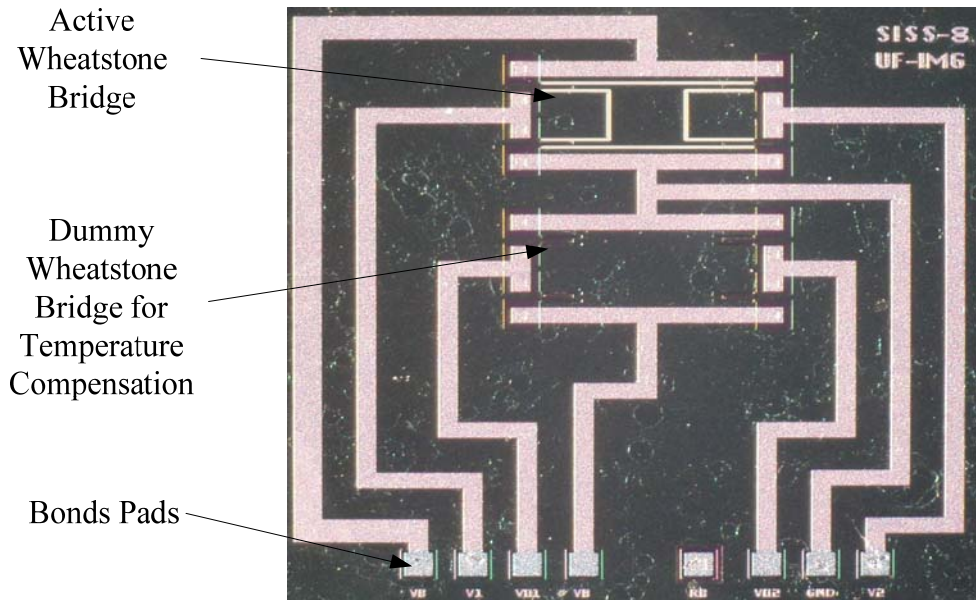


Figure 5-8. Photograph of the fabricated device.

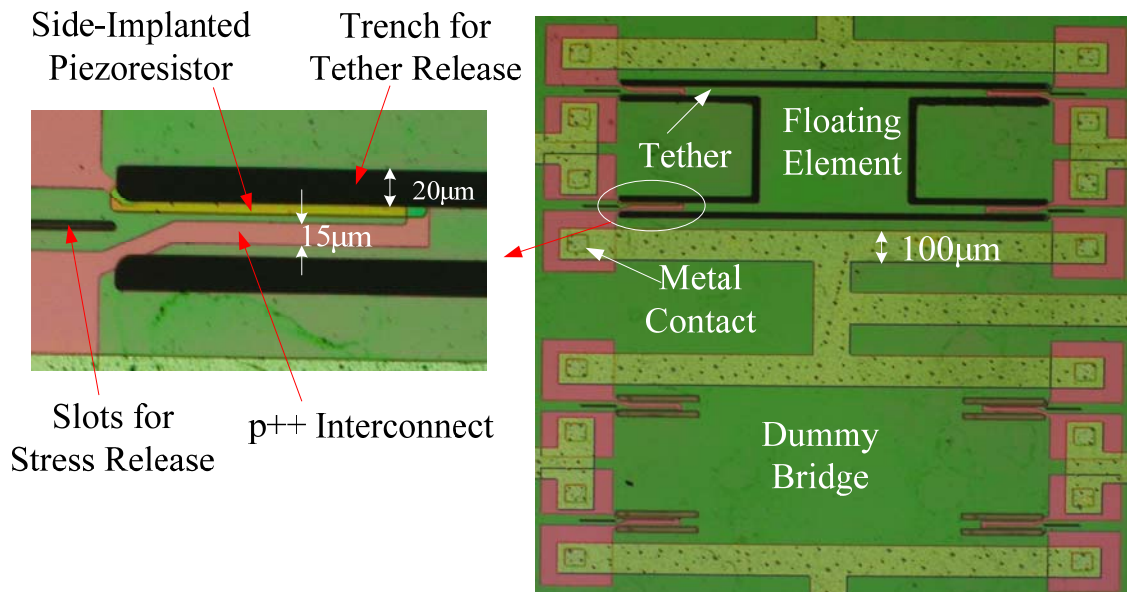


Figure 5-9. A photograph of the device with a close up view of the side-implanted piezoresistor.

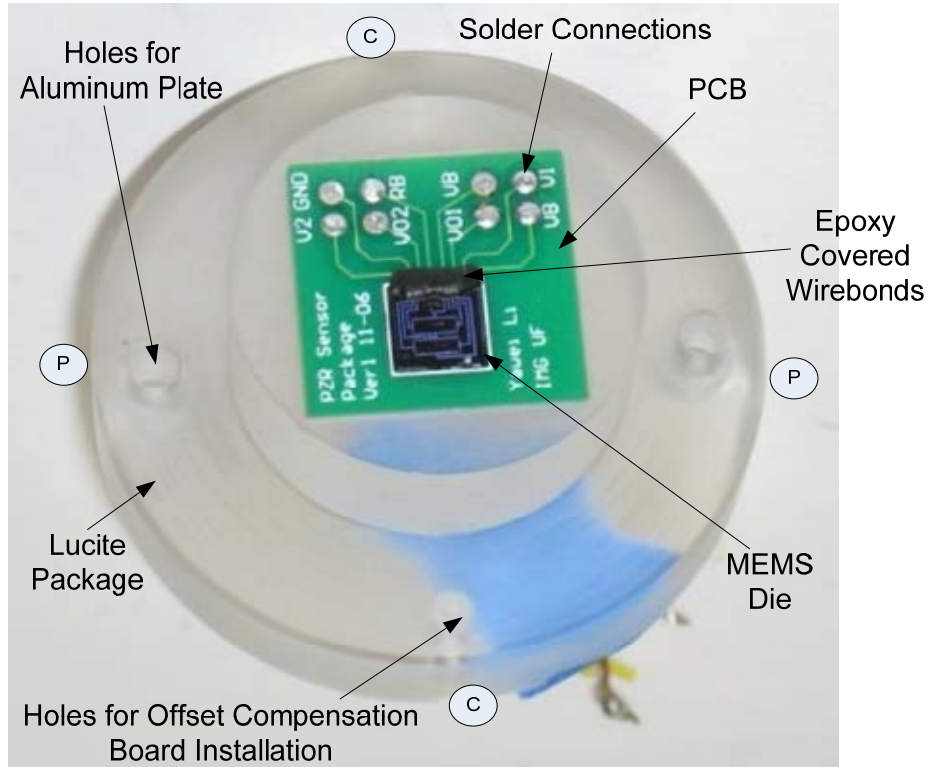


Figure 5-10. Photograph of the PCB embedded in Lucite package.

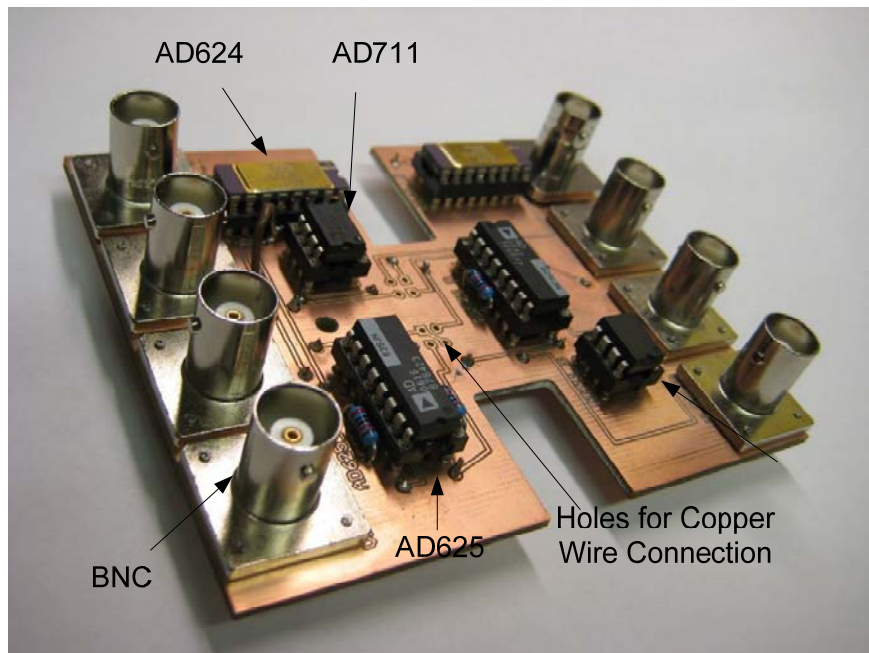


Figure 5-11. Interface circuit board for offset compensation.

CHAPTER 6 EXPERIMENTAL CHARACTERIZATION

Preliminary electrical and fluidic characterization were performed to determine the performance of the shear stress sensor and to partially compare to the analytical models discussed in Chapter 3. The experimental setup for sensor characterization is described and then the results are presented. The experiments include measurement of characteristics of p/n diode, system noise, sensor sensitivity and linearity, and frequency response.

Experimental Characterization Issues

There are two complicating issues in characterizing the sensors: the initial offset voltage output without shear stress applied and the temperature sensitivity of the bridge output. These two issues directly affect the measurement resolution and static sensitivity. Therefore, offset compensation and temperature compensation must be employed for the static calibration experiments. The motivation and methodology for offset compensation is discussed in the following paragraphs. The temperature compensation was not performed and will be discussed in Chapter 7.

For a balanced Wheatstone bridge, the differential voltage output of the sensor is directly proportional to the applied shear stress. In reality, the Wheatstone bridge is not perfectly balanced due to uncertainty in the fabrication process. As shown in Figure 6-1, the dc offset exists without applied shear stress, and is directly proportional to the bias voltage. The offset is typically $O(10 \text{ mV/V})$, or even larger in some device die. The optimization results in Chapter 4 indicate that the normalized sensitivity of the sensor designs is $O(1 \text{ } \mu\text{V/V/Pa})$. Such a small sensitivity requires high gain amplification prior to being sampled by data acquisition board. However, a dc offset will cause amplifier saturation even at a relatively low gain. Therefore, it is imperative to minimize or eliminate the offset to maximize the dynamic range of the

measurement system. An approach for the interface circuit readout is discussed as follows for dc offset compensation.

The interface circuit consists of a precision programmable instrumentation amplifier AD625 and a high speed precision Op Amp AD 711 from Analog Devices [73], as shown in Figure 6-2. The gain of the AD625 is set by adjusting external resistors R_F and R_G , and is given by $4R_F/R_G + 1$. The AD711 acts as a unity buffer. The initial offset voltage goes through the amplifier AD625 with a set gain of 21. Then the amplified offset voltage is precisely controlled by adjusting the input of the AD711, which is provided by a Stanford Research Systems SIM928 isolated voltage source [96]. SIM928 is an ultra low noise voltage source (10 μ Vrms at 1 kHz bandwidth) that provides a stable low-noise voltage reference with mV resolution. Unfortunately, there was an error in the second amplifier stage of the PCB and a decision was made to just proceed with AC shear stress calibrations to demonstrate “proof of concept” functionality.

Experimental Setup

In this section, the experimental setup for the shear stress sensor characterization is discussed. A probe station is used to measure the current-voltage (I-V) characteristics of the sensor. A plane wave tube (PWT) is then used to determine the sensor linearity, sensitivity and frequency response. Then sensor system noise is measured with dynamic calibration setup in the plane wave tube with speaker amplifier off.

Electrical Characterization

Electrical characterization includes measurement of the bridge impedance and leakage current of the junction-isolated devices, as well as the breakdown voltage. All measurements

were made using an Agilent 4155C semiconductor parameter analyzer and a wafer level probe station.

As discussed in Chapter 5, the p/n junctions are formed by the p-type piezoresistor and the p⁺⁺ interconnects with the n-well. To ensure that the current flows entirely through the p-type regions, the p/n junction must be reverse biased and the leakage current should be negligible. In this experiment, the reverse bias characteristics of the p/n junction were measured to determine the leakage current from the piezoresistors to the n-type substrate. The resistance is extracted from the I-V characteristics of the piezoresistors in the p/n forward bias region.

Dynamic Calibration

The frequency response and linearity were deduced using Stokes' layer excitation of shear-stress in a plane-wave tube (PWT). This technique utilizes acoustic plane waves in a duct to generate known oscillating wall shear stresses [97]. This technique relies on the fact that the particle velocity of the acoustic waves is zero at the wall due to the no-slip boundary condition. This leads to the generation of a frequency-dependent boundary layer thickness and a corresponding wall shear stress. Therefore, at a given location, the relationship between the fluctuating shear stress and acoustic pressure is theoretically known. The acoustically-generated wall shear stress for the frequency range of excitation in this paper is approximated by [97]

$$\tau'_{wall} = \frac{p' \sqrt{j\omega\nu}}{c} e^{j\left(\omega t - kx - \frac{\pi}{2}\right)} \tanh\left(\eta\sqrt{j}\right), \quad (6-1)$$

where p' is the amplitude of the acoustic perturbation, $j = \sqrt{-1}$, ν is the kinematic viscosity, ω is the angular frequency, $k = \omega/c$ is the acoustic wave number, $\eta = \sqrt{\omega b^2/\nu}$ is the non-dimensional Stokes number and b is the half height of the duct.

A conceptual schematic of the dynamical calibration setup is shown in Figure 6-3. The plane wave is generated by a BMS 4590P compression driver (speaker) that is mounted at one end of the PWT. The PWT consists of a rigid-wall 1”x1” duct with an anechoic termination (a 30.7” long fiberglass wedge), which is responsible for supporting acoustic plane progressive waves propagation along the duct [97]. The sensor and a reference microphone (B&K 4138) are flush-mounted at the same axial position from the driver.

The usable bandwidth for plane waves in the PWT is defined by the cut-on frequency of the first higher order mode which is 6.7 kHz in air and 20 kHz in helium. The compensated output voltage from the AD625 interface circuit is ac-coupled and amplified 46 dB by the SR560 low noise preamplifier. A B&K PULSE Multi-Analyzer System (Type 3109) is used as the microphone power supply, data acquisition unit, and signal generator for the source signal in the plane wave tube.

Noise Measurement

A noise measurement is necessary to determine the minimum detectable signal (MDS). The sensor is mounted on the sidewall of the plane wave tube and the speaker amplifier is turned off. This provides a reasonable estimate of the entire sensor system noise floor as installed in a calibration chamber. The compensated voltage output is amplified by the AD625 and the SR560 low noise preamplifier (ac coupled), and then fed into the SRS785 spectrum analyzer [98]. The spectrum analyzer measures the noise power spectral density (PSD), using a Hanning window to minimize PSD leakage. The measured noise PSD includes the sensor noise and the setup noise, including noise from sources such as EMI, the amplifier, the spectrum analyzer, and the power supply. LabVIEW is used for data acquisition and manipulation. The noise PSD is measured in three overlapping frequency spans from 10 Hz to 1024 Hz. The settings for three frequency ranges are listed in Table 6-1.

Experimental Results

Electrical Characterization

As shown in Figure 6-4, I-V characterization results indicate a negligible leakage current ($<0.12 \mu\text{A}$) up to a reverse bias voltage of -10 V . The reverse bias breakdown voltage for the P/N junction is around 20 V or greater (Figure 6-5).

I-V measurements of the diffused resistors across the Wheatstone bridge are shown in Figure 6-6 for a representative design in Table 6-2. One curve is for the resistors across the bias voltage port and ground, another is for the resistors across the output ports V_1 and V_2 . The nonlinearity of the I-V curve is obtained subtracting the actual voltage in the VB-GND curve (or V_1 - V_2) from a linear curve fit (fit between -0.5 V to 0.5 V and extended to $\pm 10 \text{ V}$), then normalizing by the linear curve and multiplying by 100. The nonlinearity is shown in Figure 6-7. The linear variation of current with voltage below 5 V (3% nonlinearity in Figure 6-7) indicates Ohmic behavior of the piezoresistors and p^{++} interconnects. The average resistances across the bridge are 397Ω and 411Ω , respectively, while the predicted value for the individual resistor is $1 \text{ k}\Omega$. The smaller than predicted resistances may be due to the high implant dosage (double of the simulation value to avoid solubility loss). The asymmetry of V_1 - V_2 curve may be due to the Schottky effect. The asymmetry may also be due to residual heating as the voltage was swept from -10 V to 10 V instead of performing two tests sweeping the voltage from 0 to 10 V and 0 to -10 V . The root cause of this asymmetry requires further study.

Dynamic Calibration Results and Discussion

The dynamic sensitivity and linearity of the sensor were tested with a single tone of 2.088 kHz as a function of increasing sound pressure levels (SPL). The chosen frequency of 2.088 kHz is far enough below the expected resonance so that it is a reasonable approximation

of the static sensitivity. In this measurement, the frequency span was 0.2-6.4 kHz with a frequency resolution of 32 Hz. 3000 linear averages with 0% overlap were taken to minimize the random error. The sensor was operated at bias voltages of 1.0 V, 1.25 V and 1.5 V. This is substantially lower than the optimized bias voltage of 10 V because electronic testing indicated nonlinearities in the current-voltage relationship at excitation voltages above 4.5 V from resistor self-heating. Any resistor self-heating will lead to temperature-resistive voltage fluctuations due to unsteady convective cooling [38]. In other words, the direct sensor will behave somewhat like an indirect sensor. To avoid this phenomenon, testing was limited to bias voltages of 1.5 V and below.

The dynamic sensitivity is the ratio of the differential sensor output voltage to the input wall shear stress. Ideally, the lateral displacement of the floating element will be solely a function of the acoustically generated wall shear stress. In practice, however, it is known that there will be an additional displacement due to the local pressure gradient forces generated by traveling acoustic waves across the floating element [43]. The magnitude of the effective shear stress including pressure-gradient effects for a purely-traveling acoustic wave in a duct is [43]

$$\tau(f)_{eff} = \left(1 + \frac{g}{2} \sqrt{\frac{2\pi f \rho}{\mu}} + t \sqrt{\frac{2\pi f \rho}{\mu}} \right) \tau_{wall} . \quad (6-2)$$

The second and third terms of Equation (6-2) represent the error due to the fluctuating flow beneath the element and the net fluctuating pressure force acting on the lip (assuming a square element). Accounting for the fact that the actual shear stress is proportional to \sqrt{f} , the magnitude of the error terms is proportional to f . The second term of Equation (6-2) assumes that $L_e \gg g$ so that the flow underneath the element can be approximated by fully-developed pressure-driven flow in a slot. For the current sensor, $g = 400 \mu\text{m}$ and $L_e = 1000 \mu\text{m}$. Clearly,

this approximation is invalid and the flow beneath the element is sufficiently complex and must be evaluated using computational techniques. Therefore, only an estimate for the pressure gradient force acting on the thickness can be provided. The maximum error for this term is 7.5 dB ($2.4\tau_{wall}$) at the highest frequency tested, 6.7 kHz. The error terms are also $\pi/2$ out of phase with the actual shear stress.

By adjusting the SPL from 123 dB to 157 dB, the induced shear stress varies from 0.04 Pa to 2.0 Pa. Figure 6-8 shows output voltages response to the shear stress variation at different bias voltages. The slopes of the plots shown in Figure 6-8 indicate the dynamic sensitivity of the sensor at different bias voltages. For all bias conditions, the sensors respond linearly up to 2.0 Pa and the sensitivities are 2.905 $\mu\text{V}/\text{Pa}$, 3.602 $\mu\text{V}/\text{Pa}$ and 4.242 $\mu\text{V}/\text{Pa}$ at bias voltages of 1.0 V, 1.25 V and 1.5 V, respectively.

The normalized sensitivity is defined as the ratio of sensitivity to applied bias voltage. For a Wheatstone bridge without resistor self-heating, the normalized sensitivity is a constant. If resistor self-heating is occurring, a power-law dependence on the power dissipation is expected. The slopes of Figure 6-9 are the normalized sensitivities at bias voltages of 1.0 V, 1.25 V and 1.5 V, respectively, which are 2.905 $\mu\text{V}/\text{V}/\text{Pa}$, 2.882 $\mu\text{V}/\text{V}/\text{Pa}$ and 2.828 $\mu\text{V}/\text{V}/\text{Pa}$. The predicted normalized sensitivity is 3.65 $\mu\text{V}/\text{V}/\text{Pa}$. Note that for Figure 6-9, the initial offset voltages were subtracted for normalized slope comparison purposes. The close match in normalized sensitivities (<3% variation) indicates that the sensor is responding solely to the piezoresistive effects and not unsteady convective cooling. This piezoresistive effect is a combination of shear stress sensitivity, pressure gradient sensitivity and normal pressure sensitivity.

The frequency response at a bias voltage of 1.5 V was also investigated in this experiment. For this test, the generator is set to a random signal with a span of 6.4 kHz and a center frequency of 3.4 kHz to ensure that all harmonics up to 6 kHz are captured. A 200 line FFT is used corresponding to frequency resolution of 32 Hz. At each measurement frequency, 2000 linear averages are taken with 0% overlap. The input shear stress is desired to be 0.3 Pa. The theoretical SPL for each measurement frequency obtained via Equation (6-1). By adjusting the SPL at specific frequency, the target shear stress is then achieved. The normalized frequency response function of the shear stress sensor is given as [43]

$$H(f) = \frac{V_{out}(f)}{\tau_{wall}(f)} \frac{\partial \bar{\tau}}{\partial \bar{V}}, \quad (6-3)$$

where $V_{out}(f)$ is the sensor output with a known input, $\tau_{wall}(f)$ is obtained via Equation (6-1), and $\partial \bar{\tau} / \partial \bar{V}$ is the flat band sensitivity. For this experiment, the sensitivity at 2.088 kHz from the linearity test was used for normalization. Figure 6-10 demonstrates the magnitude and phase of the actual frequency response function of the shear stress sensor for a nominal input shear-stress magnitude of 0.3 Pa. The gain factor is flat and is between -3.01 dB to 0.09 dB for this test. The phase is flat up to 4.552 kHz. It is noted that the gain factor at frequency of 2.088 kHz is not 0 dB, which may be due to the setup and temperature variation in these two measurements. These results are not corrected for non-idealities in the anechoic termination which results in a finite reflected wave [97]. In addition, there is some suspicion that the results above 4.552 kHz are corrupted by the scattered evanescent field near the termination. Regardless, there is no apparent resonance in this sensor up to 6.7 kHz.

To check the wave reflection effect on the measurement, the two-microphone method [99] is used to measure the reflection coefficient, as shown in Figure 6-11. The frequency spans from

0.2 Hz to 6.4 kHz . The FFT line is set to 400 giving a frequency resolution of 16 Hz . 1000 linear averages with 0% overlap are taken. The results indicated that the magnitude of the reflection coefficient is comparatively large when the frequency is below 1 kHz . Therefore, the frequency in the measurement for both linearity and frequency response are above 1 kHz to minimize the uncertainty.

The lower end of the dynamic range of the sensor is ultimately limited by the device noise floor. The output-referred noise floor of the sensor and measurement system is shown in Figure 6-12 for a bias voltage of 1.5 V . As expected, the noise spectrum is dominated by $1/f$ noise indicating that the signal-to-noise ratio for this sensor is a strong function of frequency. At 1 kHz (with 1 Hz bin) the output-referred noise floor of the sensor and measurement system is $48.2 \text{ nV}/\sqrt{\text{Hz}}$ which corresponds to the minimum detectable shear stress of 11.4 mPa .

Summary

Preliminary electrical and dynamic characterization and the noise determination are presented to demonstrate device functionality. At a bias voltage of 1.5 V , the dynamic characterization of the device revealed a linear response up to at least 2.0 Pa and a flat response up to the frequency testing limit of 6.7 kHz . The theoretically predicted resonant frequency is 9.8 kHz . Noise floor measurements indicate that $1/f$ noise dominates and the minimum detectable shear stress at 1 kHz is 11.4 mPa . Therefore, the experimentally verified dynamic range is 11 mPa-2 Pa . The theoretically predicted upper end of the dynamic range at 3% static non-linearity is 5 Pa. The upper ends of the dynamic range and bandwidth, however, could not be verified due to constraints in the calibration apparatus. A summary of the experimental results compared to the predicted results for a bias voltage of 1.5 V are listed in Table 6-4. The normalized sensitivity is close to the predicted design value, but resistor heating precluded using

higher bias voltages, thus lowering the maximum allowable sensitivity by 16.5 dB.

Furthermore, the noise floor is roughly a factor of 7 higher than predicted. This may be due to the noise floor measured is the total system noise, which includes setup noise and sensor noise, whereas the predicted value is just due to the sensor and the AD 625 circuit. There are also substantial differences in the predicted versus realized bridge impedance which means that the voltage noise of the resistors may also be higher than predicted.

Table 6-1. LabVIEW settings for noise PSD measurement

Frequency Range (Hz)	Bin Width (Hz)	Number of Averages
10-200	0.25	2300
200-1600	2	4000
1600-102400	128	30000

Table 6-2. The optimal geometry of the shear stress sensor that was characterized.

Parameters	Design Values
Target Shear Stress τ_{\max} (Pa)	5
Tether Length L_t (μm)	1000
Tether Width W_t (μm)	30
Tether Thickness T_t (μm)	50
Floating Element Width W_e (μm)	1000
Piezoresistor Length L_r (μm)	228.5
Piezoresistor Width W_r (μm)	5
Piezoresistor Depth y_j (μm)	1

Table 6-3. Sensitivity at different bias voltage for the tested sensor.

Bias Voltage (V)	Sensitivity (mV/Pa)
1.5	0.27
2.95	0.71
3.1	0.93
4.8	3.0

Table 6-4. A comparison of the predicted versus realized performance of the sensor under test for a bias voltage of 1.5V.

Parameters	Theoretical Value	Experimental Result
Normalized Sensitivity ($\mu\text{V}/\text{V}/\text{Pa}$)	3.65	2.83
Noise Floor (nV)	6.5	48.2
MDS (mPa)	1.2	11.4
Bandwidth (kHz)	9.8	>6.7
Resistance (Ω)	1000	397
τ_{\max} (Pa)	5	>2

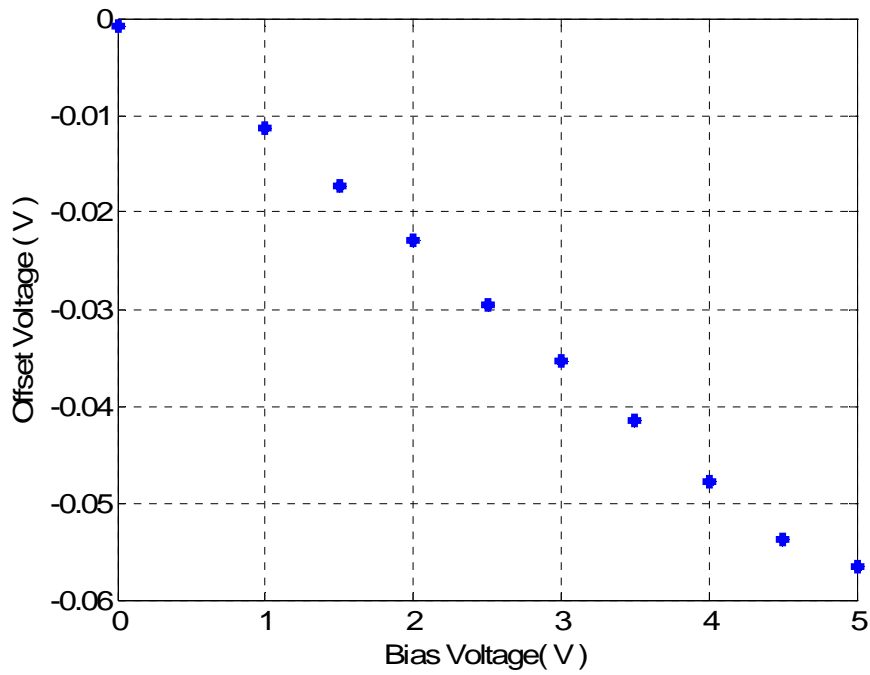


Figure 6-1. The bridge dc offset voltage as a function of bias voltages for the tested sensor.

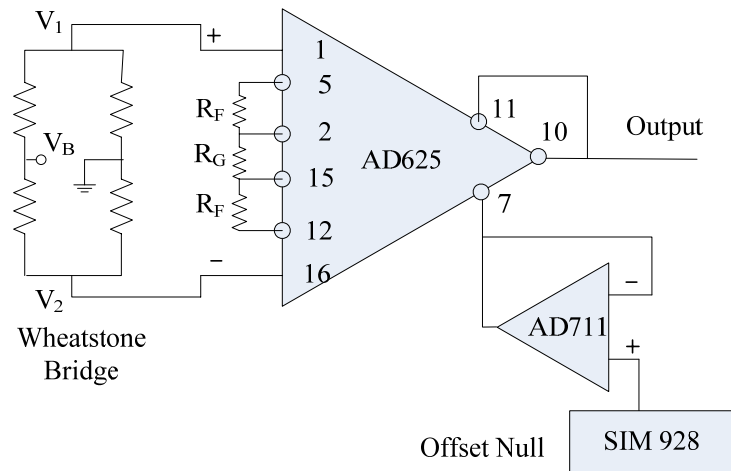


Figure 6-2. An electrical schematic of the interface circuit for offset compensation.

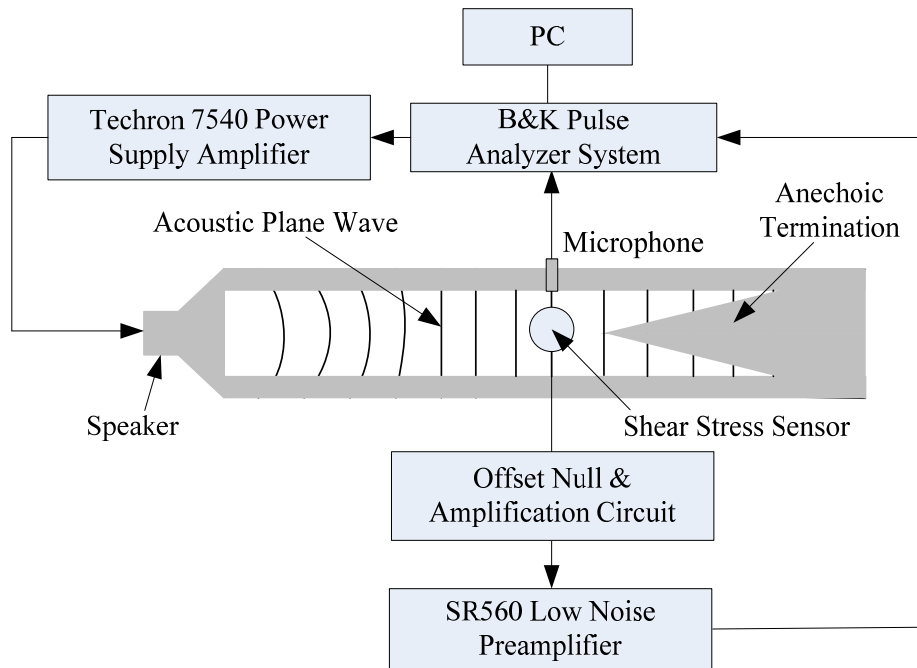


Figure 6-3. A schematic of the experimental setup for the dynamic calibration experiments.

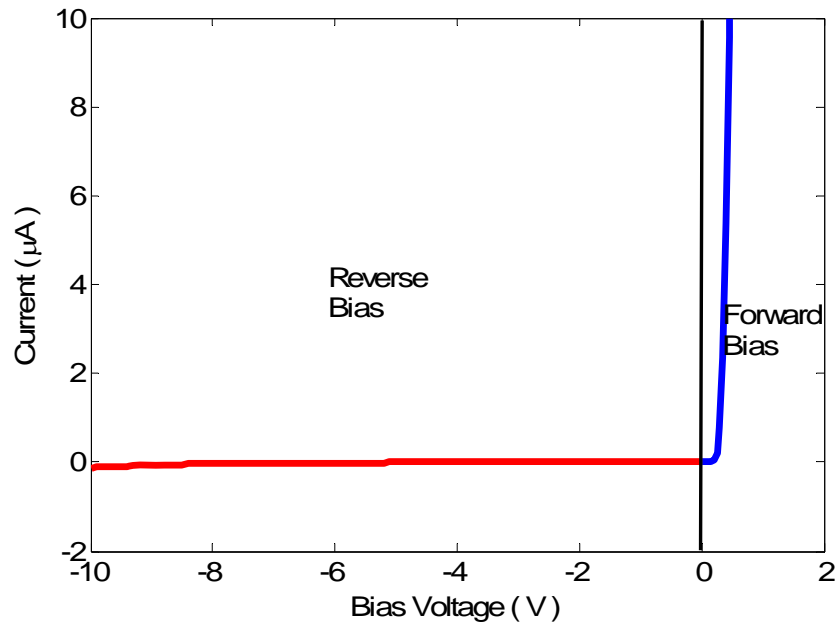


Figure 6-4. Forward and reverse bias characteristics of the p/n junction.

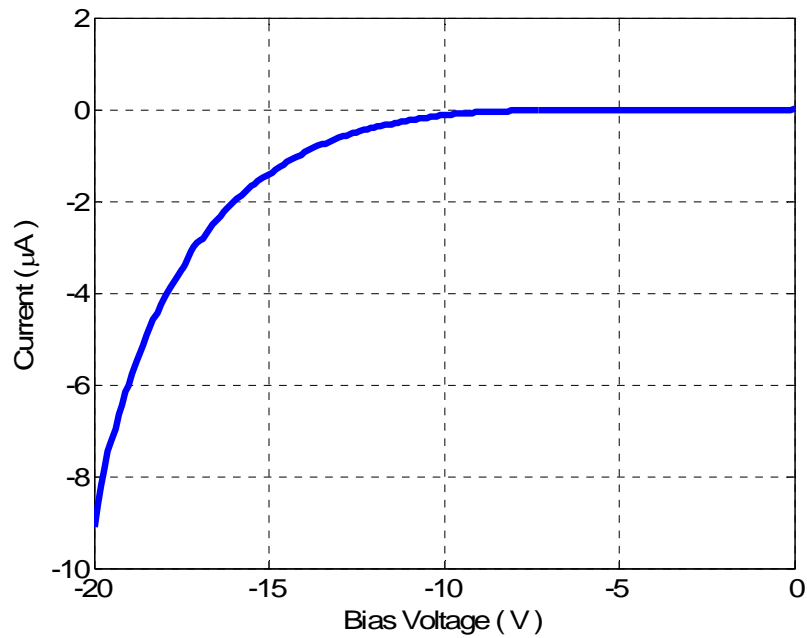


Figure 6-5. Reverse bias breakdown voltage of the P/N junction.

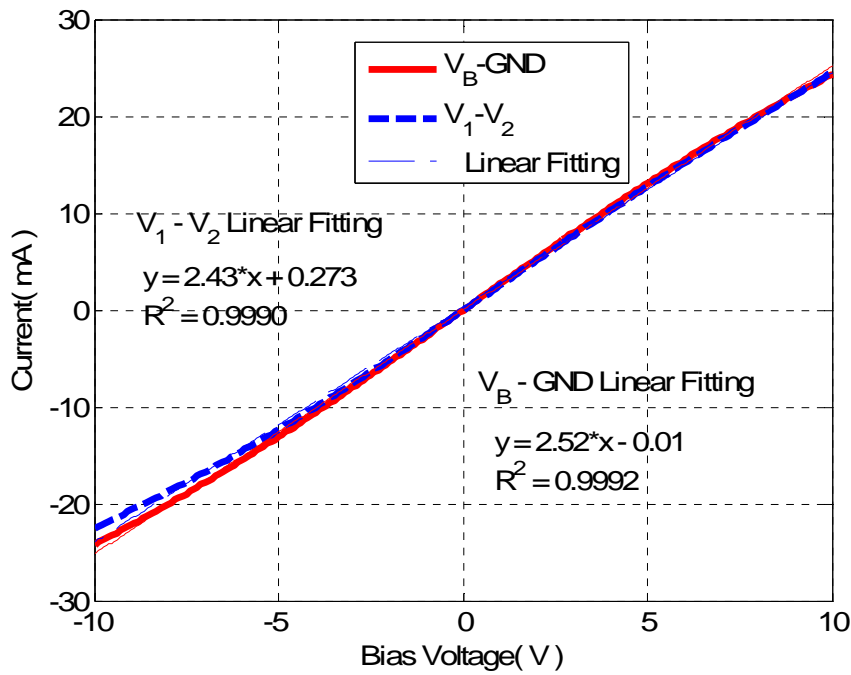


Figure 6-6. I-V characteristics of the input and output terminals of the Wheatstone bridge.

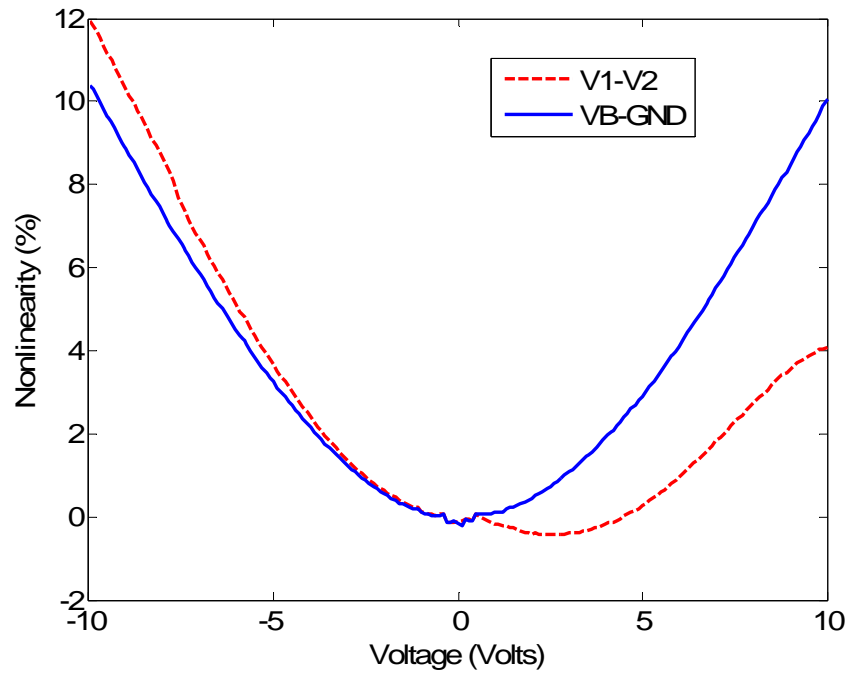


Figure 6-7. The nonlinearity of the I-V curve in Figure 6-6 at different sweeping voltages.

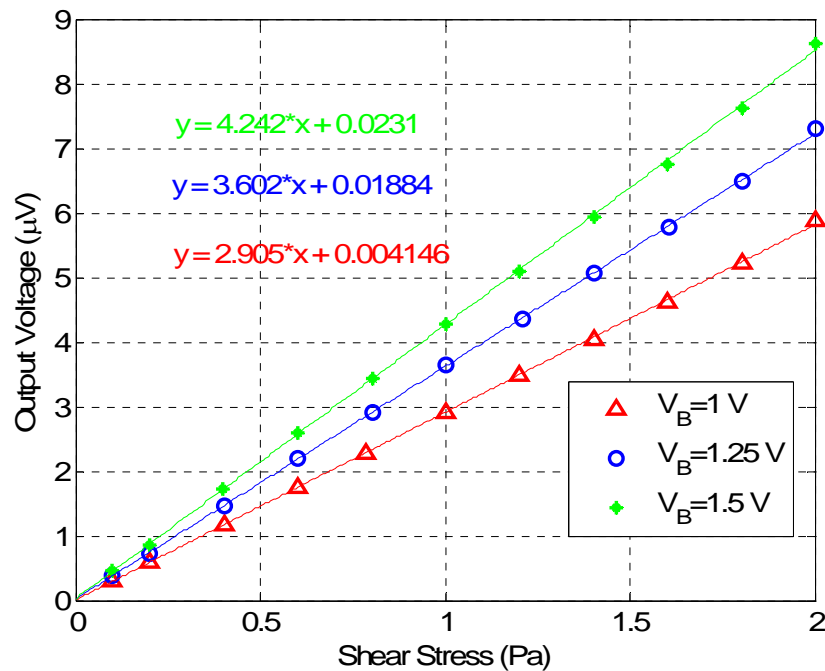


Figure 6-8. The output voltage as a function of shear stress magnitude of the sensor at a forcing frequency of 2.088 kHz as a function bias voltage.

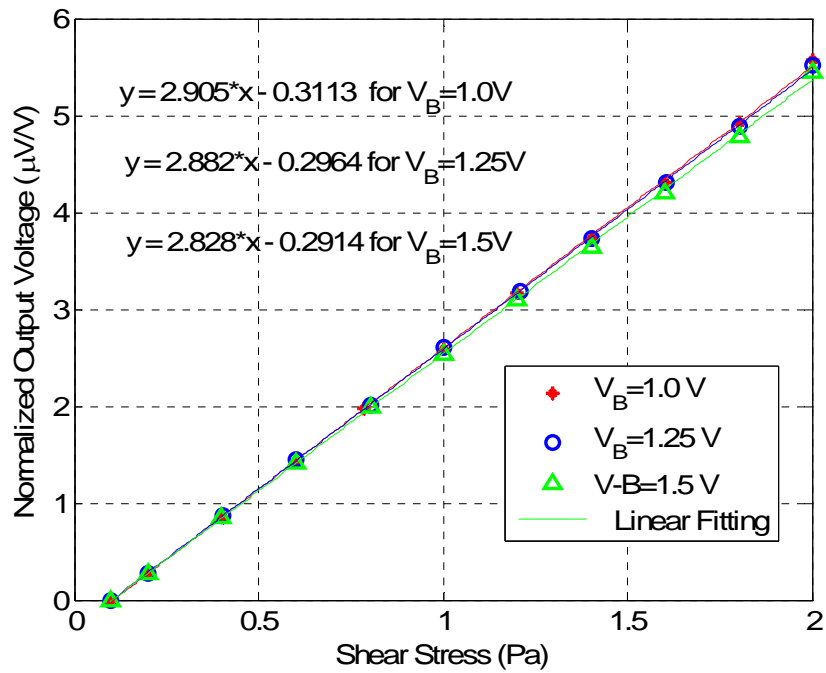


Figure 6-9. The normalized output voltage as a function of shear stress magnitude of the sensor at a forcing frequency of 2.088 kHz for several bias voltages.

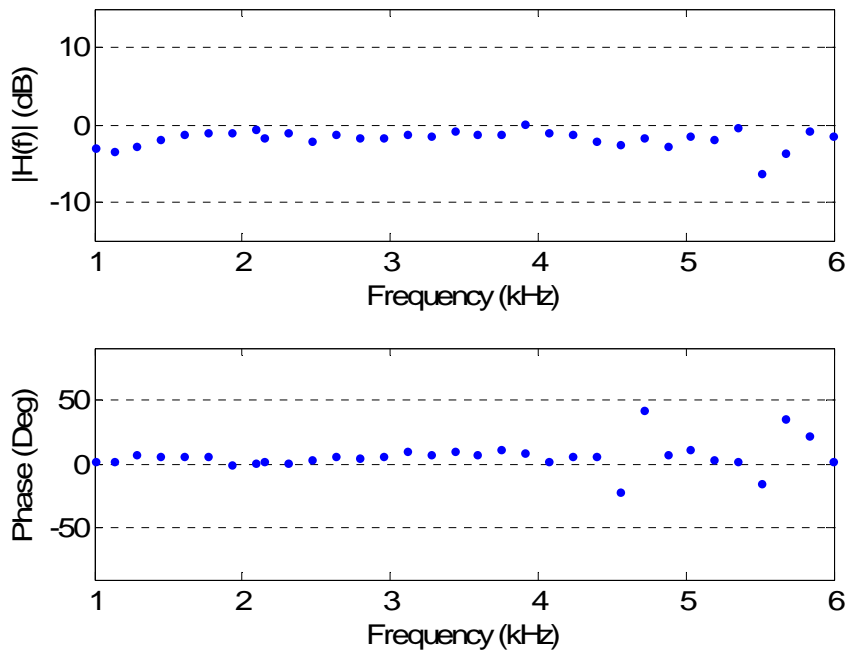


Figure 6-10. Gain and phase factors of the frequency response function.

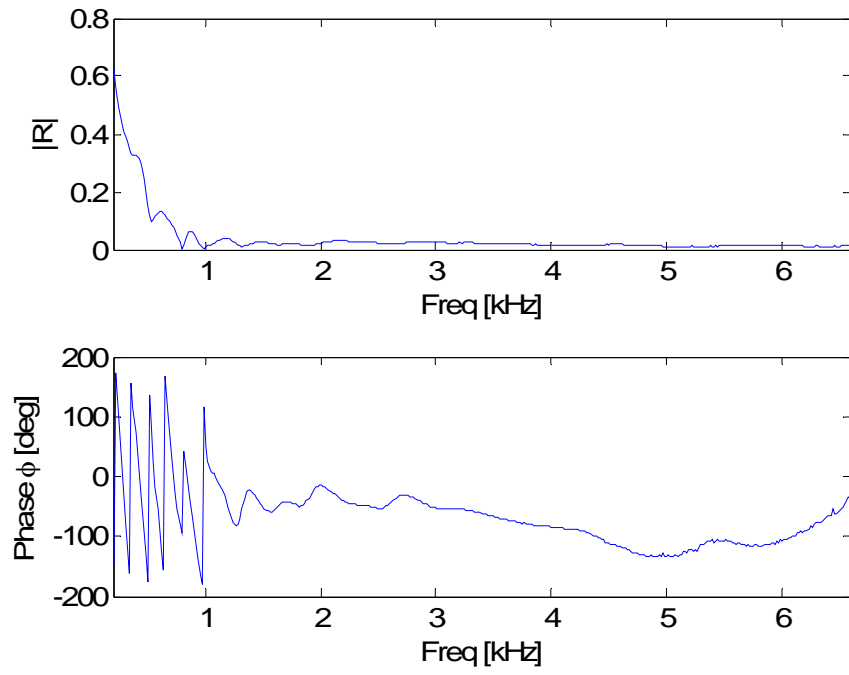


Figure 6-11. The magnitude and phase angle of the reflection coefficient of the plane wave tube.

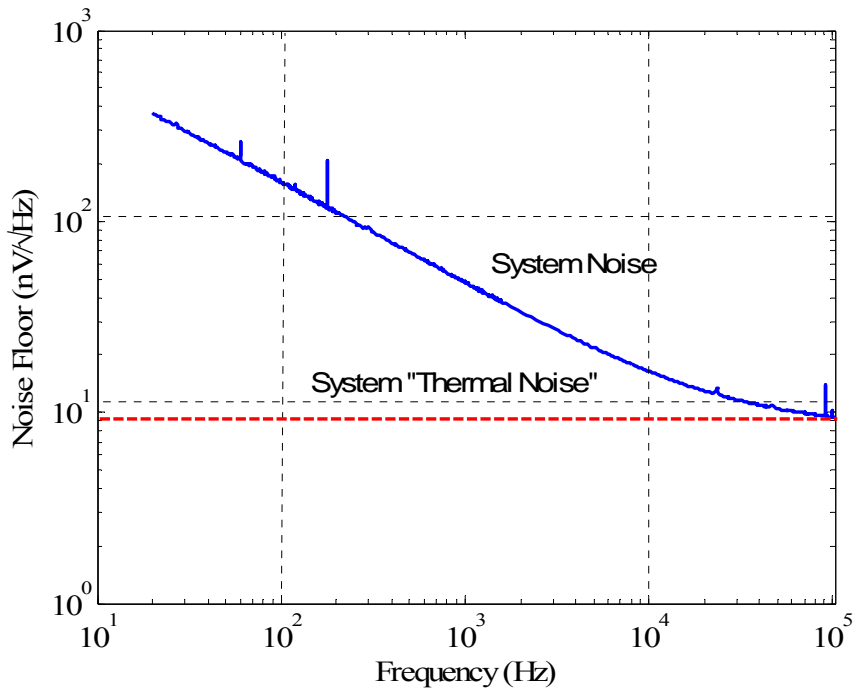


Figure 6-12. Output-referred noise floor of the measurement system at a bias voltage of 1.5V.

CHAPTER 7 CONCLUSION AND FUTURE WORK

Summary and Conclusions

A proof-of-concept micromachined, floating element shear-stress sensor was developed that employs laterally-implanted piezoresistors for the direct measurement of fluctuating wall shear stress. The shear force on the element induces a mechanical stress field in the tethers and thus a resistance change. The piezoresistors are arranged in a fully-active Wheatstone bridge to provide rejection to common mode disturbances, such as pressure fluctuations. A dummy bridge located next to the sensor is used for temperature corrections. The device modeling, optimal design, fabrication process, packaging and comprehensive calibration were presented.

Mechanical models for small and large deflection of the floating element have been developed. These models are combined with a piezoresistive model to determine the sensitivity. The dynamic response of the shear stress sensor was explored by combining the above fundamental mechanical analysis with a lumped-element model. Finite element analysis is employed to verify the mechanical models and lumped-element model results. Dominant electrical noise sources in the piezoresistive shear stress sensor, $1/f$ noise and thermal noise, together with amplifier noise, are considered to determine the noise floor. These models are then leveraged to obtain optimal sensor designs for measuring shear stress in several flow regimes.

The cost function, minimum detectable signal (MDS) formulated in terms of sensitivity and noise floor, is minimized subject to nonlinear constraints on geometric dimensions, linearity, bandwidth, power, resistance, and manufacturing constraints. The optimization results indicate that the predicted optimal device performance is improved with respect to existing shear stress sensors, with a MDS of $O(0.1 \text{ mPa})$ and dynamic range greater than 75 dB. A sensitivity

analysis indicates that the device performance is most responsive to variations in tether geometry.

The process flow used an 8-mask bulk micromachining process, involving PECVD, thermal oxidation, wet etch, sputtering, DRIE and RIE fabrication techniques. After fabrication, the die was packaged for wind tunnel testing in a custom printed circuit board for modularity. An interface circuit board was designed for amplification and offset compensation.

Then the sensor was calibrated electrically and dynamically. Electrical characterization indicates linear junction-isolated resistors, and a negligible leakage current ($<0.12 \mu\text{A}$) for the junction-isolated diffused piezoresistors up to a reverse bias voltage of -10 V . Using a known acoustically-excited wall shear stress for calibration at a bias voltage of 1.5 V , the sensor exhibited a sensitivity of $4.24 \mu\text{V}/\text{Pa}$, a noise floor of $11.4 \text{ mPa}/\sqrt{\text{Hz}}$ at 1 kHz , a linear response up to the maximum testing range of 2 Pa , and a flat dynamic response up to the testing limit of 6.7 kHz . These results coupled with a wind-tunnel suitable package are a significant first step towards the development of an instrument for turbulence measurements in low-speed flows. The system noise is $48.2 \text{ nV}/\sqrt{\text{Hz}}$ at 1 kHz (with 1 Hz bin), and is roughly 7 times higher than predicted. Static heating limitations limited the maximum bias voltage to 1.5 V instead of 10 V .

Suggestions for Future Work

Future work should focus on the comprehensive characterization of the sensor to determine absolute performance and to compare against all of the theoretical predictions. An uncertainty analysis of all experiments and accurate measurement of the sensor geometry are required to enable this comparison. Specifically, a temperature compensation approach must be realized that will enable the static calibration of the sensor as well as any dc measurement application. The

resonant frequency of the sensors must be determined. Sensitivity to vibration and pressure fluctuations must also be determined. Detailed noise measurements that isolate the contribution from the piezoresistor should be carried out. Finally, the flow around the floating element will be investigated via numerical simulations to provide an improved estimate of pressure gradient induced errors. In the following subsection, several suggestions for carrying out these measurements are discussed below.

Temperature Compensation

The sensitivity of the shear stress sensor changes with temperature due to the variation of the piezoresistive coefficient with temperature, as indicated in Equation (3-23) and (3-24). In sensor static calibration in a 2-D laminar cell, the sensitivity is defined as the slope of the curve of voltage output versus shear stress. However, due to the temperature effect, the output voltage is a function of shear stress and temperature. Thus the temperature induced voltage output should be subtracted from the active bridge voltage output. For the identical active and dummy Wheatstone bridge, the temperature effect on them should be same. Therefore, the temperature effect on the active bridge in the static calibration can be removed by subtracting the voltage output of the dummy bridge.

Unfortunately, the active bridge and dummy bridge are not identical due to Wheatstone mismatch. So the voltage output dependence of the temperature need to be measured for both active bridge and dummy bridge. The output voltage of the active bridge is a function of shear stress and temperature variations, while the dummy bridge depends on temperature variation only. The measured output voltages in the laminar flow are $V_a(\tau_w, T)$ for the active bridge and $V_d(T)$ for the dummy bridge, respectively. The slope of the voltage vs. temperature curve is S_{T_a}

for active bridge and S_{Td} for dummy bridge. In the static calibration, the output voltage dependence of shear stress is given as

$$V_a(\tau_w) = V_a(\tau_w, T) - V_a(T). \quad (7-1)$$

Assuming that the slope of the V_o vs. T curve remains constant and they are given as,

$$\frac{V_a(T) - V_a(T_0)}{V_d(T) - V_d(T_0)} = \frac{S_{Ta}}{S_{Td}}. \quad (7-2)$$

Substituting $V_a(T)$ from Equation (7-1) into (7-2) and rearranging it, the shear stress dependent output voltage is obtained as

$$V_a(\tau_w) = (V_a(\tau_w, T) - V_a(T_0)) - \frac{S_{Ta}}{S_{Td}}(V_d(T) - V_d(T_0)), \quad (7-3)$$

where $V_a(T_0)$ is the initial voltage value at room temperature. The Equation (7-3) indicates that S_{Ta} and S_{Td} must be obtained in order to get $V_a(\tau_w)$. Preliminary experiments prior to employing dc offset nulling were performed to determine the temperature sensitivity. Unfortunately, the large dc offset limited the quality of the results. The experimental set up is as follows.

The voltage output dependence of temperature variation is conducted in two bath settings. Both bathes are filled with DI water. The outer bath is the chamber of Isotemp refrigerated circulator, and the inner bath is glass beaker. The packaged sensor is sitting on the top of the beaker. The beaker is used to protect the sensor from flow circulation disturbance. The compensated voltage output is connected to a HP34970A data acquisition unit and DAQ card. A HP34970A digital voltage meter is used to minimize the 60 Hz noise. LabVIEW is used for data acquisition.

Static Characterization

Initially, we attempted to statically characterize the sensor, but the temperature sensitivity and dc offset issues prevented any meaningful results. The goal of the static characterization is to verify the sensor design and characterize the sensitivity and linearity. After temperature compensation and dc nulling have been achieved, a static calibration can be performed. The flow cell design is such that an ideal one-dimensional fully developed incompressible laminar flow exists between two semi-infinite parallel plates (Poiseuille flow between two parallel plates). For this case, the pressure drop is constant and the wall shear stress is given by the theoretical relation [7]

$$\tau_w = -\frac{h}{2} \frac{dP}{dx}, \quad (7-4)$$

where h is the height of the channel in meters and P is pressure in Pascals. Detailed setup information can be found in [34].

The incompressible flow is first verified before the sensor static calibration. The incompressible flow exhibits a linear pressure drop versus length for wall shear stress up to 2 Pa, which is a necessary assumption for Equation (7-4). The pressure measurements are carried out using the Scannivalve pressure measurement system. This multiplexing valve system allows the pressure taps to be reached sequentially to measure pressure drop between the first pressure tap and other taps downstream. The inlet flow rate is regulated using a mass flow controller (GFC4715). A linear pressure drop versus length is displayed in Figure 7-1.

Figure 7-2 shows the experimental setup for the static calibration of the wall shear stress sensor. The sensor is flush-mounted on one wall of the laminar flow cell and oriented for measuring wall shear stress in the flow direction. The corresponding pressure drops across two pressure taps P_1 and P_2 is measured using a differential pressure gauge, Heise pressure meter.

The voltage output is first fed into the compensation circuit. The compensated signal is then supplied to a HP34970A precision digital voltage meter to eliminate 60Hz noise from the power supply by averaging. The mass flow rates are controlled automatically by LabVIEW to obtain different pressure drops and correspondingly wall shear stress. LabVIEW is also used for data acquisition and manipulation.

Noise Measurement

In order to determine the isolated resistor noise characteristics, the sensor is placed in a double-nested Faraday Cages to improve the electromagnetic interference (EMI) reduction [98]. The compensated voltage output is amplified by a SR560 preamplifier, and then fed into the spectrum analyzer (SRS785). The spectrum analyzer (ac coupled) measures the noise power spectral density (PSD), using a Hanning window to avoid PSD leakage. The noise PSD of the sensor is obtained by subtracting the setup noise PSD from the total measurement noise PSD. The setup noise sources include EMI and noise from the amplifier, spectra analyzer, and power source.

Recommendations for Future Sensor Designs

Based on lessons learned during the first generation shear stress sensor fabrication and characterization, there are several issues that need to be addressed in future designs. Specifically, issues regarding resistor self-heating and pressure sensitivity need to be addressed.

In the sensor calibration, piezoresistor self-heating was clearly present when the dissipated power was greater than 10 mW . A study of the normalized sensitivities indicated that self-heating could be avoided all together for a power dissipation limit of 5.7 mW . Therefore, the power dissipation limit in the design optimization should be decreased from 100 mW down to 10 mW to avoid resistor self heating. The power limit will be a function of the tether geometry, but the order of magnitude in power reduction will provide a better estimate of appropriate

biasing conditions for design purposes. A detailed numerical study of the resistor heating may also provide insight into this phenomenon, but this may be challenging due to the complexity of the convective boundary conditions at the tether surface.

For a balanced Wheatstone bridge, pressure fluctuations should not affect the voltage output. Preliminary pressure calibrations, however, indicate that the pressure sensitivity is only $O(10 \text{ dB})$ lower than the shear stress sensitivity. In addition to achieving better control of the resistor implant process to balance the bridge, this can be mitigated by extending the side-implanted resistor all the way down tether thickness. The fabrication process should change correspondingly to protect the bottom of the piezoresistor with a high quality passivation. In current sensor design, the piezoresistor is implanted on the top $5 \mu\text{m}$ of the tether thickness to avoid resistor current leakage. So in the final backside release step, the BOX layer was removed to release the structure and the tether bottom is exposed to the flow without any protection. This will cause sensitivity drifting if the piezoresistor is implanted on the whole tether thickness. A process flow must be designed to realize an electrically passivated resistor that extends to the bottom of the resistor thickness.

In general, improved test structures are needed to provide additional information about the side-planted resistors. Specifically, a test structure must be added into the mask design to enable the measurement resistor doping profile via secondary ion mass spectroscopy (SIMS). In addition, providing additional bond pads for each resistor will permit a resistor trim based approach to bridge balancing and temperature compensation [60].

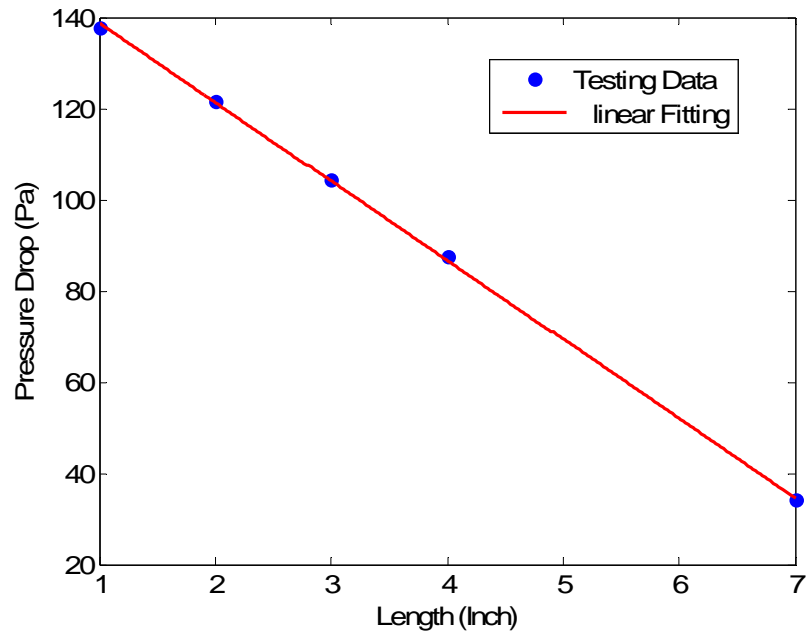


Figure 7-1. Pressure drops versus length between taps in the flow cell.

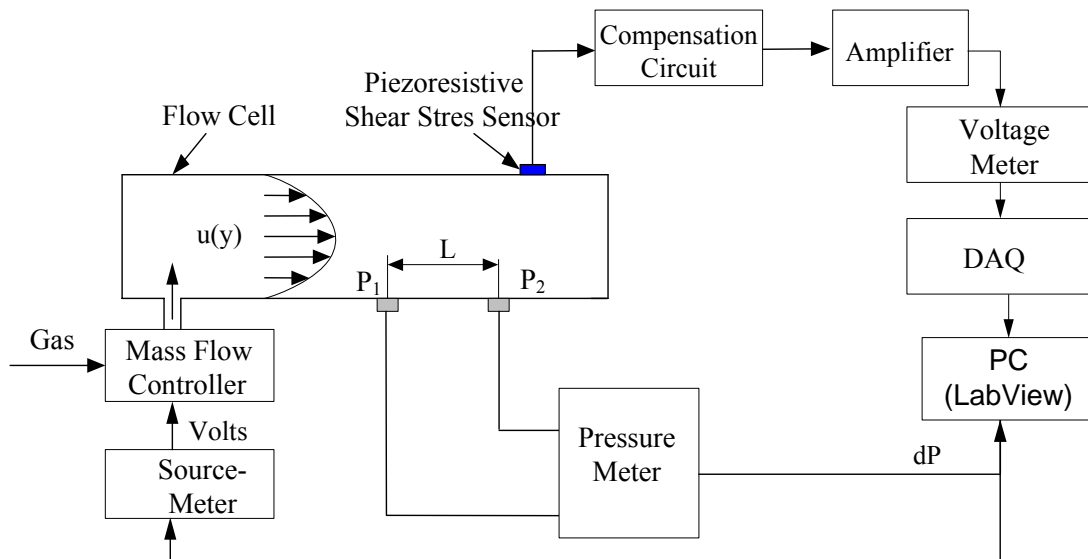


Figure 7-2. Experimental setup of static calibration.

APPENDIX A MECHANICAL ANALYSIS

A clamped-clamped beam with a central point force and a distributed pressure load is shown in Figure A-1 (a). This is a second order statically indeterminate problem. Euler Bernoulli beam theory is used to predict the linear, small deflection behavior and Von Kármán strain is included in the nonlinear, large deflection models. Two methods, an energy method and an exact analytical method, are used to solve the large deflection problem. Using Euler-Bernoulli beam theory, the stress distribution is also derived.

Small Deflection

Equilibrium equations may be written based on the free body diagram of the symmetric structure, Figure A-1(b). The relationships between the resultant forces, R_A and R_B , point load P , and distributed load Q are thus

$$R_A = R_B = P/2 + QL_t, \quad (\text{A-1})$$

where $P = \tau_w W_e L_e / 2$, $Q = \tau_w W_t$, and τ_w is the wall shear stress. The nonlinear differential equation governing the beam deflection caused by bending is given as [82]

$$EI \frac{d^2 w(x)/dx^2}{\left[1 + (dw/dx)^2\right]^{3/2}} = M_x, \quad (\text{A-2})$$

where $w(x)$ is the deflection in the z direction, E is the Young's Modulus, I is the area moment of inertia given as $I = T_t W_t^3 / 12$, and M_x is the resisting moment in cross of x . Writing the equation for moment equilibrium, $\sum M_D = 0$, yields

$$M_x = -M_A + R_A x - Qx^2/2, \quad (\text{A-3})$$

where M_A is the resisting moment, and $M_A = M_B$ due to the symmetry of the structure.

Assuming the rotation dw/dx is very small, Equation (A-2) is simplified to

$$\frac{d^2w(x)}{dx^2} = \frac{M_x}{EI}. \quad (\text{A-4})$$

Integrating Equation (A-4) yields the rotation and deflection of the beam along its length,

$$\frac{dw(x)}{dx} = \frac{1}{EI} \left(-M_A x + \frac{1}{2} R_A x^2 - \frac{1}{6} Q x^3 \right) + c_1 \quad (\text{A-5})$$

and

$$w(x) = \frac{1}{EI} \left(-\frac{M_A x^2}{2} + \frac{1}{6} R_A x^3 - \frac{1}{24} Q x^4 \right) + c_1 x + c_2, \quad (\text{A-6})$$

where c_1 and c_2 are constants. There are three unknown quantities in Equations (A-5) and (A-6)

, M_A, c_1 and c_2 . Therefore, three boundary conditions should be employed,

$$w(0) = 0 \quad (\text{clamped}), \quad (\text{A-7})$$

$$\frac{dw(0)}{dx} = 0 \quad (\text{clamped}), \quad (\text{A-8})$$

and

$$\frac{dw(L_t)}{dx} = 0 \quad (\text{symmetry}). \quad (\text{A-9})$$

Substituting the above boundary conditions and R_A from (A-1) into (A-6), one obtains

$$c_1 = c_2 = 0, \quad (\text{A-10})$$

and

$$M_A = \frac{1}{4} P L_t + \frac{1}{3} Q L_t^2. \quad (\text{A-11})$$

The displacement $w(x)$ is then obtained by substituting Equation(A-10)-(A-11) and momentum of inertia $I = T_t W_t^3 / 12$ into (A-6)

$$w(x) = \frac{-\tau_w}{4E W_t^3 T_t} \left[(3W_e L_e L_t + 8W_t L_t^2) x^2 - (2W_e L_e + 8W_t L_t) x^3 + 2W_t x^4 \right], \quad (0 \leq x \leq L_t). \quad (\text{A-12})$$

The maximum deflection at the center of the beam is given as

$$\Delta_L = -w(L_t) = \frac{\tau_w W_e L_e}{4ET_t} \left(\frac{L_t}{W_t} \right)^3 \left(1 + \frac{2W_t L_t}{W_e L_e} \right). \quad (\text{A-13})$$

Large Deflection-Energy Method

In a large lateral deflection, the beam experiences bending and stretching. The total strain is composed of bending and stretching strain [42]

$$\varepsilon_t = \varepsilon_{bending} + \varepsilon_{stretching}, \quad (\text{A-14})$$

where $\varepsilon_{bending} = y \frac{d^2 w}{dx^2}$, y is the position upward. The axial strain at $y = W_t/2$ is given as [100]

$$\varepsilon_a = \frac{du}{dx} + \frac{1}{2} \left(\frac{dw}{dx} \right)^2. \quad (\text{A-15})$$

The total change in beam length is given by

$$\delta L = \int_0^{2L_t} \varepsilon_a dx = \int_0^{2L_t} \left(\frac{du}{dx} + \frac{1}{2} \left(\frac{dw}{dx} \right)^2 \right) dx. \quad (\text{A-16})$$

The integration of the first term is zero due to the clamped-clamped boundary condition. The axial strain is the total change in beam length divided by the total length of the beam

$$\varepsilon_{stretching} = \frac{\delta L}{2L_t} = \frac{1}{4L_t} \int_0^{2L_t} \left(\frac{dw}{dx} \right)^2 dx. \quad (\text{A-17})$$

The total strain is obtained as

$$\varepsilon_t = y \frac{d^2 w}{dx^2} + \frac{1}{4L_t} \int_0^{2L_t} \left(\frac{dw}{dx} \right)^2 dx. \quad (\text{A-18})$$

For large deflection, a trial function in the form of a cosine is assumed, as it automatically satisfies the doubly clamped boundary condition and is a maximum at the center of the beam.

The trial function is thus

$$w(x) = \frac{\Delta_{NL}}{2} \left[1 + \cos\left(\frac{\pi(L_t - x)}{L_t}\right) \right], \quad (\text{A-19})$$

where Δ_{NL} is the maximum deflection at the center of the beam. Substituting this model into (A-18) yields

$$\frac{dw}{dx} = \frac{\Delta_{NL}\pi}{2L_t} \sin\left(\frac{\pi(L_t - x)}{L_t}\right) \quad (\text{A-20})$$

and

$$\frac{d^2w}{dx^2} = -\frac{\Delta_{NL}\pi^2}{2L_t^2} \cos\left(\frac{\pi(L_t - x)}{L_t}\right). \quad (\text{A-21})$$

Substituting Equation (A-20) into Equation(A-18) yields

$$\varepsilon_t = y \frac{\Delta_{NL}\pi^2}{2L_t^2} \cos\left(\frac{\pi(L_t - x)}{L_t}\right) + \frac{\Delta_{NL}^2\pi^2}{16L_t^2}. \quad (\text{A-22})$$

The strain energy density is given as

$$U_0 = \int_0^{\varepsilon_t} \sigma d\varepsilon = \frac{1}{2} E \varepsilon_t^2 = \frac{1}{2} E \left[y \frac{\Delta_{NL}\pi^2}{2L_t^2} \cos\left(\frac{\pi(L_t - x)}{L_t}\right) + \frac{\Delta_{NL}^2\pi^2}{16L_t^2} \right]^2 \quad (\text{A-23})$$

The strain energy is then obtained

$$U = \int U_0 dV = \frac{ET_t}{2} \int_0^{W_t} \int_0^{2L_t} \varepsilon_t^2 dx dy. \quad (\text{A-24})$$

The total strain energy is obtained by integrating Equation (A-24) to yield

$$U = ET_t \left(\frac{\Delta_{NL}^2\pi^4 W_t^3}{96L_t^3} + \frac{\Delta_{NL}^4\pi^4 W_t}{256L_t^3} \right). \quad (\text{A-25})$$

Based on the principle of virtual work, the total potential energy W is equal to the stored strain energy minus the work done by the external force K ,

$$W = U - K, \quad (\text{A-26})$$

where K is given by

$$K = P\delta + Q \int_0^{2L_t} \frac{\Delta_{NL}}{2} \left[1 + \cos\left(\frac{\pi(L_t - x)}{L_t}\right) \right] dx = \Delta_{NL} (P + QL_t). \quad (\text{A-27})$$

The equilibrium configuration is that in which the potential energy is minimized. The minimum is obtained when

$$\frac{dW}{d\delta} = ET_t \left(\frac{\Delta_{NL} \pi^4 W_t^3}{48L_t^3} + \frac{\Delta_{NL}^3 \pi^4 W_t}{64L_t^3} \right) - \frac{1}{2} \tau_w W_e L_e - \tau_w W_t L_t = 0. \quad (\text{A-28})$$

Rearranging Equation (A-28) yields

$$\Delta_{NL} \left(\frac{\pi^4}{96} + \frac{\pi^4}{128} \left(\frac{\Delta_{NL}}{W_t} \right)^2 \right) = \frac{\tau_w W_e L_e}{4ET_t} \left(1 + \frac{2W_t L_t}{W_e L_e} \right) \left(\frac{L_t}{W_t} \right)^3. \quad (\text{A-29})$$

Simplifying the above equation, $\frac{\pi^4}{96} \approx 1$ and $\frac{\pi^4}{128} \approx \frac{3}{4}$, yields an approximate large deflection solution,

$$\Delta_{NL} \left(1 + \frac{3}{4} \left(\frac{\Delta_{NL}}{W_t} \right)^2 \right) = \frac{\tau_w W_e L_e}{4ET_t} \left(1 + \frac{2W_t L_t}{W_e L_e} \right) \left(\frac{L_t}{W_t} \right)^3. \quad (\text{A-30})$$

Large Deflection-Analytical Method

For large deflection, axial force in the beam is not zero as in the small deflection model, and serves as a constitutive equation in the modeling analysis. Since the beam is symmetric, only half of the beam is analyzed, as shown in Figure A-3. For large deflections, taking axial force F_a into account, the differential equation governing the beam deflection caused by bending is given as

$$EI \frac{d^2 w(x)}{dx^2} = M(x), \quad (\text{A-31})$$

where the slope of beam caused by large deflection is assumed $dw/dx \ll 1$, and therefore $(dw/dx)^2$ is negligible. The moment $M(x)$ is given by

$$M(x) = \frac{1}{2}Qx^2 + \frac{P}{2}x - M_0 - F_a(w(0) - w(x)), \quad (\text{A-32})$$

where $w(0)$ is an unknown constant. Substituting Equation (A-32) into Equation (A-31) yields

$$EI \frac{d^2w(x)}{dx^2} - F_a w(x) = \frac{1}{2}Qx^2 + \frac{P}{2}x - M_0 - F_a w(0). \quad (\text{A-33})$$

The above equation can be solved as a superposition of one general solution w_n and a particular solution w_s ,

$$w(x) = w_n(x) + w_s(x), \quad (\text{A-34})$$

where $w_n(x) = C_1 \sinh(\lambda x) + C_2 \cosh(\lambda x)$ and $w_s(x) = ax^2 + bx + c$, assuming $\lambda = \sqrt{F_a/EI}$.

Substituting w_s into Equation (A-33), a, b, and c are obtained as

$$a = -\frac{Q}{2F_a}, \quad b = -\frac{P}{2F_a}, \quad \text{and} \quad c = w(0) + \frac{M_0}{F_a} - \frac{Q}{F_a \lambda^2}.$$

Equation (A-34) can be rewritten as

$$w(x) = C_1 \sinh(\lambda x) + C_2 \cosh(\lambda x) - \frac{Q}{2F_a}x^2 - \frac{P}{2F_a}x + w(0) + \frac{M_0}{F_a} - \frac{Q}{F_a \lambda^2}, \quad (\text{A-35})$$

for which the boundary conditions are:

$$\frac{dw(0)}{dx} = 0, \quad (\text{A-36})$$

$$\frac{dw(L_t)}{dx} = 0, \quad (\text{A-37})$$

and

$$w(L_t) = 0. \quad (\text{A-38})$$

For large deflection, the axial strain at $y = W_t/2$ is nonlinear and is given as

$$\varepsilon_x = \frac{du_0}{dx} + \frac{1}{2} \left(\frac{dw}{dx} \right)^2 = \frac{\sigma_x}{E} = \frac{F_a}{EA}, \quad (\text{A-39})$$

where $A = T_i W_i$. Integrating the above equation yields

$$F_a = \frac{EA}{L_i} \int_0^{L_i} \left(\frac{du_0}{dx} + \frac{1}{2} \left(\frac{dw}{dx} \right)^2 \right) dx. \quad (\text{A-40})$$

The first term in the integration is zero due to the doubly clamped boundary condition. Axial force F_a in the neutral axis $y = W_i/2$ is then obtained as

$$F_a = \frac{EA}{2L_i} \int_0^{L_i} \left(\frac{dw}{dx} \right)^2 dx. \quad (\text{A-41})$$

There are five unknown variables: C_1, C_2, F_a, M_0 , and $w(0)$, thus five boundary conditions are needed to solve for these unknown variables. However, only three boundary conditions (A-36)-(A-38) and one constitutive equation (A-41) are available. Another condition is $w(0) = w(0)$.

The problem is indeterminate and an iterative technique must be used to find the final result.

First, we applied boundary conditions (A-36)-(A-38) and the constitutive equation (A-41) into Equation (A-35) and solve it to get the maximum deflection as a function of the axial force in the neutral axis, F_a . The detailed procedure for solving this problem is given in the following.

Substituting (A-35) into boundary conditions (A-36) and (A-37) yields

$$C_1 = \frac{P}{2\lambda F_a} \quad \text{and} \quad C_2 = \frac{1}{F_a \lambda \sinh(\lambda L_i)} \left(Q L_i + \frac{P}{2} - \frac{P}{2} \cosh(\lambda L_i) \right). \quad (\text{A-42})$$

Substituting C_1 and C_2 into (A-35) and setting $x=0$ yields

$$M_0 = \frac{Q}{\lambda^2} - \frac{1}{\lambda \sinh(\lambda L_i)} \left(Q L_i + \frac{P}{2} - \frac{P}{2} \cosh(\lambda L_i) \right). \quad (\text{A-43})$$

Substituting M_0 from (A-43) and C_1 and C_2 from (A-42) into (A-35) yields

$$w(x) = \frac{P}{2\lambda F_a} \sinh(\lambda x) + \frac{\cosh(\lambda x) - 1}{F_a \lambda \sinh(\lambda L_i)} \left(Q L_i + \frac{P}{2} - \frac{P}{2} \cosh(\lambda L_i) \right) - \frac{Q}{2F_a} x^2 - \frac{P}{2F_a} x + w(0). \quad (\text{A-44})$$

Substituting (A-38) into (A-44) yields deflection at the center,

$$w(0) = -\frac{P}{2\lambda F_a} \sinh(\lambda L_t) - \frac{\cosh(\lambda L_t) - 1}{F_a \lambda \sinh(\lambda L_t)} \left(QL_t + \frac{P}{2} - \frac{P}{2} \cosh(\lambda L_t) \right) + \frac{QL_t^2}{2F_a} + \frac{PL_t}{2F_a}. \quad (\text{A-45})$$

Derivative Equation (A-44) to obtain

$$\frac{dw(x)}{dx} = \frac{1}{F_a} \left[\frac{P}{2} \cosh(\lambda x) + \frac{\sinh(\lambda x)}{\sinh(\lambda L_t)} \left(QL_t + \frac{P}{2} - \frac{P}{2} \cosh(\lambda L_t) \right) - Qx - \frac{P}{2} \right]. \quad (\text{A-46})$$

Secondly, we solve the maximum deflection equation (A-45) by iterating F_a . An initial value $F_a = 10^{-4}$ Pa is selected randomly and the following steps are performed to obtain the maximum deflection, $w(0)$.

- 1) Substitute F_a into (A-46) to get $\frac{dw}{dx}$, where $\lambda = \sqrt{\frac{Fa}{EI}}$.
- 2) Substitute $\frac{dw}{dx}$ into (A-41) to obtain new F_a .
- 3) Repeat 1), 2) until the relative error $|Fa^{n+1} - Fa^n| / Fa^{n+1} \leq 1e-6$.
- 4) Substitute F_a into (A-45) to find the maximum deflection $w(0)$.

Stress Analysis

The bending stress along a beam (shown in (A-3)) is given as [82]

$$\sigma_x = \frac{F}{A} + \frac{M_z y}{I_z}, \quad (\text{A-47})$$

where I_z is the moments of inertia for the z axis, and $I_z = TW_t^3/12$. In small deflection, the axial force $F_a = 0$. A free body diagram of the clamped beam is shown based on the discussion

in the small deflections section, where R_A and M_A are obtained from Equation (A-1) and (A-11), respectively. The moment for a certain length from the edge of the beam is obtained as,

$$M_z = -\frac{1}{4}PL_t - \frac{1}{3}QL_t^2 + \left(\frac{1}{2}P + QL_t\right)x - \frac{1}{2}Qx^2. \quad (\text{A-48})$$

Substituting Equation (A-48) into (A-47) and simplifying the equation to obtain the bending stress along the beam ($0 \leq x \leq L_t$) at $y = 0$,

$$\sigma_x = \frac{\tau_w W_e L_e L_t}{W_t^2 T_t} \left[\left(\frac{3}{4} + \frac{2W_t L_t}{W_e L_e} \right) - \left(\frac{3}{2} + \frac{6W_t L_t}{W_e L_e} \right) \left(\frac{x}{L_t} \right) + \frac{3W_t L_t}{W_e L_e} \left(\frac{x}{L_t} \right)^2 \right]. \quad (\text{A-49})$$

Effective Mechanical Mass and Compliance

In this section, the mechanical lumped parameters for a clamped-clamped beam are found. These parameters include lumped compliance obtained via the storage of potential energy and lumped mass obtained via the storage of kinetic energy. These results are used in Chapter 3 to develop the lumped element model of a laterally diffused piezoresistive shear stress sensor.

Recall that the lateral displacement and maximum displacement of the clamped-clamped beam in small deflection given in Chapter 2,

$$w(x) = \frac{\tau_w}{4EW_t^3 T_t} \left[(3W_e L_e L_t + 8W_t L_t^2)x^2 - (2W_e L_e + 8W_t L_t)x^3 + 2W_t x^4 \right] \quad (0 \leq x \leq L_t) \quad (\text{A-50})$$

and

$$w(L_t) = \frac{\tau_w W_e L_e}{4ET_t} \left[\frac{L_t}{W_t} \right]^3 \left[1 + 2 \frac{W_t L_t}{W_e L_e} \right]. \quad (\text{A-51})$$

The kinetic co-energy W_{KE} of a rectilinear system with a total effective mass m moving with velocity u is given as,

$$W_{KE}^* = \frac{1}{2}mu^2. \quad (\text{A-52})$$

For a simple harmonic motion, the velocity and displacement of the beam are related by

$$u(x) = j\omega w(x), \quad (\text{A-53})$$

where ω is the frequency and $u(L_t) = j\omega w(L_t)$. $u(x)$ is then expressed as

$$u(x) = \frac{w(x)}{w(L_t)} u(L_t) \quad (\text{A-54})$$

For an infinitesimal element on the beam with a mass of $\rho_{si} W_t T_t dx$, the kinetic co-energy

dW_{KE}^* is calculated using Equations (A-52) and (A-54) to be

$$dW_{KE}^* = \frac{1}{2} \rho_{si} W_t T_t u^2(x) = \frac{\rho_{si} W_t T_t u^2(L_t)}{2w^2(L_t)} w^2(x) dx \quad (\text{A-55})$$

where ρ_{si} is the density of silicon. Integrating Equation (A-55) over the beam gives the total kinetic co-energy of the system,

$$W_{KE}^* = 2 \int_0^{L_t} dW_{KE}^* = \frac{\rho_{si} W_t T_t u(L_t)^2}{w^2(L_t)} \int_0^{L_t} w^2(x) dx. \quad (\text{A-56})$$

The reference point is $x = L_t$, which corresponds to the maximum deflection of the beam $w(L_t)$.

The distributed deflection of the beam can be lumped into a rectilinear piston by equating the kinetic energy obtained in Equation (A-56) to the kinetic energy of the rectilinear piston of mass M_{me} ,

$$W_{KE} = \frac{M_{me} u(L_t)^2}{2}. \quad (\text{A-57})$$

Equating Equation (A-57) and (A-56) yields effective mechanical mass as

$$M_{me} = 2 \frac{\rho_{si} W_t T_t}{w^2(L_t)} \int_0^{L_t} w^2(x) dx. \quad (\text{A-58})$$

Since the velocity of the plate is $u = j\omega w(L_t)$, the effective mechanical mass of the device is the sum of the mass of the plate and the effective mechanical mass of the beam,

$$M_{me} = M_p + M_{me} = \rho_{si} L_e W_e T_t + M_{me} . \quad (\text{A-59})$$

The strain energy stored in the beam due to its deflection can be expressed as

$$W_{SE} = EI \int_0^{L_t} \left(\frac{d^2 w(x)}{dx^2} \right)^2 dx . \quad (\text{A-60})$$

The strain energy of an equivalent spring is given by

$$W_{SE} = \frac{1}{2} \frac{1}{C_{me}} w(L_t)^2 , \quad (\text{A-61})$$

where C_{me} is the mechanical compliance of the beam. Equating Equation (A-61) and (A-60)

yields

$$C_{me} \frac{w(L_t)^2}{2EI \int_0^{L_t} \left(\frac{d^2 w(x)}{dx^2} \right)^2 dx} . \quad (\text{A-62})$$

Substituting $w(x)$ and $w(L_t)$ in Equation (A-50) and (A-51) into (A-59) and (A-62) yields

$$M_{me} = \rho_{si} W_e L_e T_t \frac{1 + \frac{1494}{315} \frac{W_t L_t}{W_e L_e} + \frac{2238}{315} \left(\frac{W_t L_t}{W_e L_e} \right)^2 + \frac{1024}{315} \left(\frac{W_t L_t}{W_e L_e} \right)^3}{\left(1 + 2 \frac{W_t L_t}{W_e L_e} \right)^2} , \quad (\text{A-63})$$

and

$$C_{me} = \frac{1}{2ET_t} \left(\frac{L_t}{W_t} \right)^3 \frac{\left(1 + 2 \frac{W_t L_t}{W_e L_e} \right)^2}{1 + 4 \frac{W_t L_t}{W_e L_e} + \frac{64}{15} \left(\frac{W_t L_t}{W_e L_e} \right)^2} . \quad (\text{A-64})$$

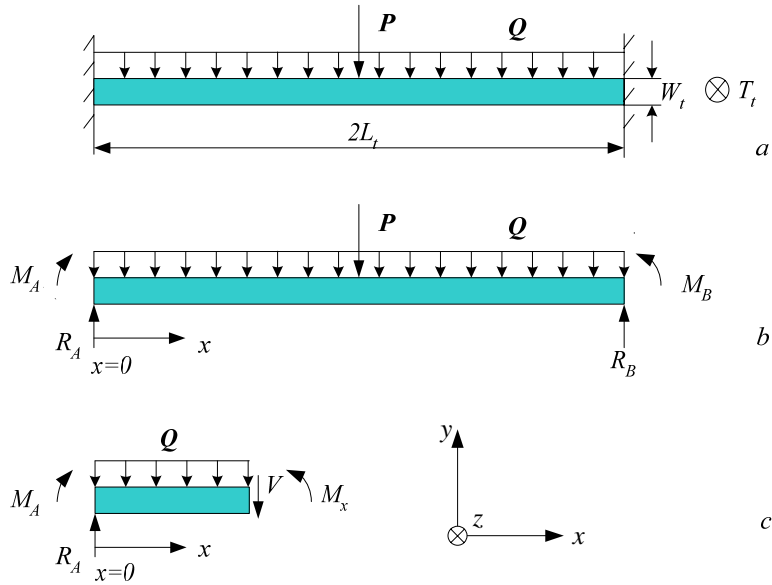


Figure A-1. The clamped beam and free body diagram. a) Clamped-clamped beam. b) Free body diagram of the beam. c) Free body diagram of part of the beam.

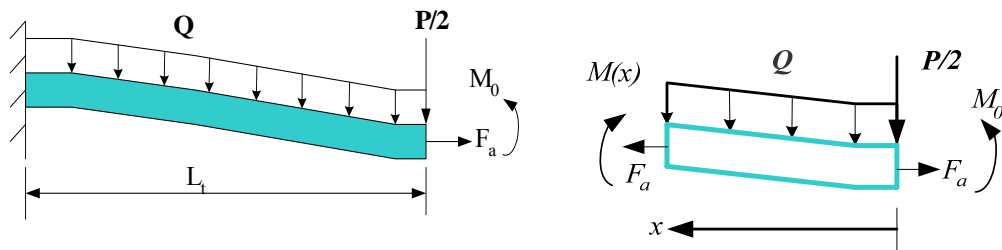


Figure A-2. Clamped-clamped beam in large deflection.

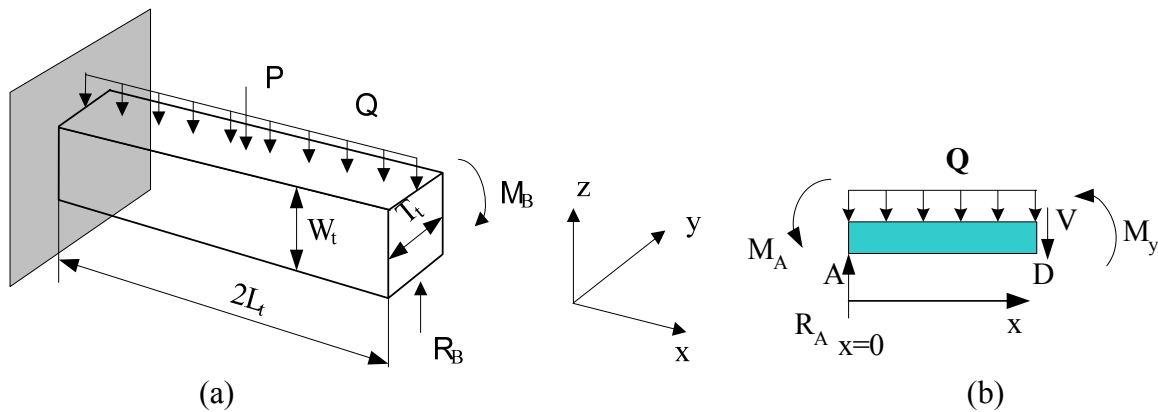


Figure A-3. Clamped-clamped beam in small deflection (a) and free body diagram of the clamped beam (b).

APPENDIX B
NOISE FLOOR OF THE WHEATSTONE BRIDGE

For a Wheatstone bridge shown in Figure B-1, assuming $R_1 = R_2 = R_3 = R_4 = R$, we get

$V_1 = V_B/2$, therefore the voltage across each resistor is

$$V_R = V_B - V_B/2 = V_B/2. \quad (\text{B-1})$$

The current through the resistor is

$$I_R = \frac{V_B}{2R}. \quad (\text{B-2})$$

Assuming the noise sources are uncorrelated, the mean square noise can be solved as a superposition of the mean square thermal noise, the $1/f$ noise, and the amplifier noise. For thermal noise, the equivalent noise model is given in Figure B-2. The rms thermal voltage is given as

$$V_{n,thermal} = \sqrt{E_1^2 + E_2^2} = \sqrt{4k_B T (R_1 \parallel R_2) \Delta f + 4k_B T (R_3 \parallel R_4) \Delta f} = \sqrt{4k_B T R \Delta f}. \quad (\text{B-3})$$

For $1/f$ noise, the equivalent noise model is given in Figure B-3. The mean square current noise is

$$I_1^2 = \frac{\alpha_H I_R^2}{N_{c1}} \ln \left(\frac{f_2}{f_1} \right). \quad (\text{B-4})$$

The mean square voltage noise E_1^2 is obtained as

$$E_1^2 = (I_1^2 + I_2^2) (R_1 \parallel R_2)^2. \quad (\text{B-5})$$

Substituting Equation (B-4) and (B-2) into (B-5) to obtain

$$\begin{aligned} E_1^2 &= \left(\frac{\alpha_H I_R^2}{N_{c1}} \ln \left(\frac{f_2}{f_1} \right) + \frac{\alpha_H I_R^2}{N_{c2}} \ln \left(\frac{f_2}{f_1} \right) \right) (R_1 \parallel R_2)^2 \\ &= \left(\frac{\alpha_H V_B^2}{N_c 4R^2} \ln \left(\frac{f_2}{f_1} \right) + \frac{\alpha_H V_B^2}{N_c 4R^2} \ln \left(\frac{f_2}{f_1} \right) \right) (R_1 \parallel R_2)^2. \end{aligned} \quad (\text{B-6})$$

Rearrange the above equation to get

$$E_1^2 = \frac{\alpha_H V_B^2}{8N_c} \ln\left(\frac{f_2}{f_1}\right). \quad (\text{B-7})$$

The rms $1/f$ voltage is obtained as

$$V_{n,1/f} = \sqrt{E_1^2 + E_2^2} = \sqrt{2\left(\frac{\alpha_H V_B^2}{8N_c} \ln\left(\frac{f_2}{f_1}\right)\right)} = \sqrt{\frac{\alpha_H V_B^2}{4N_c} \ln\left(\frac{f_2}{f_1}\right)}. \quad (\text{B-8})$$

The total noise floor is obtained via the superposition of the mean square noises

$$V_n = \sqrt{\frac{\alpha_H V_B^2}{4N_c} \ln\left(\frac{f_2}{f_1}\right) + 4k_B TR\Delta f + (4e-9)^2}, \quad (\text{B-9})$$

where the last term in the above equation is the low amplifier noise.

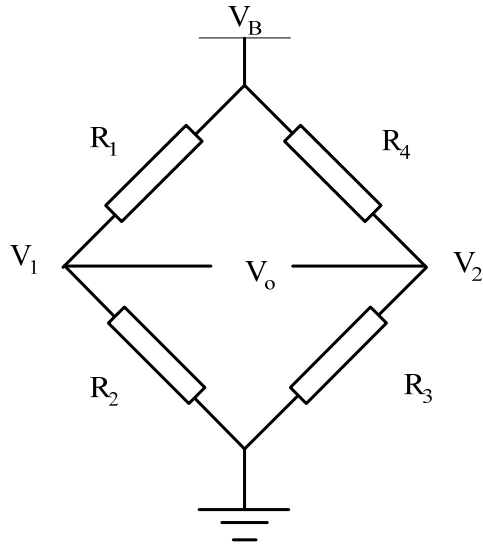


Figure B-1. The Wheatstone bridge.

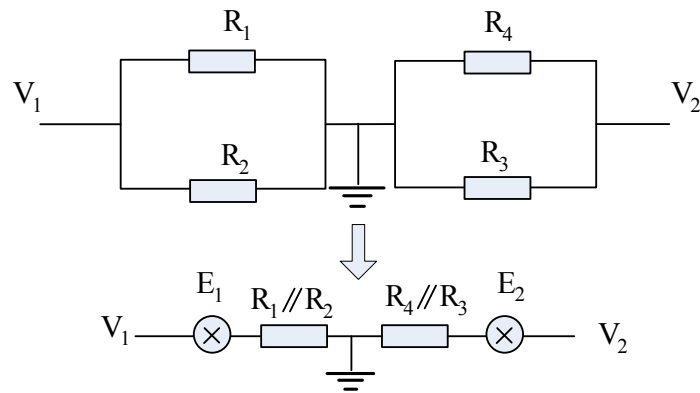


Figure B-2. The thermal noise model of the Wheatstone bridge.

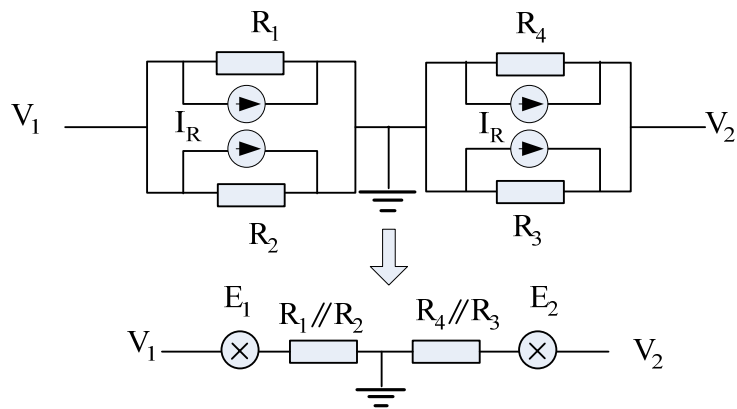


Figure B-3. The $1/f$ noise model of the Wheatstone bridge.

APPENDIX C PROCESS TRAVELER

Wafer: n-type <100> 1-5 ohm-cm, SOI wafer

Start with SOI wafer (n-Si (100) 1-5 Ω -cm) with 50 μ m silicon on 1.5 μ m buried oxide (BOX).

DI rinse

Masks

Reversed biased mask-----RBM

Piezo contact mask-----PCM

Nested mask-----NM

Side implant mask-----SIM

Bond pad cuts mask-----BPCM

Metal mask-----MM

Bond pad mask-----BPM

Process Steps

1. n-well Implant

- Ion implant- dopant = phosphorus, energy = 150 keV, dose = 4×10^{12} cm⁻². 7 degree tilt, blanket implantation. This forms the n-well. This needs to be simulated first.
- Piranha clean

2. PECVD oxide: deposit oxide 0.1 μ m via PECVD

3. Reverse Bias Contact

- Coat and pattern photoresist/oxide on front side
 - HMDS evaporation for 5min
 - Spin AZ1529 at 4000rpm for 50sec & softbake at 90° C oven for 30min
 - Pattern by mask RBM
 - Exposure 60sec at 8.8mJ/cm²
 - Develop at AZ300MIF for 50sec
 - Hard bake at 90° C oven for 60min

- BOE(7:1) : ~80sec to etch 0.1 μ m oxide. This step puts alignment marks on the wafer
- Ion implant- dopant =phosphorus, energy = 80 keV, dose = 9×10^{13} cm⁻². 7 degree tilt
- Ash strip photoresist
- RCA clean
- Thermal annealing at $T = 1000^\circ$ C , time=420sec in nitrogen

4. Inplant Interconnection Contact

- Coat and pattern photoresist/oxide on front side
 - HMDS evaporation for 5min
 - Spin AZ1529 at 4000rpm for 50sec & softbake at 90° C oven for 30min
 - Pattern by mask PCM, align to the alignment marks created via RBM
Exposure 60sec at 8.8mJ/cm²
Develop at AZ300MIF for 50sec
Hard bake at 90° C oven for 60min
- BOE(7:1) : 90sec to etch 0.1 μ m oxide. This step puts alignment marks on the wafer
- Preamorphization Implant
 - Ion implant- dopant = Ge, energy = 160 keV, dose = 1×10^{15} cm⁻². 7 degree tilt
 - Ion implant- dopant = Ge, energy = 50 keV, dose = 1×10^{15} cm⁻². 7 degree tilt
- Ion implant- dopant = boron, energy = 50 keV, dose = 1.2×10^{16} cm⁻². 7 degree tilt
- Ash strip photoresist
- Piranha clean

5. Nested Mask Release

- Deposit PECVD oxide 1 μ m
- Coat and pattern photoresist on front side
 - HMDS evaporation for 5min
 - Spin AZ1529 at 2000rpm for 50sec & softbake at 95° C convection oven for 25min
 - Pattern by mask NM, align to the alignment marks created via PCM
Exposure 85sec at 7.9 mJ/cm²
Develop at AZ300MIF for 60sec
Hard bake at 90° C oven for 60min
- Plasma dry oxide etch. This step puts new alignment marks on the wafer

- BOE(6:1) oxide etch to remove the oxide residues

6. Etch Sidewalls

- Coat and pattern photoresist on front side
 - HMDS evaporation for 5min
 - Spin AZ1512 at 2000rpm for 40sec & softbake at 95° C hotplate for 50sec
 - Pattern by side implantation mask(SIM), align to the alignment marks created via NM
 - Exposure 19sec at 4.5mJ/cm²
 - Develop at AZ300MIF for 70sec
 - Hard bake at 90° C oven for 60min
- BOE(6:1) oxide for 2min
- DRIE silicon to ~8µm deep
- BOE(6:1) oxide for 60sec to avoid Piezoresistor and Piezo contact disconnection due to DRIE undercut
- Ash strip photoresist
- Piranha clean

7. Hydrogen Annealing

- $T = 1000^{\circ}\text{C}$, $P=5\text{mTorr}$ for 5min in pure hydrogen for surface roughness reduction

8. Oxidation: thermal grown wet oxide 1000A at T=1000°C

9. Side Wall Implantation

- Preamorphization implant
 - Ion implant- dopant = Ge, energy = 160 keV, dose = $1\text{e}15 \text{ cm}^{-2}$. 54 degree tilt
 - Ion implant- dopant = Ge, energy = 50 keV, dose = $1\text{e}15 \text{ cm}^{-2}$. 54 degree tilt
- Ion implant- dopant = boron, energy = 50 keV, dose = $1\text{e}16 \text{ cm}^{-2}$. 54 degree tilt
- Piranha clean

10. Beam Definition

- Etch oxide by reactive ion etch via dielectric setting in STS
- DRIE silicon to BOX
- BOE(6:1) 2min to remove oxide (ensure to remove 0.1µm oxide on sidewall)

11. Oxidation

- Piranha clean
- Annealing at $T=1000^{\circ}\text{C}$ for 60min in nitrogen
- Thermal dry oxide grown at $T=975^{\circ}\text{C}$ for 235min ($0.1\mu\text{m}$)

12. Bond Pad Cuts

- Trench filling
 - Spin AZ1512 at 800rpm for 40sec & softbake at 95°C hotplate for 50sec
 - Spin AZ9260 at 800rpm for 50sec & softbake at 90°C oven for 30min
 - Flood exposure
Exposure 300sec at $7.9\text{mJ}/\text{cm}^2$
Develop at AZ400MIF till clear
- Coat and pattern photoresist on front side
 - HMDS evaporation for 5min
 - Spin AZ1512 at 0.5k/2k for 5/40sec & softbake at 95°C hotplate for 50sec
 - Pattern by bond pad cuts mask(BPCM), align to the alignment marks created via PCM
Exposure 45sec at $4.5\text{mJ}/\text{cm}^2$
Develop at AZ300MIF for 60sec
Hard bake at 90°C oven for 60min
- BOE(6:1) oxide for 15min
- Remove photoresist

13. Metalization

- Trench filling
- Descum in oxygen plasma
- Deposit $1\mu\text{m}$ Al-Si(1%) to avoid spiking via sputtering
- Coat and pattern photoresist on front side
 - HMDS evaporation for 5min
 - Spin AZ1529 at 0.2k rpm and stay for 2min. Then spin at 0.2k/2k rpm for 10/50sec with ramp rate of 100/500 rmp/s
 - Softbake at 90°C oven for 30min
 - Pattern by metal mask (MM), align to the alignment marks created via BPCM
Exposure 100sec at $7.9\text{mJ}/\text{cm}^2$
Develop at AZ300MIF for 1min 30sec

Hard bake at 90° C oven for 60min

- Etch Al by RIE
- Remove photoresist

14. Nitride Passivation

- Deposit 2000A PECVD silicon nitride
- Trench filling
- Coat and pattern photoresist on front side
 - HMDS evaporation for 5min
 - Spin AZ1512 at 4000rpm for 40sec & softbake at 95° C hotplate for 50sec
 - Pattern by bond pad mask(BPM), align to the alignment marks created via MM
Exposure 18sec at 4.5mJ/cm²
Develop at AZ300MIF for 60sec
Hard bake at 90° C oven for 60min
- Etch nitride by RIE
- Remove photoresist

15. Final Release

(a) Device wafer

- Spin AZ9260 on front side of the device wafer
 - Spin speed 200rpm, ramp rate 100rpm/s for 10s, wait for 1min. Run this recipe twice
 - Spin speed 4000rpm, ramp rate 1000rpm/s for 50s
 - Soft bake at 90° C oven for 30min
- HMDS on the backside
- Spin AZ9260 on backside of the device wafer
 - Spin speed 2000rpm, ramp rate 1000rpm/s for 50s
 - Soft bake in 90° C oven for 30min
- Pattern by back release mask(BRM), align to the alignment marks created via NM
 - Exposure 25sec in EVG520 mask aligner
 - Develop at AZ300MIF for 3min 40sec

- Hard bake at 90° C oven for 60min
- (b) Carrier wafer
 - Spin PR AZ9260 on a carrier wafer
 - Spin speed 2000rpm, ramp rate 1000rpm/s for 50s
 - Soft bake at 90° C oven for 20-30min
 - Put some cool grease on the edge of the carrier wafer
 - Bake on hotplate, 60° C for 5min
 - Put the device wafer face down on the carrier wafer.
 - Put on the hotplate, apply pressure using swab
- (c) DRIE
 - Run DRIE, stopped until 50um silicon left
 - Put the wafer on the hotplate 60° C for 5min, separate from the carrier wafer
 - Separate the wafer into individual dies
- (d) Process on individual dies
 - Spin AZ9260 on a carrier wafer
 - Spin speed 2000rpm, ramp rate 1000rpm/s for 50s
 - Put the device die on the top of the carrier wafer, apply pressure using swab
 - Soft bake in 90° C oven for 30min
 - DRIE to BOX layer
 - RIE BOX layer for 15min, run BOE 5-10min to remove the residues
 - RIE nitride for 6min
 - Remove the device die using tweezers
 - Put the device die in AZ400 PR stripper
 - Plasma clean in Asher for 10min

APPENDIX D PROCESS SIMULATION

This chapter includes the FLOOPS process simulation of the piezoresistor, p++ interconnects and n-well, as well as the reverser bias connections.

(a). Piezoresistor

This program simulates the doping profile of piezoresistor in the silicon layer after ion implantation, anneal and thermal oxidation. The boron is implanted into preamorphization Si layer with oxide as a screen layer. Its initial doping profile is simulated by SRIM, and then imported to FLOOPS file for subsequent process simulation.

```
line x loc=-0.1 spa=0.005 tag=SiO2top
line x loc=0 spa=0.005 tag=top
line x loc=1.5 spa=0.01 tag=bot
region oxide xlo=SiO2top xhi=top
region silicon xlo=top xhi=bot
init
#profile name=B_SRIM
inf=/home/yawei/Floops_new/SRIM_B_50keV_0.1umSiO2_Si_only.txt
sel z=B_SRIM*5 name=Boron
sel z=log(Boron)
layer
etch oxide time=1 rate=0.1 iso
diffuse temp=1000 time=60
diffuse temp=975 dry time=235
puts "### Oxide thickness after thermal oxide is [expr [interface oxide /silicon] - [interface gas /oxide]] um."
sel z=log10(Boron)
plot.1d bound !cle label=PZR
set cout [open /home/yawei/Floops_new/pzrdata w] puts $cout [print.1d] close $cout
sel z=log10(5.0e14)
plot.1d !cle label=background
sel z = Boron-5e14
puts "The Junction Depth is [interpolate silicon z=0.0]"
set z=Boron
layer
```

(b). P++ interconnection and n-well

```
#p++ surface concentration is ~1e+21 and n-well Ns~1e+16
# generate grid
```

```

line x loc=0   spa=0.001 tag=top
line x loc=1.0   spa=0.01
line x loc=2.5   spa=0.01 tag=bot
region silicon xlo=top xhi=bot
init
sel z=5e14 name=Phosphorus
implant phosph dose=4.0e12 energy=150 tilt=7
#deposit 0.1um PECVD oxide
deposit time=4 rate =0.030 oxide grid=10 puts "Oxide thickness after PECVD oxide is [expr
[interface oxide /silicon] - [interface gas /oxide]] um."
diffuse temp=1000 time=450
strip oxide
implant boron dose=1.2e16 energy=50 tilt=7
#strip oxide
#deposit 1um PECVD oxide
deposit time=41.9 rate =0.0239 oxide grid=10 puts "### Oxide thickness after 2nd PECVD
oxide is [expr [interface oxide /silicon] - [interface gas /oxide]] um."
diffuse temp=1000 wet time=9.2 # oxide thickness is 1000A
etch oxide time=1 rate=0.1 iso
diffuse temp=1000 time=60
diffuse temp=975 dry time=235
sel z=log10(Phosphorus+1)
plot.1d bound !cle color=blue label=nwell
set cout [open /home/yawei/Floops_new/nwelldata w] puts $cout [print.1d] close $cout
sel z=log10(5e14)
plot.1d !cle color=pink label=background
sel z=log10(Boron+1)
plot.1d bound !cle color=red label=p++
set cout [open /home/yawei/Floops_new/ohmicdata w] puts $cout [print.1d] close $cout
sel z = Boron- Phosphorus
layer
puts "The Junction Depth is [interpolate silicon z=0.0]"

```

(c). Reverse biased contact

```

line x loc=0   spa=0.005 tag=top
line x loc=2.5   spa=0.01 tag=bot
region silicon xlo=top xhi=bot
init
sel z=5.0e14 name=Phosphorus
implant phosph dose=4.0e12 energy=150
#deposit 0.1um PECVD oxide
deposit time=4.19 rate =0.0239 oxide grid=10 puts "Oxide thickness after PECVD oxide is [expr
[interface oxide /silicon] - [interface gas /oxide]] um."
strip oxide smooth
set t [open temp.P w+]

```

```

sel z=Phosphorus
puts $t [print.1d]
close $t
# start with a new grid ... since strip oxide removes the nodes near the surface where the new
phosphorus profile is about to go set former_interface [interface gas /silicon]
line x loc=$former_interface spa=0.0001 tag=top
line x loc=0.1 spa=0.001
line x loc=1.0 spa=0.01
line x loc=2.5 spa=0.01 tag=bot
region silicon xlo=top xhi=bot
init
profile name=Phosphorus inf=temp.P
# inplant phosphorus for reverse bias contact
implant phosph dose=9.0e13 energy=80 tilt=7
sel z=log10(Phosphorus)
plot.1d bound !cle color=red label=Profile_ini
#Thermal Annealing 450min at T=1000 deg
diffuse temp=1000 time=450
#deposit 1um PECVD oxide
deposit time=41.9 rate =0.0239 oxide grid=10 puts "#### Oxide thickness after 2nd PECVD
oxide is [expr [interface oxide /silicon] - [interface gas /oxide]] um."
# thermal grown oxide 1000A at T=975 deg
diffuse temp=1000 dry time=9.2
etch oxide time=1 rate=0.1 iso
diffuse temp=1000 time=60
diffuse temp=975 dry time=235
puts "#### Oxide thickness after thermal oxide is [expr [interface oxide /silicon] - [interface gas
/oxide]] um."
sel z=log10(5.0e+14)
plot.1d bound !cle color=black label=background
sel z=log10(Phosphorus+1)
plot.1d bound !cle color=blue label=reverse_bias
set cout [open /home/yawei/Floops_new/reversedata w]
puts $cout [print.1d]
close $cout
layers

```

APPENDIX E
MICROFABRICATION RECIPE FOR RIE AND DRIE PROCESS

Table E-1. Input parameters in the ASE on STS DRIE systems.

Parameters	50 μm Si etch	8 μm Si etch	SiO ₂ etch
Coil power	600 W	600 W	800 W
Platen power	12 W	12 W	130
APC (mTorr)	28 (fixed)	28 (fixed)	50 (auto)
Etching process	11	6	
Passivation process	6.5	4	
SF ₆ flow (sccm)	130	130	
O ₂ flow (sccm)	13	13	
C ₄ F ₈ flow (sccm)	85	85	
Etching cycle	Varies	Varies	Varies
Passivation cycle	Varies	Varies	Varies

Table E-2. Anisotropic oxide/nitride etch recipe on the Unaxis ICP Etcher system.

Parameters	Oxide	Nitride
CHF ₃ flow (sccm)	45	--
SF ₆ flow (sccm)	--	15
O ₂ flow (sccm)	3	5
RF2 power (W)	600	300
RF1 power (W)	100	100
Chamber pressure (mTorr)	15	20
Helium flow (sccm)	20	10

Table E-3. Anisotropic aluminum etch recipe on the Unaxis ICP Etcher system.

Parameters	Settings
Ar flow (sccm)	5
Cl ₂ flow (sccm)	30
BCl ₃ flow (sccm)	15
RF2 power (W)	500
RF1 power (W)	100
Chamber pressure (mTorr)	5
Helium flow (sccm)	20

APPENDIX F
PACKAGING DRAWINGS

Measurements Units: mm

Material: Lucite

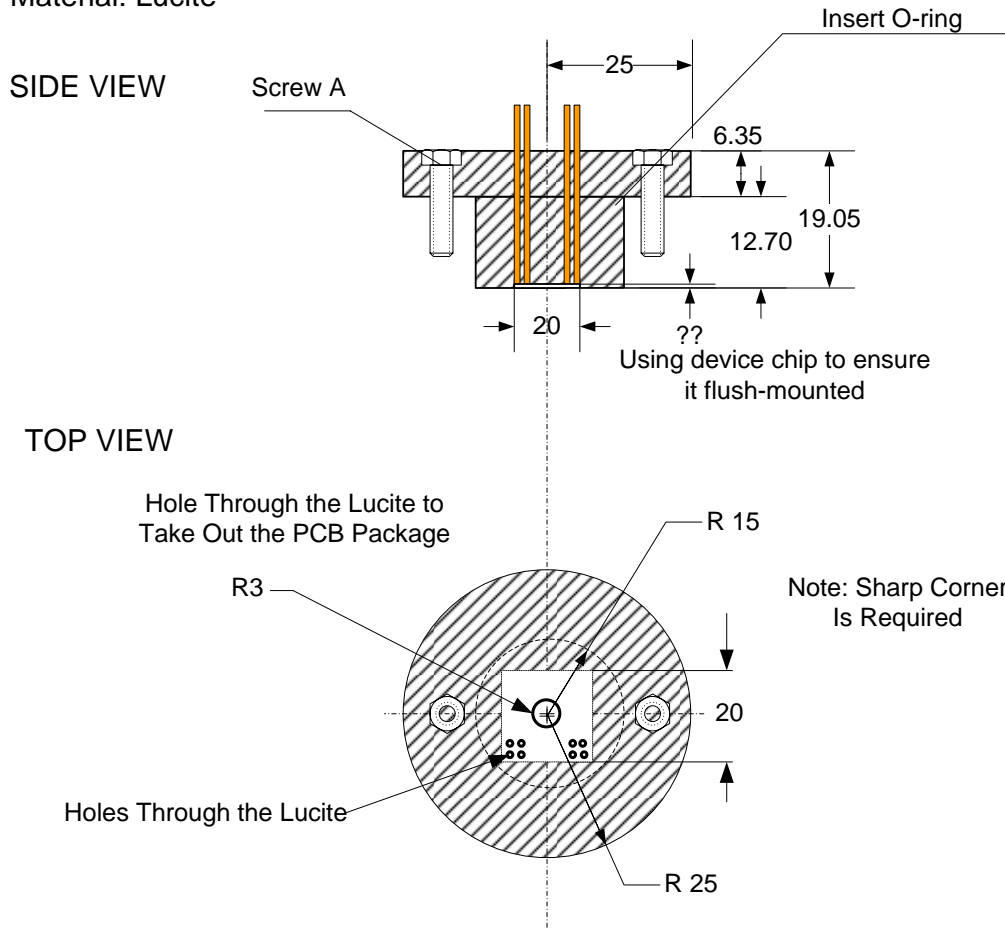
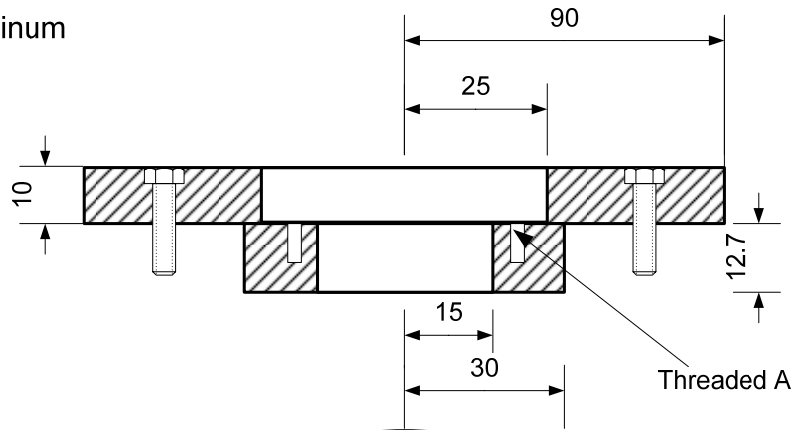


Figure E-1. The drawing illustrating the Lucite packaging.

Measurements Units: mm

Material: Aluminum

SIDE VIEW



TOP VIEW

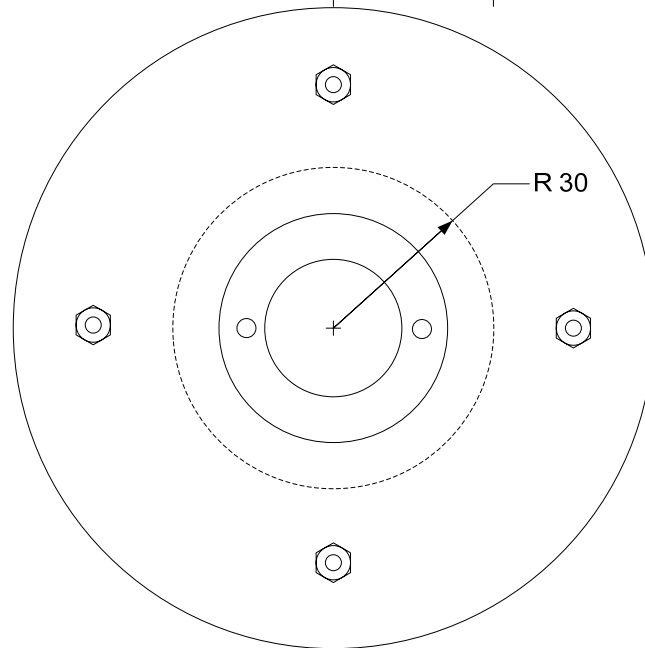


Figure E-2. The aluminum plate for the plane wave tube interface connection.

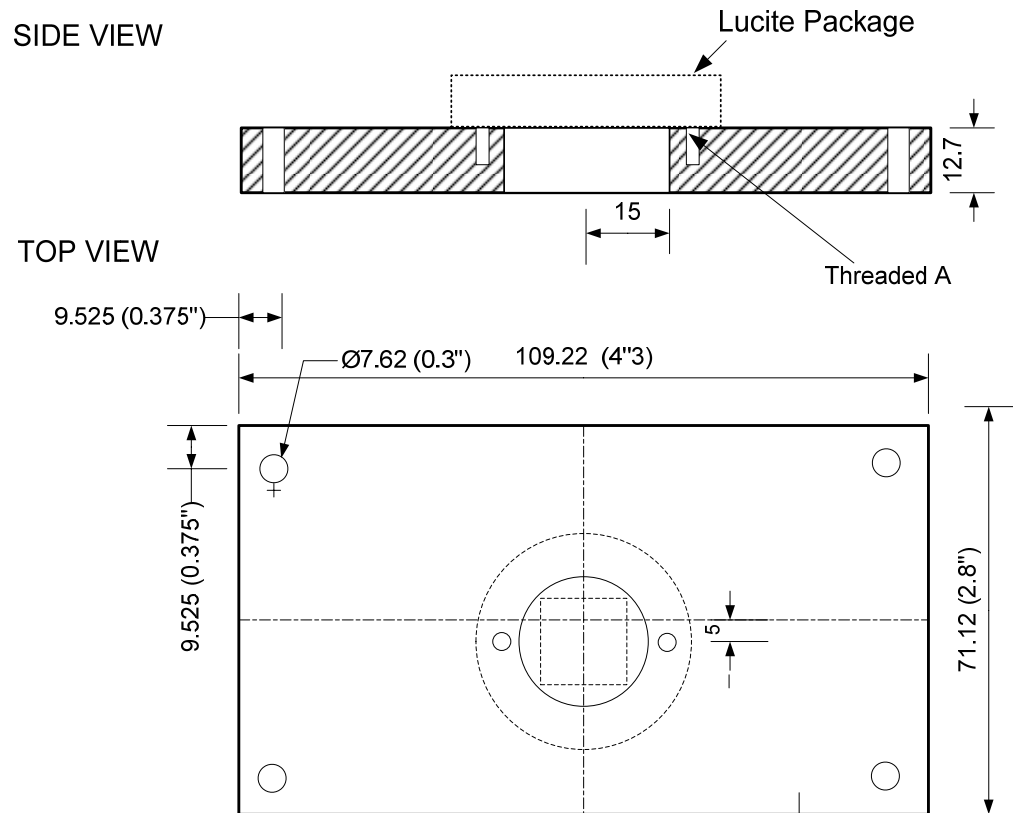


Figure E-3. Aluminum packaging for pressure sensitivity testing.

LIST OF REFERENCES

- [1] P. J. Johnston, J. Allen H. Whitehead, and G. T. Chapman, "Fitting Aerodynamics and Propulsion into the Puzzle," *Aerospace America*, pp. 32-42, 1987.
- [2] W. Shyy, M. Berg, and D. Ljungqvist, "Flapping and Flexible Wings for Biological and Micro Air Vehicles," *Prog. Aerosp. Sci.*, vol. 35, pp. 455-505, 1999.
- [3] M. Sheplak, L. Cattafesta, and Y. Tian, "Micromachined Shear Stress Sensors for Flow Control Applications," *IUTAM Symposium on Flow Control and MEMS*, London, England 2007, pp. 67-73.
- [4] J. W. Naughton and M. Sheplak, "Modern Development in Shear Stress Measurement," *Prog. Aerosp. Sci.*, vol. 38, pp. 515-570, 2002.
- [5] M. Gad-el-Hak, *Flow Control*: Cambridge University Press, 2000, pp. 209-210.
- [6] R. Rathnasingham and K. S. Breuer, "Active Control of Turbulent Boundary Layers," *J. Fluid Mech.*, vol. 495, pp. 209-233, 2003.
- [7] F. M. White, *Viscous Fluid Flow*, 2nd ed.: McGraw Hill, 1991, Ch.1, 4, 5, 6.
- [8] H. Tennekes and J. L. Lumley., *A First Course in Turbulence*: The MIT Press, 1972, Ch.1, 5.
- [9] Y. A. Cengel and J. M. Cimbala, *Fluid Mechanics: Fundamentals and Applications*: McGraw-Hill 2006.
- [10] L. Lofdahl and M. Gad-el-Hak, "MEMS-Based Pressure and Shear Stress Sensors for Turbulent Measurement," *Meas. Sci. Tech.*, vol. 10, pp. 665-686, 1999.
- [11] A. Padmanabhan, "Silicon Micromachined Sensors and Sensor Arrays for Shear-Stress Measurements in Aerodynamic Flows," Ph.D Dissertation in Department of Mechanical Engineering, Massachusetts Institute of Technology, 1997.
- [12] H. Alfredsson, A. V. Johansson, J. H. Haritonidis, and H. Eckelman, "The Fluctuating Wall-Shear Stress and the Velocity Field in the Viscous Sublayer," *Phys. Fluids*, vol. 31, pp. 1026-1033, 1988.
- [13] M. Gad-el-Hak and P. R. Bandyopadhyay, "Reynolds Number Effects in Wall-Bounded Flows," *Appl. Mech. Rev.*, vol. 47, pp. 307-365, 1994.
- [14] J. M. Corcos, "Resolution of Pressure in Turbulence," *J. Acoust. Soc. Am.*, vol. 35 (2), pp. 192-200, 1963.
- [15] T. A. Brungart, G. C. Lauchle, S. Deutsch, and E. T. Riggs, "Outer-Flow Effects on Turbulent Boundary Layer Wall Pressure Fluctuations," *J. Acoust. Soc. Am.*, vol. 105, pp. 2097-2106, 1999.

- [16] R. F. Blackwelder and J. H. Haritonidis, "Scaling of the Bursting Frequency in Turbulent Boundary Layer," *J. Fluid Mech.*, vol. 132, pp. 87-103, July 1983.
- [17] W. W. Willmarth and L. K. Sharma, "Study of Turbulent Structure with Hot Wires Smaller than the Viscous Length," *J. Fluid Mech.*, vol. 142, pp. 121-149, May 1984.
- [18] M. A. Schmidt, R. T. Howe, S. D. Senturia, and J. H. Haritonidis, "Design and Calibration of a Micromachined Floating-Element Shear-Stress Sensor," *IEEE Trans. Electron Devices*, vol. 35, pp. 750-757, 1988.
- [19] J. Shajji, K.-Y. Ng, and M. A. Schmidt, "A Microfabricated Floating Element Shear Stress Sensor Using Wafer-bonding Technology," *J. Microelectromech. Syst.*, vol. 1 (2), pp. 89-94, June 1992.
- [20] A. Padmanabhan, H. Goldberg, K. D. Breuer, and M. A. Schmidt, "A Wafer-Bonded Floating-Element Shear Stress Microsensor with Optical Position Sensing by Photodiodes," *J. Microelectromech. Syst.*, vol. 5 (4), pp. 307-315, 1996.
- [21] T. Pan, D. Hyman, and M. Mehregany, "Microfabricated Shear Stress Sensors, Part 1: Design and Fabrication," *AIAA J.*, vol. 37, pp. 66-72, 1999.
- [22] F.-G. Tseng and C.-J. Lin, "Polymer MEMS-Based Fabry-Perot Shear Stress Sensor," *IEEE Sensors J.*, vol. 3, pp. 812-817, Dec. 2003.
- [23] S. Horowitz, T.-A. Chen, V. Chandrasekaran, K. Tedjojuwono, L. Cattafesta, T. Nishida, and M. Sheplak, "A Micromachined Geometric Moiré Interferometry Floating-Element Shear Stress Sensor," *IEEE Solid-State Sensor and Actuator Workshop*, 2004, pp. 13-18.
- [24] J. Zhe, V. Modi, and J. Kenneth. R. Farmer, "A Microfabricated Wall Shear-Stress Sensor with Capacitative Sensing," *J. Microelectromech. Syst.*, vol. 14 (1), pp. 167-175, Feb. 2005.
- [25] A. A. Barlian, S.-J. Park, V. Mukundan, and B. L. Pruitt, "Design and Characterization of Microfabricated Piezoresistive Floating Element-Based Shear Stress Sensors," *Sensors and Actuators A*, vol. 134 (1), pp. 77-87 2007.
- [26] M. E. Law and S. Cea, "Continuum Based Modeling of Silicon Integrated Circuit Processing: An Object Oriented Approach," *Computational Materials Science*, vol. 12, pp. 289-308, August 1998.
- [27] J. I. Haritonidis, "The Measurement of Wall Shear Stress," *Advances in Fluid Mechanics Measurements*, Springer-Verlag, pp. 229-261, 1989.
- [28] K. G. Winter, "An Outline of the Techniques Available for The Measurements of Skin Friction in Turbulent Boundary Layers," *Prog. Aerosp. Sci.*, vol. 18, pp. 1-57, 1977.
- [29] T. J. Hanratty and J. A. Campbell, "Measurements of Wall Shear Stress," *Fluid Mech. Measurements*, 1983, pp. 559-615.

- [30] T. K. Hsiai, S. K. Cho, P. K. Wong, M. Ing, A. Salazar, A. Sevanian, M. Navab, L. L. Demer, and C.-M. Ho, "Monocyte Recruitment to Endothelial Cells in Response to Oscillatory Shear Stress," *FASEB J.*, vol. 17(12), pp. 1648-1657, September, 2003.
- [31] B. Oudheusden and J. Huijsing, "Integrated Flow Friction Sensor," *Sensors and Actuators A*, vol. 15, pp. 135-144, 1988.
- [32] E. Kalvesten, G. Stemme, C. Vieider, and L. Lofdahl, "An Integrated Pressure-Flow Sensor for Correlation Measurement in Turbulent Gas Flow," *Sensors and Actuators A*, vol. 52, pp. 51-58, 1996.
- [33] C. Liu, J.-B. Huang, A. Z. Z, F. Jiang, S. Tung, Y.-C. Tai, and C.-M. Ho, "A Micromachined Flow Shear-Stress Sensor Based on Thermal Transfer Principles," *J. Microelectromech. Syst.*, vol. 8 (1), pp. 90 - 99, March 1999.
- [34] M. Sheplak, V. Chandrasekaran, A. Cain, T. Nishida, and L. N. C. III, "Characterization of a Micromachined Thermal Shear Stress Sensor," *AIAA J.*, vol. 40, pp. 1099-1104, 2002.
- [35] D. Fourquette, D. Modarress, F. Taugwalder, D. Wilson, M. Koochesfahani, and M. Gharib, "Miniature and MOEMS Flow Sensor," *AIAA paper 2001-2982*, 2001.
- [36] C. Brücker, D. Bauer, and H. Chaves, "Dynamic Response of Micro-Pillar Sensors Measuring Fluctuating Wall-Shear-Stress," *Exp. in Fluids*, vol. 42 (5), 2007
- [37] C. Brücker, J. Spatz, and W. Schröder, "Feasibility Study of Wall Shear Stress Imaging Using Microstructured Surfaces with Flexible Micropillars," *Exp. in Fluids*, vol. 39 (2), pp. 464-474, Aug. 2005.
- [38] T. V. Papen, H. Steffes, H. D. Ngo, and E. Obermeier, "A Micro Surface Fence Probe for the Application in Flow Reverse Area," *Sensors and Actuators A*, vol. 97-98, pp. 264-270, 2002.
- [39] M. A. Schmidt, "Microsensors for the Measurement of Shear Forces in Turbulent Boundary Layers," Ph.D Dissertation in Mechanical Engineering, Massachusetts Institute of Technology, 1988.
- [40] B. Carroll, E. Boulos, M. Sytsma, L. Cattafesta, J. P. Hubner, and M. Sheplak, "Aero-Optic Measurement Facility Characterization," in *42nd Aerospace Sciences Meeting and Exhibit, AIAA Paper 2004-0936*, Reno, NV, 2004.
- [41] Z. W. Hu, C. L. Morfey, and N. D. Sandham, "Wall Pressure and Shear Stress Spectra from Direct Simulations of Channel Flow," *AIAA J.*, vol. 44 (7), July 2006 2006.
- [42] T. Pan, D. Hyman, and M. Mehregany, "Microfabricated Shear Stress Sensors, Part 2: Testing and Calibration," *AIAA J.*, vol. 37, pp. 73-78, 1999.

- [43] M. Sheplak, A. Padmanabhan, M. A. Schmidt, and K. S. Breuer, "Dynamic Calibration of a Shear-Stress Sensor Using Stokes-Layer Excitation," *AIAA J.*, vol. 39 (5), pp. 819-823, May 2001.
- [44] H. D. Goldberg, K. S. Breuer, and M. A. Schmidt, "A Silicon Wafer-Bonding Technology for Microfabricated Shear-Stress Sensors with Backside Contacts," *IEEE Solid-State Sensor and Actuator Workshop*, Hilton Head, SC, 1994, pp. 111-115.
- [45] N. Maluf, *An Introduction to Microelectromechanical Systems Engineering*. Norwood, MA: Artech House, 2000.
- [46] S. D. Senturia, *Microsystem Design*: Kluwer Academic Publishers, 2001, Ch. 10, 17, 18, 19.
- [47] J. A. Harley and T. W. Kenny, "1/f Noise Considerations for the Design and Process Optimization of Piezoresistive Cantilevers," *J. Microelectromech. Syst.*, vol. 9 (9), June 2000.
- [48] M. Sheplak, L. Cattafesta, and T. Nishida, "Microelectromechanical Floating Element Flow Sensor," U.S Patent Number: 6966231, Issued on November 22, 2005.
- [49] A. A. Barlian, R. Narain, J. T. Li, C. E. Quance, A. C. Ho, V. Mukundan, and B. L. Pruitt, "Piezoresistive MEMS Underwater Shear Stress Sensors," *MEMS' 06*, Istanbul, Turkey, 2006, p. 626.
- [50] B. W. Chui, T. W. Kenny, H. J. Mamin, B. D. Terris, and D. Rugar, "Independent Detection of Vertical and Lateral Forces with a Sidewall-Implanted Dual-Axis Piezoresistive Cantilever," *Appl. Phys. Lett.*, vol. 72 (11), pp. 1388-1394, 1998.
- [51] A. Partridge, J. K. Reynolds, B. W. Chui, E. M. Chow, A. M. Fitzgerald, L. Zhang, N. I. Maluf, and T. W. Kenny, "A High-Performance Planar Piezoresistive Accelerometer," *J. Microelectromech. Syst.*, vol. 9 (1), March 2000.
- [52] C. S. Smith, "Piezoresistance Effects in Germanium and Silicon," *Physical Review*, vol. 94, 1954.
- [53] M. Madou, *Fundamentals of Microfabrication*: CRC Press, 1997, Ch. 4.
- [54] A. H. Nayfeh and P. F. Pai, *Linear and Nonlinear Structural Mechanics*: John Wiley & Sons, Inc, 2004, pp. 183.
- [55] M. Rossi, *Acoustics and Electroacoustic.*: Artech House, 1988, pp. 245.
- [56] J. Merhaut, *Theory of Electroacoustics*: McGraw-Hill Inc., 1981, Ch. 1.
- [57] S. M. Sze, *Semiconductor Sensors*: Wiley-Interscience, 1994, pp. 160.

- [58] O. N. Tufte and D. Long, "Recent Development in Semiconductor Piezoresistive Devices," *Solid State Electronics*, vol. 6, pp. 323-338, 1963.
- [59] Y. Kanda, "A Graphical Representation of the Piezoresistive Coefficients in Silicon," *IEEE Trans. Electron Devices*, vol. 29 (64), pp. 64-70, 1982.
- [60] J. Brysek, K. Petersen, J. Joseph R. Mallon, L. Christel, and F. Pourahmadi, *Silicon Sensors and Microstructures*: Lucas NovaSensor, 1991, Ch. 4.
- [61] O. N. Tufte and E. L. Stelzer, "Piezoresistive Properties of Silicon Diffused Layers," *J. Appl. Phys.*, vol. 34 (2), pp. 313-318, 1963.
- [62] W. P. Mason, J. J. Forst, and L. M. Tornillo, *Recent Developments in Semiconductor Strain Transducers*: New York, 1962.
- [63] D. R. Kerr and A. G. Milelnes, "Piezoresistance of Diffused Layers in Cubic Semiconductors," *J. Appl. Phys.*, vol. 34 (4), pp. 727-731, 1963.
- [64] M. Tortonese, "Force Sensors for Scanning Probe Microscopy," Ph.D Dissertation in Department of Mechanical Engineering: Stanford University, 1993.
- [65] J. A. Harley, "Advances in Piezoresistive Probes for Atomic Force Microscopy," Ph.D Dissertation in Department of Mechanical Engineering: Stanford University, 2000.
- [66] J. D. Plummer, M. D. Deal, and P. B. Griffin, *Silicon VLSI Technology*: Prentice Hall, 2000, Ch. 7, 8.
- [67] T. Nishida and C.-T. Sah, "A Physical Based Mobility Model for MOSFET Numerical Simulation," *IEEE Trans. Electron Devices*, vol. 34 (2), pp. 310-320, 1987.
- [68] H. Nyquist, "Thermal Agitation of Electric Charge in Conductors," *Phys. Rev.*, vol. 32, pp. 110-113, 1928.
- [69] J. B. Johnson, "Thermal Agitation of Electricity in Conductors," *Phys. Rev.*, vol. 32, pp. 97-109, 1928.
- [70] F. N. Hooge, "1/f Noise is No Surface Effect," *Phys. Lett. A*, vol. 29, pp. 139-140, 1969.
- [71] E. Simoen and C. Claeys, "On the Flicker Noise in Sub Micron Silicon MOSFETs," *Solid State Electronics*, vol. 43, pp. 865-882, 1999.
- [72] A. McWhorter, "1/f noise and Germanium Surface Properties," in *Semiconductor Surface Physics*: University of Pennsylvania, Philadelphia, 1957, pp. 207-228.
- [73] Analog Devices Inc, www.analog.com.
- [74] M. Akbar and M. A. Shanblatt, "Temperature Compensation of Piezoresistive Pressure Sensors," *Sensors and Actuators A*, vol. 33, pp. 155-162, 1992.

- [75] K. Suzuki, T. Ishihara, M. Hirata, and H. Tanigawa, "Nonlinear Analysis of a CMOS Integrated Silicon Pressure Sensor," *IEEE Trans. Electron Devices*, vol. 34, pp. 1360-1367, 1987.
- [76] R. F. Pierret, *Semiconductor Device Fundamentals*: Addison-Wesley, 1996, Ch.5, 6.
- [77] R. C. Jaeger, *Introduction to Microelectronic Fabrication*, 1993, pp. 57.
- [78] M. E. Law and S. M. Cea, "Continuum Based Modeling of Silicon Integrated Circuit Processing: An Object Oriented Approach," *Computational Materials Science*, vol. 12, pp. 289-308, Nov 1998.
- [79] SRIM, www.srim.org.
- [80] S. M. Sze and G. Gibbons, "Avalanche Breakdown Voltage of Abrupt and Linearly Graded p-n junctions in Ge, Si, GaAs, and GaP," *Appl. Phys. Lett.*, vol. 8, pp. 111, 1966.
- [81] S. M. Sze, *Physics of Semiconductor Devices*, 2nd ed.: John Wiley & Sons, Inc, 1981, pp. 193.
- [82] R. C. Hibbeler, *Mechanics of Materials*, Third ed.: Prentice Hall, 1997, pp. 160
- [83] J. D. Plummer, M. D. Deal, and P. B. Griffin, *Silicon VLSI Technology: Fundamentals, Practice, and Modeling*, Prentice Hall, 2000.
- [84] M. Papila, R. T. Haftka, T. Nishida, and M. Sheplak, "Piezoresistive Microphone Design Pareto Optimization: Tradeoff Between Sensitivity and Noise Floor," *J. Microelectromech. Syst.*, vol. 15 (6), pp. 1632-1643, December 2006.
- [85] A. Partridge, "Lateral Piezoresistive Accelerometer with Epipoly Encapsulation," Ph.D Dissertation in Department of Electrical Engineering, Stanford University, 2003.
- [86] Mathworks Inc, MATLAB R2006b ed, 2006.
- [87] J. F. Schutte and A. A. Groenwold, "A Study of Global Optimization Using Particle Swarms," *J. Global Opt.*, vol. 31 (1), pp. 93-108, 2005.
- [88] R. T. Haftka and Z. Gurdal, *Elements of Structural Optimization*: Kluwer Academic Publishers, 1992.
- [89] B. El-Kareh, *Fundamentals of Semiconductor Processing Technologies*, 3rd ed.: Kluwer Academic Publisher, 1998.
- [90] Unaxis, www.unaxis.com.
- [91] STS, www.stsystems.com.
- [92] M.-C. M. Lee, J. Yao, and M. C. Wu, "Silicon Profile Transformation and Sidewall Roughness Reduction Using Hydrogen Annealing," *MEMS '05*, Miami, FL, USA, 2005.

- [93] R. Legtenberg, H. Jansen, M. d. Boer, and M. Elwenspoek, "Anisotropic Reactive Ion Etching of Silicon Using SF₆/O₂/CHF₃ Gas Mixtures," *J. Electrochem. Soc.*, vol. 142, pp. 2020-2028, 1995.
- [94] M. Ohring, *The Materials Science of Thin Films*: Academic Press, 1992.
- [95] C.-T. Sah, *Fundamentals of Solid-State Electronics*: World Scientific, 1993.
- [96] Stanford Research Systems, <http://www.thinksrs.com/products/SIM928.htm>.
- [97] V. Chandrasekaran, A. Cain, T. Nishida, L. N. Cattafesta, and M. Sheplak, "Dynamic Calibration for Thermal Shear-Stress Sensors with Mean Flow," *Exp. in Fluids*, vol. 39, pp. 56-65, 2005.
- [98] R. Dieme, G. Bosman, M. Sheplak, and T. Nishida, "Source of Excess Noise in Silicon Piezoresistive Microphones," *J. Acoust. Soc. Am.*, vol. 119, pp. 2710-2720, May 2006.
- [99] M. G. Jones and P. E. Stiede, "Comparison of Methods for Determining Specific Acoustic Impedance," *J. Acoust. Soc. Am.*, vol. 101(5), pp. 2694-2704, 1997.
- [100] J. N. Reddy, *Theory and Analysis of Elastic Plates*: Taylor and Francis, 1999, pp. 25.

BIOGRAPHICAL SKETCH

Yawei Li received her BS and MS degree in Aerospace Engineering at Beijing University of Aeronautics and Astronautics, China. She worked with China Aerospace Corporation before she joined University of Florida. She also received MS (2003) in Aerospace Engineering and ME (2006) in Electrical Engineering from University of Florida, respectively.

She is currently a Ph.D student in the Department of Mechanical and Aerospace Engineering at the University of Florida. Her current research focuses on the sensor modeling, design optimization, fabrication, and characterization of MEMS-based piezoresistive sensors that enable the measurement and control of wall shear stress in turbulent flow.